HYDRODYNAMIC IMPACTS OF TIDAL LAGOONS IN THE UPPER BAY OF FUNDY

JULIEN COUSINEAU

Submitted under the supervision of
Dr. Ioan Nistor
Dr. Andrew Cornett

In partial fulfillment of the requirements
for the degree of
Master of Applied Science in Civil Engineering

Department of Civil Engineering
University of Ottawa
September, 2012

uOttawa

Acknowledgements

First, I would like to thank Professor Dr. Ioan Nistor (University of Ottawa) and Dr. Andrew Cornett (NRC - Canadian Hydraulic Centre), both supervisors of this thesis, for giving me the opportunity to work in an excellent research environment, for their support, and their feedback on my work, which improved its quality significantly. In addition, I would like to thank them again for taking the time to read though the thesis document and providing me with invaluable feedback that has significantly elevated the quality of the final document.

Over the course of the thesis, I have come into contact with a number of other experts, whose advice I have greatly appreciated. My very special thanks go to Thierry Faure and Martin Serrer (NRC - CHC) for generously sharing their knowledge and experience in numerical modeling. Thanks are furthermore due the thesis defence committee for the time and effort devoted to reading and evaluating this thesis.

I would like the express my deep gratitude to my family for their interest in my work and their support, which were inestimable value during my academic education.

Finally and most importantly, I am immensely grateful to my spouse, Mélanie, for her unconditional support and her encouragement, for her understanding and patience when I had to work evenings and week-ends.

Abstract

Among sources of renewable energy, development of tidal energy has traditionally been plagued by relatively high costs and limited availability of sites with sufficiently high tidal amplitudes or flow velocities. However, many recent technology developments and improvements, both in design (e.g. dynamic tidal power, tidal lagoons) and turbine technology (e.g. new axial turbines, crossflow turbines), showed that the economic and environmental costs may be brought down to competitive levels comparing to other conventional energy sources.

It has long been identified that the Bay of Fundy is one of the world's premier locations for the development of tidal power generating systems, since it has some of the world's largest tidal ranges. Consequently, several proposals have been made in the recent years to find economical ways to harness the power of tides. Presently, there is considerable interest in installing tidal lagoons in the Bay of Fundy. The lagoon concept involves temporarily storing seawater behind an impoundment dike and generating power by gradually releasing the impounded seawater through conventional low-head hydroelectric turbines. A tidal lagoon will inherently modify the tides and tidal currents regime in the vicinity of the lagoon, and possibly induce effects that may be felt throughout the entire Bay of Fundy. The nature of these hydrodynamic impacts will likely depend on the size of the tidal lagoon, its location, and its method of operation. Any changes in the tidal hydrodynamics caused by a tidal lagoon may also impact on the transport of sediments throughout the region and upset ecosystems that are well adapted to existing conditions. The scale and character of the potential hydrodynamic impacts due to tidal lagoons operating in the Bay of Fundy have not been previously investigated. The present study endeavours to investigate these potential impacts to help the development of sustainable, science-based policies for the management and development of clean energy for future generations.

After outlining fundamental aspects of tidal power projects taken in consideration in the Bay of Fundy, an analysis of present knowledge on tidal lagoons was conducted in order to provide a focus for subsequent investigations. Hydrodynamic modeling was used to quantify any of the potential hydrodynamic changes induced in the Bay of Fundy due to the presence of tidal la-

goons. In the last part of the thesis, new relationships were derived in order to describe the amount of energy removed from tidal lagoons associated with its hydrodynamic impacts.

Keywords: Bay of Fundy, Tidal renewable energy, Tidal power, Hydrodynamics, Numerical model, 2D hydrodynamic model

Table of Contents

List of Figures

List of Tables

List of Symbols

Latin symbols

a	Tidal constituents amplitude	[m]
a	Scale parameter	[-]
a_c	Coriolis acceleration	[m/s^2]
b	Scale parameter	[-]
d	Distance	[km]
e	Relative error	[-]
f	Coriolis parameter	[s^{-1}]
g	Gravitational acceleration	[m/s^2]
i	Step number in a simulation	[-]
j	Turbine number	[-]
k	Location parameter	[-]
m	Mass	[kg]
n_p	Manning's coefficient	[-]
n	Number of steps in a simulation	[-]
q	Discharge per unit width	[m^3/ms]
r	Radius	[m]
t	Time	[s]
t_{step}	Time step	[s]
u	Velocity in x-direction	[m/s]
v	Velocity in y-direction	[m/s]
v_e	Easting velocity	[m/s]
v_n	Northing velocity	[m/s]
x	Space coordinate in x-direction	[m]
y	Space coordinate in y-direction	[m]

A	Wet flow-through area	[m^2]
A_c	Critical area or flow area based on critical depth	[m^2]
C	Chézy coefficient	[-]
C_d	Discharge coefficient	[-]
C_1	Unsubmerged inlet constant	[-]
C_2	Unsubmerged inlet constant	[-]
C_3	Unsubmerged inlet constant	[-]
C_4	Submerged inlet constant	[-]
C_5	Submerged inlet constant	[-]
C_f	Friction coefficient	[-]

D	Diameter	[m]
E_d	Downstream water elevation	[m]
E_i	Elevation of culvert inlet invert relative to culvert outlet invert	[m]
E_{cycle}	Power generation for one spring-neap tidal cycle	[GWh]
E_u	Upstream water elevation	[m]
F	Bottom friction force	[N]
H	Head loss	[m]
H	Water head	[m]
H_{min}	Minimum operating head	[m]
H_{normal}	Normal operating head	[m]
K	Strickler's coefficient	[$m^{1/3}$/s]
K_e	Minor loss coefficient	[-]
L_p	Length of culvert	[m]
P	Wetted perimeter	[m]
P	Power	[MW]
P_{avg}	Averaged power output	[MW]
Q	Discharge	[m^3/s]
Q_p	Flow rate	[m^3/s]
S_h	Source term in total water depth-direction	[m/s^2]
S_p	Longitudinal slope	[m/m]
S_x	Source term in x-direction	[m/s^2]
S_y	Source term in y-direction	[m/s^2]
T_c	Top width of flow based on critical depth	[m]
V_C	Critical velocity or velocity based on critical depth	[m/s]
V_{max}	Maximum velocity	[m/s]
V_R	Residual velocity	[m/s]
V_{RMS}	Root mean square of velocity	[m/s]
$\bar{V}$	Depth-averaged velocity	[m/s]
Y_{avg}	Average water depth	[m]
Y_C	Critical water depth	[m]
Y_h	Headwater depth	[m]
Y_t	Tailwater depth	[m]
Z	Free surface water elevation	[m]

Greek symbols

α	Tidal constituents phase angle	[rad]
ΔH	Water head difference	[m]
$\Delta\psi$	Change in a hydrodynamic variable	[-]
$(\Delta\psi)_{\%}$	Percentage change in a hydrodynamic variable	[%]
η	Sea surface elevation or water level	[m]
η	Efficiency	[-]
η_m	Water level from modeled results	[m]
η_{max}	Maximum water level	[m]
η_{min}	Minimum water level	[m]

η_o	Water level from observed results	[m]
θ	Steepest slope on a given surface	[m/m]
θ	Scale parameter	[-]
θ	Partially full angle	[rad]
θ_c	Partially full angle based on critical depth	[rad]
μ	Viscosity	[kg/ms]
ρ	Density	[kg/m^3]
τ	Shear stress	[Pa]
τ_{max}	Maximum shear stress	[Pa]
τ_{RMS}	Root mean square of shear stress	[Pa]
φ	Latitude	[rad]
ω	Angular frequencies	[s^{-1}]
ω	Angular velocity of the earth	[7.27×10^{-5} rad/s]
Φ	Tidal range	[m]
Φ_{max}	Maximum tidal range	[m]
ψ	Hydrodynamic variable	[-]
ψ_e	Hydrodynamic variable from a model without tidal lagoons	[-]
ψ_p	Hydrodynamic variable from a model with tidal lagoons	[-]
Ω	Angular velocity vector	[rad/s]

Abbreviations

ADCP	Acoustic Doppler Current Profiler
BoF	Bay of Fundy
C1	Calibration time period #1
CB	Chignecto Bay
CHC	Canadian Hydraulic Center
DFO	Department of Fisheries and Oceans Canada
DMC	Delta Marine Consultants
GoM	Gulf of Maine
Hyd.	Hydrodynamic
MB	Minas Basin
NOAA	National Oceanic and Atmospheric Administration
NRC	National Research Council
RMS	Root mean square
S1-S19	Hypothetical simulation #1 to simulation #19
TEC	Tidal Electric Canada
V1,V2,V3	Validation time period #1, # 2 and #3

Chapter 1

Introduction

1.1 Background

Over a century, the world's energy usage has been dominated by the use of fossil fuels, a non-renewable energy known for producing tremendous amounts of greenhouse gases. These gases are often pointed to as being partly responsible for climate change. To alleviate the effects of climate change, there are increasing calls and search for alternative energy sources. Alternative energy sources are producing little to no greenhouse gas emissions while still contributing to the current and future energy needs of the world. Renewable energy has been the main focus in research and development during the past few decades. Some of these alternatives include solar energy, wind energy, hydroelectric energy, tidal energy, and geothermal energy. One type of this renewable energy, i.e. tidal energy, is not yet widely used but has the potential for future electricity generation.

It has long been identified that the Bay of Fundy (BoF), which is located on the north-eastern coast of North America, mainly between the Canadian provinces of New Brunswick and Nova Scotia, is one of the world's premier locations for the development of tidal power generating systems since it has some of the world's largest tidal ranges. The tidal range in the Minas Basin, located in the upper part of the Bay of Fundy, exceeds 16 m during spring tides.

Considerable research has been undertaken in recent years to find economical ways to harness tidal energy. In the early 1970s, a series of technical and economic assessments were performed to look into the feasibility and environmental impacts of a potential large-scale tidal barrage in the Bay of Fundy. From these studies, it was concluded that the development of a large-scale tidal barrage was considered potentially hazardous to the surrounding ecosystem and with inadequate funds to start the project, the project was never implemented. Although a large-scale tidal barrage has not been successful, a smaller-scale tidal barrage was completed at Annapolis Royal, Nova Scotia in 1984 instead. The tidal power station has the capacity to generate 20 MW of elec-

tricity and supplies 1.0% of the power demand of Nova Scotia. The Annapolis tidal barrage remains one of three tidal power plants operating worldwide.

Tidal energy has traditionally suffered from relatively costly and limited availability of sites with sufficiently high tidal ranges or tide-induced flow velocities. However, many recent technology developments and improvements, both in design (e.g. dynamic tidal power, tidal lagoons) and turbine technology (e.g., new axial turbines, crossflow turbines), indicate that economic and environmental costs may be brought down to competitive levels.

Presently, there is considerable interest in installing in-stream turbines to extract energy from the strong currents flowing through Minas Passage, in the Upper Bay of Fundy. These devices generate power from tidal currents, much as wind turbines generate power from air currents. The tidal lagoon is another option that is being presently considered. The lagoon concept involves temporarily storing seawater behind an impoundment dike and generating power by gradually releasing the impounded seawater through conventional low-head hydroelectric turbines. Tidal lagoons are intended to achieve high efficiency while diminishing some of the environmental problems associated with tidal barrages.

1.1 Significance and novelty of the study

Tidal lagoons are generally huge and challenging engineering projects, costing several billions of dollars and requiring substantial funds. Their development can be separated into five main task areas that required parallel consideration. These tasks, shown in Figure 1.1, are: (1) Feasibility and technical design, (2) hydrodynamic analysis, (3) market and systems analyses, (4) socioeconomic analysis, and (5) environmental analysis.

Commissioned by Tidal Electric Canada (TEC), Delta Marine Consultants (DMC) (2007) performed a feasibility study to construct a tidal lagoon in Minas Basin. Although they have studied the technical aspect of tidal lagoons, the potential hydrodynamic impacts due to this new technology have not been investigated. A tidal lagoon operating in Minas Basin or other regions in the Upper Bay of Fundy has the potential to modify the characteristics of the tides and tidal currents near the lagoon, and possibly create effects that are felt throughout the entire Bay of Fundy and even in the Gulf of Maine (GoM). The nature of these hydrodynamic impacts will likely depend on the size of the tidal lagoon as well as its location and method of operation. Any

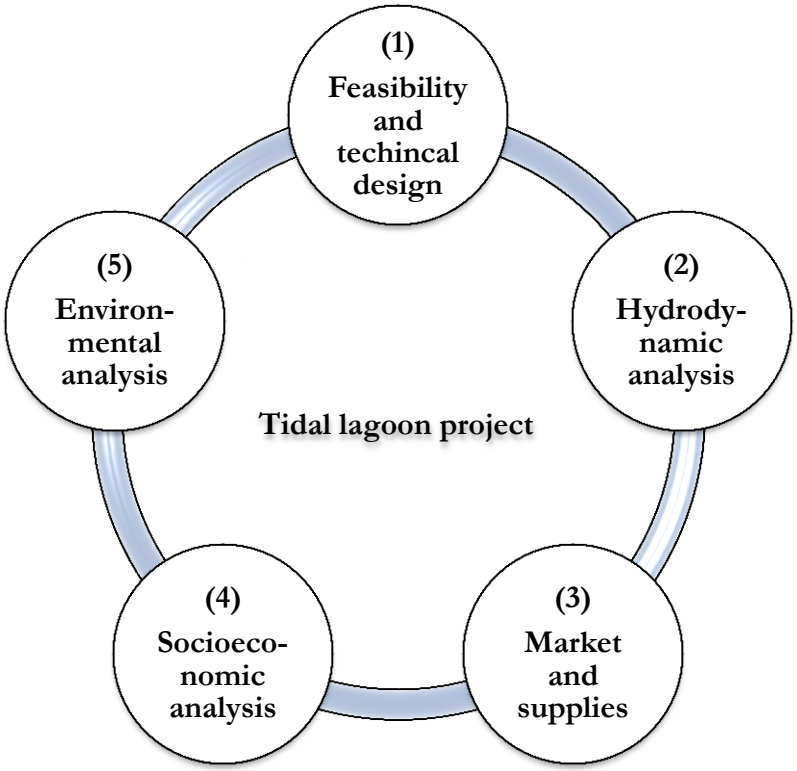

Figure 1.1: Organizational framework of tidal power project.

changes in the tidal hydrodynamics caused by a tidal lagoon could potentially impact on the transport of sediments throughout the region, and upset also the local ecosystems that are presently well adapted to existing conditions.

In this study, a numerical model was constructed and deployed to study the hydrodynamic effects of a single and/or multiple tidal lagoons operating in the Upper Bay of Fundy. The development on the technical design aspect was further assessed to develop these tidal lagoons. Relationships between extractable energy from tidal lagoons associated with their hydrodynamic impacts were studied. Such studies aim to help the development of sustainable, science-based policies for the management and development of Nova Scotia's tidal energy resource for future generations.

This study is the first study to employ a two-dimensional hydrodynamic numerical model to assess the change in hydrodynamics in the Bay of Fundy and Gulf of Maine due to the implementation of tidal lagoons.

1.2 Main objectives

The present study focuses on the technical design aspect and the hydrodynamic analysis of tidal lagoons in the Bay of Fundy. In summary, this thesis aims to answer the following question: 'How will tidal lagoons impact the hydrodynamic in the Bay of Fundy? More specifically, the objectives of the thesis are:

1. To assess the design and operation regime of tidal lagoons.
2. To develop hydrodynamic models with and without the presence of tidal lagoons.
3. To quantify hydrodynamic changes induced by the presence of tidal lagoons.
4. To describe relationships between extractable energy from tidal lagoons associated with their hydrodynamic impacts.

1.3 Thesis outline

This thesis is divided into seven chapters.

Chapter 1 describes the significance and novelty of the study, explains the main objectives, and describes the general framework of the thesis.

Chapter 2 starts with an overview of the hydrodynamic characteristics in the Bay of Fundy and previous studies on tidal power projects. This chapter concludes with an analysis of present knowledge on hydrodynamic modeling as well as of tidal lagoon design and modeling

Chapter 3 discusses the implementation of various tidal lagoon designs in the Upper Bay of Fundy in order to study their effects on the complex hydrodynamics of the Bay of Fundy and Gulf of Maine.

Chapter 4 describes the development of the hydrodynamic modeling and analysis. It consists of studying the hydrodynamics with and without tidal lagoons in the Bay of Fundy and determining the hydrodynamic impacts in the region of the Bay of Fundy and the Gulf of Maine. Finally, relationships were developed between different tidal lagoon characteristics and their hydrodynamic impact.

Chapter 5 discusses the developments and findings of all preceding chapters in order to provide a detailed understanding of the hydrodynamic impacts of tidal lagoons in the Bay of Fundy.

Chapter 6 summarizes the principal findings and provides the most significant conclusions derived from this work. Finally, recommendations for future work are also made.

Chapter 7 lists all references consulted during this study.

Chapter 2

Literature Review

2.1 Introduction

An overview of the hydrodynamic characteristics in the Bay of Fundy and previous studies on tidal power projects is provided herein. The main focus lies on finding and describing different techniques of harnessing the power of the tides, and determining their advantages and disadvantages. Finally, an analysis of present knowledge on design and modeling tidal lagoons following by hydrodynamic modeling is presented. This analysis serves to identify techniques of hydrodynamic modeling with tidal lagoons. Figure 2.1 shows a schematic layout of the content of Chapter 2.

For ensuing parts of the present chapter, basic knowledge on the aspects of tide is very useful. Readers who are not familiar with this topic are directed to read Appendix A.

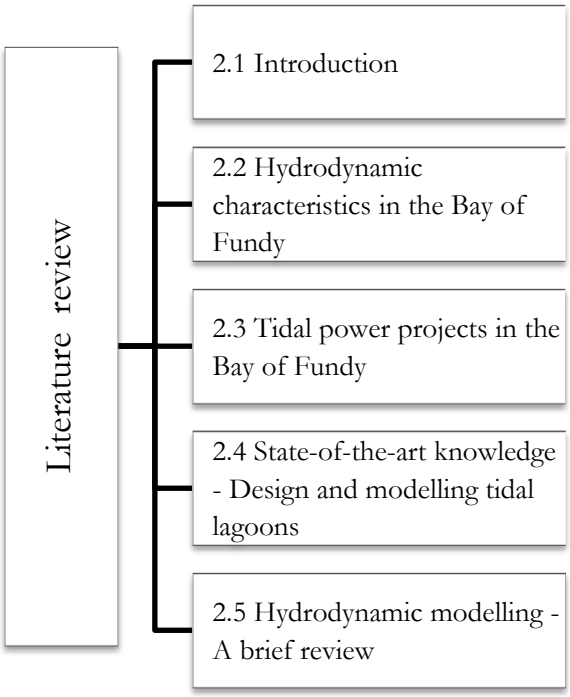

Figure 2.1: Layout of Chapter 2.

2.2 Hydrodynamic Characteristics in the Bay of Fundy

2.2.1 Introduction

The Gulf of Maine (GoM) is a large, semi-enclosed body of seawater located on the north-eastern coast of North America (Figure 2.2). The GoM has an area of around 200,000 km^2 and interconnects with the Atlantic Ocean through a series of shoals, banks and channels. The Bay of Fundy covers around 20,000 km^2 and is located northeast of the state of Maine, between New Brunswick and Nova Scotia, Canada. Bay of Fundy can be divided up of two sections in its upper zone: Chignecto Bay and Minas Basin (Figure 2.3).

2.2.2 Tidal water levels

Bay of Fundy is well-known for having the highest tidal range in the world: tides rise and fall over 12-16 meters, twice daily. Wolfville, located on the southern shore of Minas Basin, offers the most dramatic views of the tidal rise and fall, including vast areas of the sea bottom uncovered by the falling tide. The primary cause of the very large tidal range at the Bay of Fundy is a resonance of the Bay of Fundy-Gulf of Maine system at the tidal period. The area is bounded to the south by the edge of the continental shelf and gradually increases in depth towards the ocean. The bay's shape and bottom topography also have a secondary influence on the tides. The bay is shaped like a large natural funnel, as it becomes narrower and shallower towards the

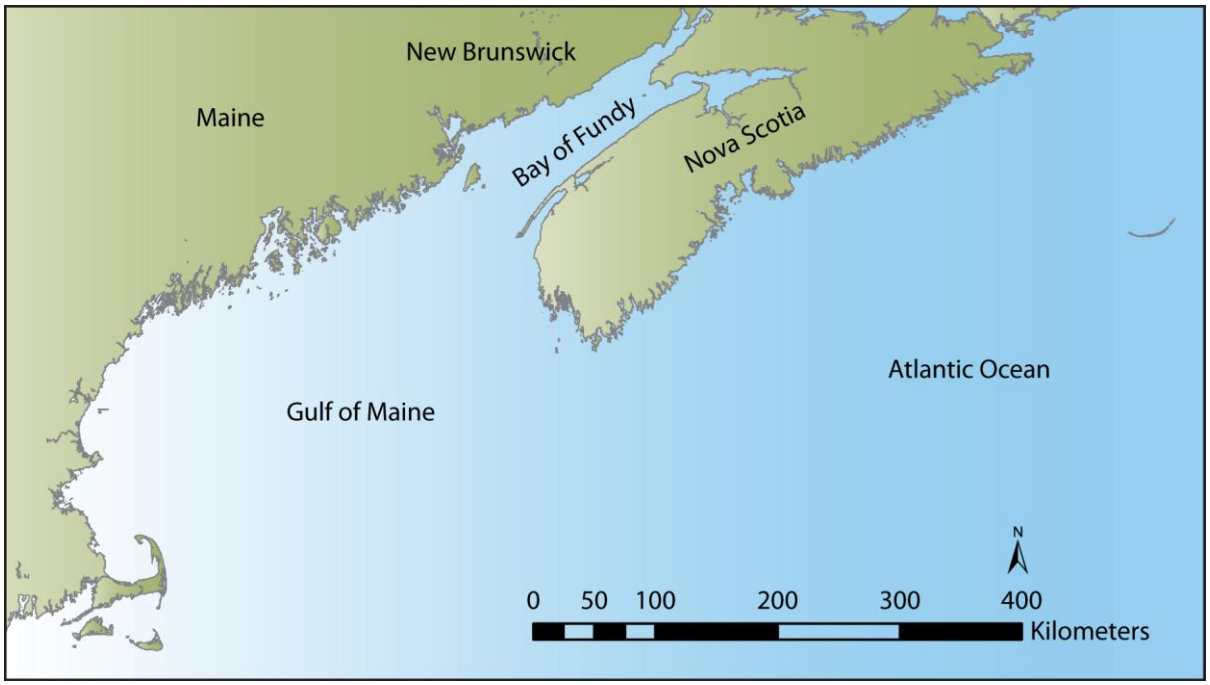

Figure 2.2: Region of the Bay of Fundy and Gulf of Maine.

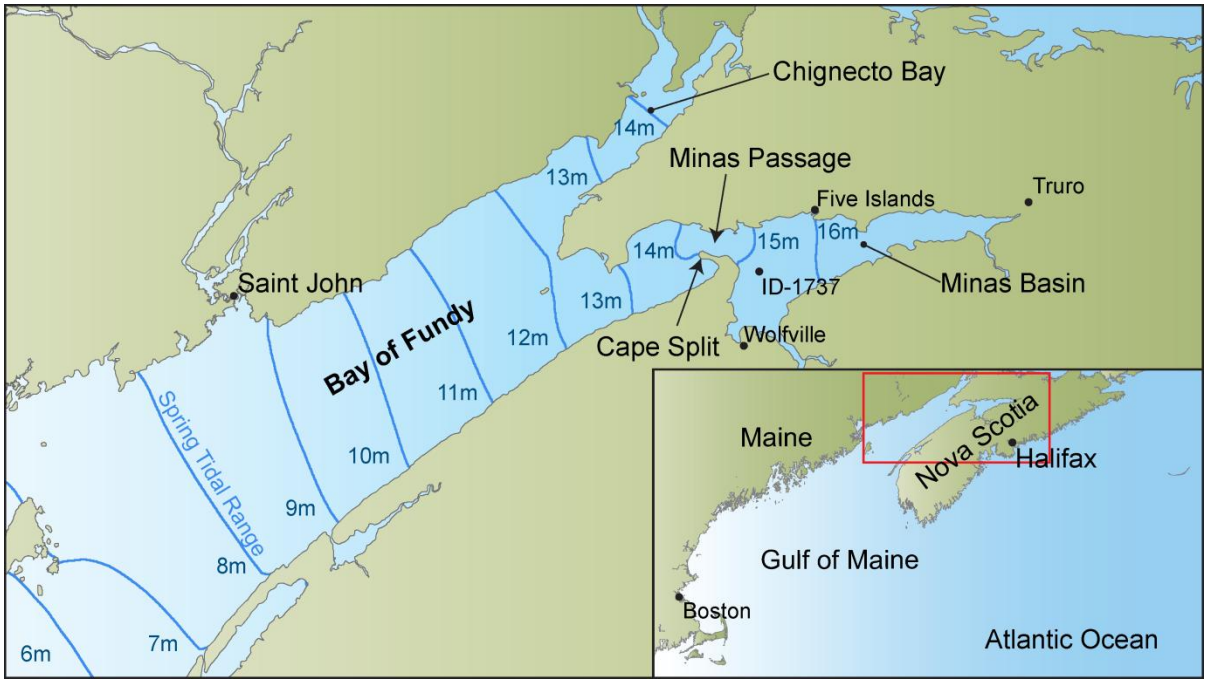

Figure 2.3: Tidal range in the Bay of Fundy.

upper end of the bay, forcing the water higher up onto its shores.

2.2.3 Tidal currents

Tidal bores form as the incoming tide flows upstream against the freshwater of the river, and even pushes upstream in some of the rivers which flow into Minas Basin (e.g., the Meander River near Windsor, east of Wolfville, and the Shubenacadie River and Salmon River near Truro). The most significant tides or current activities are found around Cape Split. This is located on the southern side of the entrance to Minas Basin, and, at its maximum flow, it experiences significant turbulence of the waters surging over some submarine ridges for a considerable distance. This maximum tidal current exceeds eight knots (4 m/s), and the flow rate through the deep, five kilometer-wide channel on the north side of Cape Split is about 4 km^3/hr. This kind of current reappears about three hours later in the opposite direction. In total, almost 14 billion tons (equivalent to 14 cubic kilometers) of muddy sea water flow in and out of the Minas Basin every six hours.

2.2.4 Numerical studies of flow characteristics in the Bay of Fundy

Several numerical studies have been conducted over the past decades to study the unique tidal behaviour in the Bay of Fundy. Rao (1968) and Garrett (1972) found that the natural wave period of the Bay of Fundy is close to the period of M2 tide. They concluded that the BoF together

with the GoM form a funnel with a natural period of approximately 13 hours, which is close to the 12.42 hours period of the M2 tidal forcing. These large tides are a result of the near resonant response of the BoF-GoM system to the M2 tidal forcing. This characteristic explains the significant tidal range in this region.

Greenberg et al. (1997) successfully developed a 3D finite element model for Passamaquoddy Bay to accurately predict flows. Sankaranarayanan et al. (2003) generated a 3D hydrodynamic model to simulate tidal circulation in the Saint John Harbour region. The model included five tidal constituents (M2, N2, S2, O1, K1) and achieved errors of less than 0.2 m in amplitude and 7° in phase for M2, except for the Minas Basin where the errors increased to 0.3–0.5 m (relative to an amplitude of 4.5–6 m). The errors in N2 (the next largest component) were 0.1–0.3 m in Minas Basin (relative to an amplitude of 0.7–1 m) with phase errors as large as 20° (roughly a 40-minute error in timing). Their model grid resolution ranged from 50–100 m in Saint John Harbour to 2–3 km in the Bay of Fundy.

Dupont et al. (2005) developed a high resolution model of the Upper Bay of Fundy to simulate both the the tides and the sea level. The model included the wetting and drying of the extensive tidal flats in Minas Basin and achieved a root-mean-square (RMS) error for the M2 tidal harmonic of less than 0.3 m (relative to tidal amplitude of 3 m at Saint John). The system can also simulate the series of total water level in Minas Basin with an RMS error of 0.3–0.5 m (relative to an amplitude of 4.5–6 m). Overall, the system is capable of an accuracy of ~10% in Minas Basin.

2.3 Tidal Power Projects in the Bay of Fundy

2.3.1 Introduction

Tidal energy is a form of hydropower that exploits the rise and fall in sea levels due to the tides, or the movement of water caused by the tidal flow. Tidal energy is classified as a renewable energy source because tidal forces are caused by gravitational attraction between the Earth, the Moon, and the Sun. Tidal power projects can be classified into two schemes: (1) the *dam or barrage scheme* which makes use of the potential energy from the difference in water level between high and low tides; and (2) the *tidal stream scheme* which makes use of the kinetic energy from the moving water currents.

Given the significant tidal range, the Bay of Fundy is considered a premier location for the development of tidal power. Other than the 12-16 meter tidal range, the surrounding environment and the social economic development of the region are also encouraging the use of the tidal power. Several proposals have been presented over the years to find economical ways to harness the power of the tides. They can be classified as *tidal barrage* projects, *tidal lagoon* projects, and *in-stream current turbine* projects.

2.3.2 Tidal barrage

Tidal energy has been harnessed in the past by the installation of barrages (dams), which resemble low head hydro-electric dams. Instead of impouding water on one side like a conventional dam, a tidal barrage first allows water to flow into the upstream bay or river during high tide, and then releases the water back at low tide. This operational cycle is performed by measuring the tidal flow and controlling the sluice gates at various times within the tidal cycle. Turbines are then placed within these sluices to capture the energy of the in and out flowing water. There are barrages that can capture energy only in one direction, either on the ebb or flow alone. There are also two-way tidal barrages that can capture energy in both flow directions. To read in more detail about the different power generation modes, the reader is directed to Section 2.4. The world's first constructed tidal power station, *La Rance,* is located on the estuary of the Rance

Figure 2.4: Aerial view of La Rance (France) tidal barrage. (www.wikipedia.org)

River in France (Figure 2.4). The tidal power station, built in the 1960s, has a two way generation system that has an installed power of 240 MW of electricity and which supplies 0.012% of the total power demand of France.

Lawton (1970) argued that a tidal barrage would be feasible under some conditions at two economically viable sites: the Minas Basin and the Cobequid Bay. Both sites had the potential of producing up to 6,000 MW. In the early 1970s, a committee entitled the Bay of Fundy Tidal Power Review Board (1974, 1977), was created to look into the feasibility and the environmental impacts of a potential large-scale tidal barrage in the Bay of Fundy. The Committee completed Phase I and Phase II of the assessment project. Phase I consisted of a series of technical and economic assessments aimed at determining the competitiveness of tidal power for this location. Phase II consisted of more in-depth technical, environmental, economic, as well as financial assessments of the projects selected based on the Phase I conclusions.

Previous modeling studies conducted by Garrett (1972), Greenberg (1977, 1979), DeWolfe (1986), and Sucsy et al. (1992), have focused on the potential impacts of constructing a tidal barrier in the Bay of Fundy. Garrett (1972) used the "resonance iteration" numerical method of Platzman, which neglects friction, with a grid size of approximately 25 km to determine the normal mode frequencies of the gulf and to estimate changes to the tides by tidal dam construction. He concluded that a tidal barrier placed in the Bay of Fundy would raise the M2 tide in the Gulf of Maine because the new system would be in closer resonance with the tide, and because of a change of shape of the normal mode. Garrett estimated an increase of 25% in the M2 amplitude at Boston if an impermeable barrier would be placed across Minas Basin. Greenberg (1977, 1979) used a conventional two-dimensional tide model with a nested finite-difference grid of 2.3 to 21 km scale to simulate the natural and post barrier installation tides. An accuracy of 0.15 m and 5° in phase was achieved in the Bay of Fundy, except for the Minas Basin where the phases and amplitude were greater than the ones observed. Greenberg estimated that an impermeable barrier placed across Minas Basin would increase the M2 tide at Boston by 33% or 40 cm. The model was extended by DeWolfe (1986) to include other constituents (N2, S2, O1, K1) and he found similar results to those of Greenberg (1979). Sucsy et al. (1992) used a two- and three-dimensional tide model to simulate the M2 tide with and without a tidal barrier in the Upper Bay of Fundy. Tidal amplitudes in the presence of a barrier increased 30-50 cm for both models, corroborating the results of previous studies by Greenberg (1979). The three-

dimensional model with tide barrier uniformly produced water levels of 3.5 cm (or 7%) less than the two-dimensional model.

Gordon et al. (1979) stated the changes in tidal amplitude could influence flooding and drainage of waters along the coast. They also indicated that the change in circulation pattern due to the construction of a tidal barrage will not only alter the transport and resuspension of sediment but also the erosion and deposition characteristics in both the tidal basin and seawards of it. Consequently, the impacts could damage land property along the coast and change the existing coastline. Some of the environmental impacts of the tidal barrages on marine life are similar to those induced by hydroelectric dams: a decrease in the tidal current speed as well as the prolonged high tide inside the catch basin. The result is that water quality could decrease, significantly affecting wildlife in the area.

For the reasons mention above, the development of barrages in the Bay of Fundy for the generation of tidal power was considered potentially hazardous to the surrounding ecosystem, it was never pursued. Although the development of a large-scale tidal power plant was not successful, a smaller-scale tidal power plant was completed at Annapolis Royal in 1984. The tidal power station has the capacity to generate 20 MW of electricity and supplies 1.0% of the power demand of the province of Nova Scotia.

2.3.3 Tidal lagoon

The concept of the **offshore tidal lagoon** is a recent approach to tidal power conversion that partially solves the environmental and economic problems of a tidal barrage (Figure 2.5). Rather than blocking an estuary with a barrage, the tidal lagoon uses an impoundment structure, making it completely self-contained and independent of the shoreline. The **coastal tidal lagoon** is another type of tidal lagoon, which operates similarly to tidal barrages in that they exploit the difference in tidal amplitude to generate electricity. However, the structures do not fully obstruct the estuary, but it uses the shoreline to form part of the lagoon's edge.

Tidal lagoon can be built in the form of a closed dike (rubble mound type, with an impermeable element). The lagoon holds water at high tide and creates power by releasing the water back into the sea at low tide through conventional hydroelectric turbines and then repeating the cycle at high tide by refilling the lagoon. Tidal lagoons could have benign or minimal impacts on marine environment and could potentially foster biodiversity by creating new habitats for fish, birds and marine wildlife. Although tidal lagoons are generally thought to be achievable from an engineering perspective, there are currently no examples of tidal lagoon development anywhere in the world.

Commissioned by Tidal Electric Canada, Delta Marine Consultants (DMC) (2007) studied the feasibility of constructing a tidal lagoon in Minas Basin. DMC proposed constructing a tidal lagoon on the tidal flats located along the northern shore of Minas Basin, between Five Islands and Economy Point (Figure 2.5). Various tidal plant layouts were investigated, including tidal lagoons with single and multiple basins as well as tidal lagoons with a direct and rectified flow through the power station. They concluded that a single basin with a direct flow through the power station would be most cost efficient for the analyzed Minas Basin site.

DMC developed conceptual designs for two lagoon types: a) an offshore lagoon comprising a power station and a 12 km^2 circular impoundment enclosed by a 11.9 km long dike detached

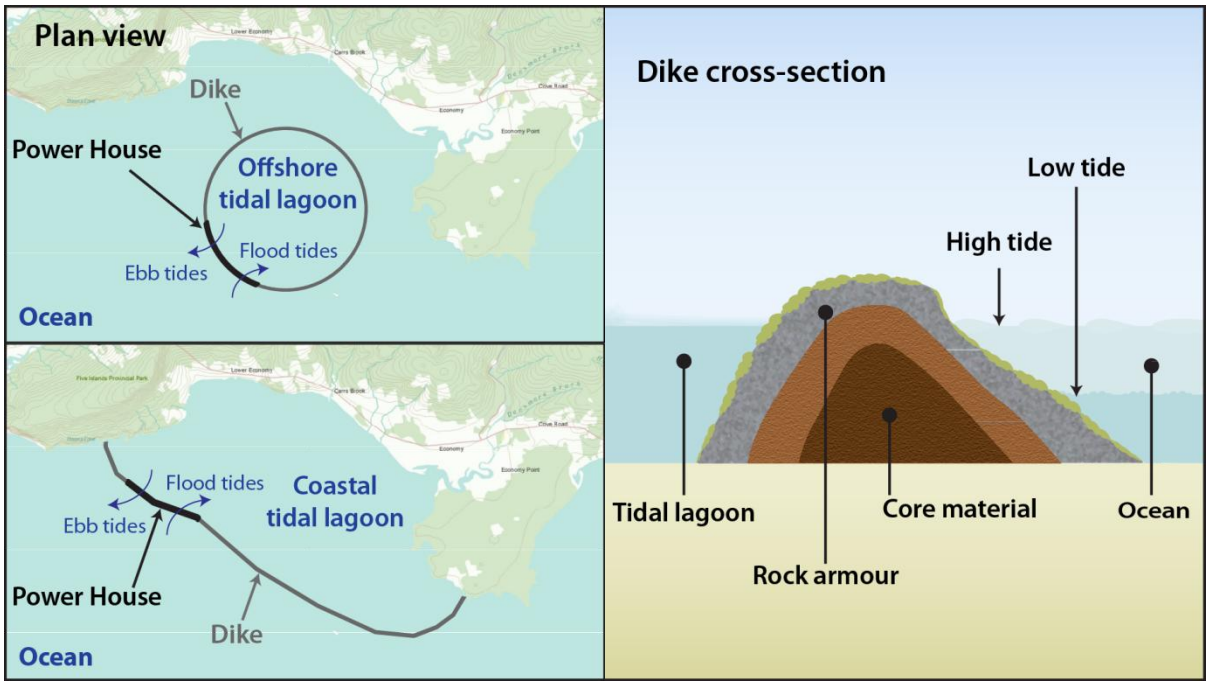

Figure 2.5: Examples of offshore and coastal tidal lagoons.

from the shore; and b) a coastal lagoon comprising a power station and a 24 km^2 impoundment space formed between a 10.2 km long dike and the existing shoreline (Figure 2.5). According to DMC, a 12 km^2 offshore lagoon fitted with fourteen 7.5 m diameter bulb turbine generators (up to 20 MW each) and 15 sluice gates (56 m^2 area each) would have an average power output of approximately 124 MW. The larger coastal lagoon, equipped with twenty-four 20 MW bulb turbines and 15 sluices, was estimated to have an average power output of approximately 220 MW.

Although DMC's study intended to assess the technical feasibility study of a tidal power plant in the Minas Basin, the scale and character of the potential hydrodynamic impacts due to the presence of a single or multiple tidal lagoon(s) operating in the Upper Bay of Fundy have not been previously investigated and remain unknown. Tidal lagoon operating in the Upper Bay of Fundy would modify the tides and tidal currents near the lagoon, and possibly create effects that would be felt throughout the entire Bay of Fundy and Gulf of Maine. The nature of these hydrodynamic impacts would likely depend on the size of the tidal lagoon, its location, and its method of operation. Any changes in the tidal hydrodynamics caused by a tidal lagoon may also impact on the transport of sediments throughout the region, and possibly upset ecosystems that are presently well adapted to existing conditions.

2.3.4 In-stream tidal current turbine

In-stream tidal current turbine is a relatively new technology which makes use of the kinetic energy of the moving tidal currents to generate electricity (Figure 2.6). The concept is similar to wind turbines except a single generator can provide significant power since the water density is 832 times higher than the density of air. The location of the tidal stream system is critical for a tidal stream power generator: the system needs to be located in areas with fast currents to make it economically feasible. On the other hand, safe installation, operation and maintenance could also be difficult if the flows are excessively strong.

The kinetic energy resources due to tidal currents throughout the Bay of Fundy have been investigated by Cornett (2006), Hagerman et al. (2006) and Cornett et al. (2010). Tidal current resources are best characterized by the mean power (calculated as mean of instantaneous power), which represents an integration or averaging of temporal fluctuations over time. The mean power density characterizes the average intensity of the flow at the site. Cornett (2006) has estimated an average power density of 6 kW/m^2 in Minas Passage.

Nova Scotia Power has partnered with Irish firm OpenHydro to explore a new source of tidal energy for Nova Scotia. As part of a test project that will help to determine the feasibility of harnessing tidal energy on a commercial scale, NS Power has deployed a 10-metre, 1 MW in-stream tidal turbine in the Minas Passage.

Sutherland et al. (2007) mentioned that harnessing the power from tidal currents is cheaper and more ecologically sustainable. While the environmental impact may not be as noticeable in a single water turbine, water turbine farms could change the nature of the tidal current overtime. Karsten et al. (2008) used hydrodynamic modeling to show that over 5,000 MW of power could be extracted from Minas Passage, and that the scale of the associated impacts would be proportional to the amount of energy removed from the natural system. As for marine life, Allard (2004) stated that fish in the area, which rely on the current to orient themselves, could get disoriented and even struck by the blades of the turbine depending on the design.

The physical and ecological impacts of removing energy from natural tidal flows must be carefully assessed before reliable predictions can be made concerning the size of the extractable kinetic energy resource at any site. Good information on the physical and ecological impacts of removing various amounts of energy from particular locations must be collected before such an assessment could be made.

Figure 2.6: In-stream tidal current turbine. (Courtesy of OpenHydro)

Nova Scotia is in the process of assessing potential environmental impacts of in-current tidal technology and is working with technology developers from around the world to select the best devices for the region. All of this process is initiated by FORCE (Fundy Ocean Research Centre for Energy), which is Canada's leading research centre for in-stream tidal energy.

2.4 State of knowledge – Design and modeling tidal lagoons

2.4.1 Design components

idal lagoons are very similar to hydro-electric dams. Instead of damming water on one side like a conventional dam, a tidal lagoon first allows water to flow into the lagoon during high tide, and releases the water back in the surrounding ocean during low tide. This release is controlled by measuring the tidal flow and controlling the sluice gates at key intervals. The design of a tidal lagoon has three main components: dikes, sluices, and turbines/generators.

2.4.2 Dikes

Dikes are impoundment structures designed to separate the tidal lagoon from the surrounding ocean. These structures must be able to dissipate and protect against wave attack to maintain their structural and functional integrity. This is done either by using massive self-supporting structures (e.g. concrete caissons) or by using a revetment slope protection (e.g. with rock or concrete armour units). Caisson breakwaters typically have vertical sides and are often used where it is desirable to berth one or more vessels on the inner face of the breakwater. They use their own mass (the caisson and the fill within it) to resist the overturning forces induced by waves. They are relatively expensive to construct in shallow water, but in deeper locations they can offer significant savings over rouble mound breakwaters. Rubble mound breakwaters use the voids in the structure to dissipate the wave energy. Rock or concrete armour units on the outside slope of the structure absorb most of the energy, while gravel or sand is used to prevent the wave energy being transmitted through the breakwater core. The slopes of the revetment are typically between 1:1 and 1:5, depending upon the materials used, as described by Baker (1991). In shallow water, revetment breakwaters represent a preferred solution due to cheaper costs, but as water depth increases, the design requirements become more complex and, hence, costs increase significantly.

2.4.3 Sluices

Sluices, flow openings fitted with control gates, are designed to control water levels in the tidal lagoon. Unlike conventional hydroelectric sluices, tidal-electric sluices must open and close in accordance to the operation mode. They must be capable of rapid, frequent operation and be as free as possible from maintenance and operating problems. As explained by Baker (1991), it is also essential that the gate setting ensures adequate submergence at all times to avoid damages or operational difficulties through wave impact and corrosion of the gate mechanisms or ice jamming and freezing in regions where this occurs.

2.4.4 Sluice modeling for tidal power projects

To simulate adequately the hydrodynamic processes caused by the sluices, Falconer et al. (2009) and Xia et al. (2010a, 2010b, 2010c) applied the orifice equation, Equation (2.1), to approximate the discharge-water head relationship.

$$Q = C_d A\sqrt{2g\Delta H} \tag{2.1}$$

where Q is the discharge (m^3/s), C_d is the discharge coefficient, A is the wet flow-through area (m^2), g is the gravitational acceleration (m/s^2), and ΔH is the water head difference (m). Severn Barrage Committee (SBC) (1981) and Severn Tidal Power Group (STPG) (1993) performed physical model studies on tidal sluices and determined an averaged discharge coefficient of 3.0 and 1.8, respectively. In previous hydrodynamic modeling, Falconer et al. (2009) and Xia et al. (2010a, 2010b, 2010c) applied a constant discharge coefficient of 1.0 to 1.2.

The orifice equation is a simple equation, easy to implement, and computationally efficient. Although this type of equation provides quick results, they must be treated with caution. The extent to which the results will differ from the realistic results depends largely on the dimensions and the position of the sluices. If sluices are positioned well below the water level, they will most likely behave like an orifice. Otherwise, they will behave similar to a culvert.

A typical longitudinal section of a culvert is shown in Figure 2.7. Culverts are structures that allow water to pass underneath a road, railway, or embankment. In fact, they are very similar to sluices. As explained by Normann (1985), the discharge through a culvert is controlled by either inlet or outlet conditions. Inlet control means that flow through the culvert is limited by culvert entrance characteristics. Outlet control means that flow through the culvert is limited by friction between the flowing water and the culvert barrel. The term "outlet control" is a bit of a misnomer because friction along the entire length of the culvert is as important as the actual outlet condition (the tailwater depth). Inlet control most often occurs for short, smooth, or greatly downward sloping culverts. Outlet control governs long, rough, or slightly sloping culverts. The type of control also depends on the flow rate. For a given culvert installation, inlet control may govern for a certain range of flows while outlet control may govern for other flow rates.

The equations below, Equation (2.2) to Equation (2.5), are solved simultaneously to determine the headwater depth (Y_h) for known flowrate (Q_p) and tailwater depth (Y_t). The headwater depth is computed independently, based on inlet and outlet control equations. The equation that gives the larger value of Y_h is considered to be the controlling condition.

For non-submerged inlet control, the equation suggested by Normann (1985) is:

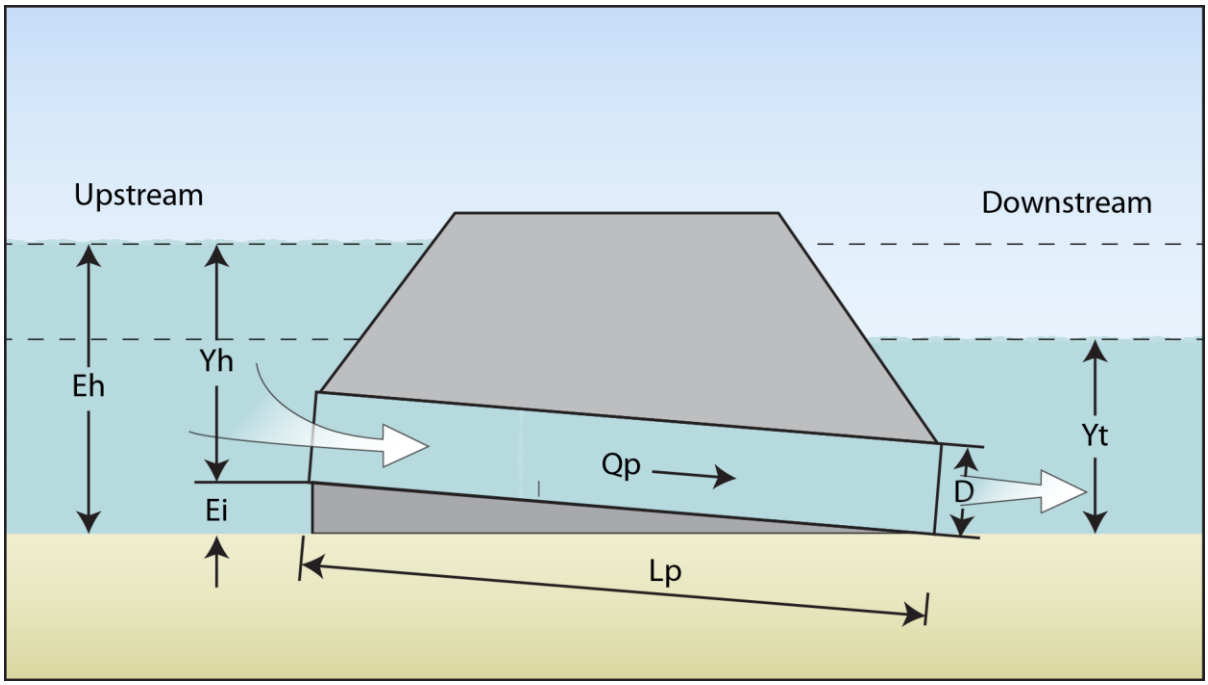

Figure 2.7: Culvert diagram.

$$Y_h = Y_C + \frac{V_c^2}{2g} + D\left[C_1\left(\frac{4Q_p}{\pi D^{5/2}}\right)^{C_2} + CS_p\right] \; for\; Y_h < D \tag{2.2}$$

where Y_C is the critical water depth (m), V_C is the velocity based on critical depth (m/s), D is the diameter (m), C_1, C_2, C_3 are non-submerged inlet constants, S_p is the longitudinal slope (m/m), A_c is the flow area based on critical depth(m^2). The critical depth is given by:

$$1 = {Q_p}^2 \cdot \frac{T_c}{g \cdot {A_c}^3}$$

where

$$T_c = 2 \cdot r \cdot \sin\theta_c$$

$$A_c = (\theta_c - \cos\theta_c \cdot \sin\theta_c) \cdot r^2$$

$$\theta_c = arccos\left(1 - {Y_c}/{r}\right)$$

T_c is the top width of flow based on critical depth (m), A_c is the flow area based on critical depth (m^2), θ_c is the partially full angle based on critical depth, and r is the radius. Since Q_p is known, the above equations are solved numerically for Y_c. For submerged inlet control, the equation proposed by Normann (1985) is:

$$Y_h = D\left[C_4\left(\frac{4Q_p}{\pi D^{5/2}}\right)^2 + C_5 + C_3 S_p\right] \; for\; Y_h \geq D \tag{2.3}$$

where C_4, C_5 are submerged inlet constants. For non-submerged outlet control, the equation proposed by Chow (1959) is:

$$Q_p = \frac{1.49A\sqrt{S_p}}{n_p}\left(\frac{A}{P}\right)^{2/3} \; for\; Y_h < 0.93D \tag{2.4}$$

where A is the flow area(m^2), S_p is the slope of the culvert (m/m), n_p is the Manning coefficient, θ is he partially full angle (rad), P is the wetted perimeter (m). The flow area, the partially full angle, and the wetted perimeter equations are:

$$A = (\theta - \cos\theta \sin\theta) \cdot r^2$$

$$\theta = arccos\left(1 - {}^{Y_h}/_{r}\right)$$

$$P = r \cdot \theta$$

Since Q_p is known, the above equations are solved numerically for Y_h. For submerged outlet control, the equation proposed by Normann (1985) is:

$$Y_h = Y_o + H - E_i \; for \; Y_h \geq 0.93D \tag{2.5}$$

where Y_o is the water outlet depth (m), H is the head loss computed from outlet control equation (m), E_i is the elevation of culvert inlet invert relative to culvert outlet invert (m). The water outlet depth, head loss and E_i are :

$$Y_o = Max(Y_t, Y_{avg})$$

$$H = \left[1 + K_e + 29 n_p^2 L_p \left(\frac{4}{D}\right)^{1.33}\right] \frac{8Q_p^2}{g\pi^2 D^4}$$

$$E_i = L_p S_p$$

where Y_{avg} is the average water depth (m), K_e is a minor loss coefficient, L_p is the length of culvert (m), and S_p is the slope of the culvert (m/s). The average water depth can be expressed as:

$$Y_{avg} = \frac{Y_c + D}{2} \; for \; Y_c < D$$

$$Y_{avg} = D \; for \; Y_c \geq D$$

2.4.5 Turbines and generators

Turbines and generators are designed to convert potential energy of the difference in water levels into electricity. The first turbines considered for tidal power were based on the vertical axis Kaplan's turbine. This design offered the advantages of good efficiency over a wide range of flows and heads, with the generator mounted in the dry above the turbine, easy cooling and good access for maintenance. Figure 2.8 shows a typical arrangement of this type of turbine. The main disadvantage lies in the water passing through the turbine having to turn through 90° bends twice and wasting potential energy. In order to reduce these losses, other types of turbine

were considered, namely the straight-flow (Straflo) or rim-generator turbine, the tubular turbine, and the bulb turbine.

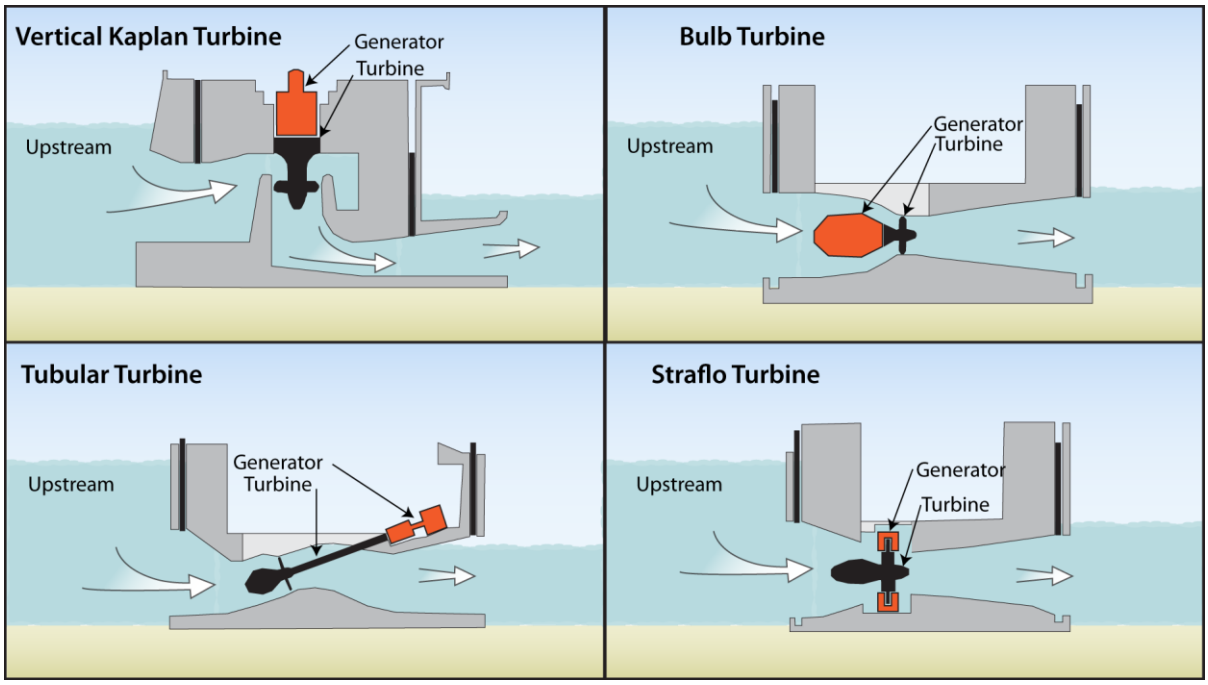

Figure 2.8: Types of turbines.

Bulb turbine: Bulb turbines operate in a straight water passage with the generators enclosed in watertight steel bulbs upstream of the Kaplan type runners. Figure 2.8 shows a typical arrangement of a bulb turbine with directly-driven generator. The assembly is made up of stay vanes, adjustable wicket gates, and variable-pitch runner vanes on a horizontal shaft, thereby providing double regulation. Bulb turbines have been significantly advancing in the field of low-head hydro developments, enabling the exploitation of heads between about 1.5 to 20 m. Its characteristics are well developed and almost all recent installations for large, low-head, river schemes have used bulb turbines. The success of these machines combined with the great amount of experience with all sizes on non-tidal projects, means that this type is generally favoured for large tidal power schemes.

Tubular turbines: Figure 2.8 shows a typical outline design of a tubular turbine. The purpose of the design is to move the generator from the water passage into a dry enclosure. This is achieved by a long shaft connecting the Kaplan's runner at an angle through the wall of the water passage.

No serious consideration is being given to the use of tubular turbines for tidal power because of the general superiority of the bulb type.

Straight-flow (Straflo) turbine: The concept is illustrated in Figure 2.8. The turbine runner is of Kaplan's propeller type, mounted horizontally. The generator rotor is supported on the tips of the runner blades and outside the rotor is the stator. Most straight-flow turbines were developed for relatively small runner diameters of the order of 1 m.

2.4.6 Turbine and power modeling for tidal power projects

Turbines and generators for tidal power schemes are a commercially sensitive subject where manufacturers are reluctant to disseminate their design. The designer of a tidal power project has to approach manufacturers directly to assess the most appropriate design for the particular circumstances of tidal range, water depth and available volumes of water that apply to that site. The standard formula for computing the generating power, P, can be expressed as

$$P = \rho g Q H \eta \tag{2.6}$$

where ρ is the density (kg/m^3), H is the water head (m), and η is the efficiency. To calculate the power, Xia et al. (2010a, 2010b, 2010c) applied the orifice equation, Equation (2.1) , with a discharge coefficient of 1.0 to calculate the discharge. Although the power can be directly calculated from Equation (2.6), the performance of a turbine is often defined as a hill chart, relating specific discharge, unit speed and efficiency. These are based largely on physical and computational fluid dynamics models.

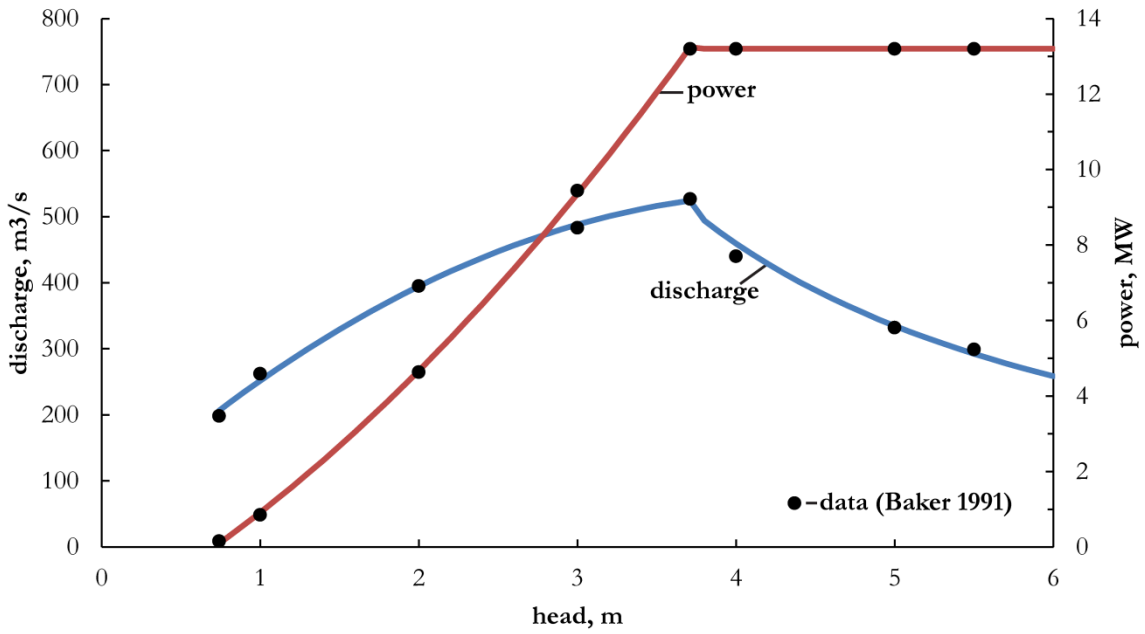

Figure 2.9: Notional double-regulated turbine characteristics.

As proposed by Baker (1991), turbine performance curves can be developed based on the simplified relationship between the water head, discharge and potential maximum power, as shown in Figure 2.9. This figure was derived from Table 2.1 given by Baker (1991). The relationship is based upon a double-regulated bulb turbine with a runner diameter of 8 m, a maximum power output to the generator of 13.4 MW, which would be suitable for a maximum head of 5.5 m and a normal operating head around 3.5 m. The maximum turbine efficiency considered is 80%.

Table 2.1: Example of turbine performance, Baker (1991).

H (m)	Q (m3/s)	η (%)	P (MW)
0.74	198	10	0.15
1	262	32	0.85
2	395	58	4.63
3	483	64.5	9.44
3.71	527	67	13.2
4	440	74	13.2
5	332	79	13.2
5.5	299	79.5	13.2

As shown in Figure 2.9, the power increases with an increase in head up to a maximum value of 3.71 m. The power remains constant after reaching the maximum head at a value of 13.2 MW. The flow discharge through the turbine also reaches its maximum value when the head is around

3.71 m and decreases for higher water head. Table 2.2 summarises theoretical turbine performance relationships.

Table 2.2: Turbine performance relationships.

Output (1)	Relationship (2)	Flow conditions (3)
Power (MW)	$P = 0$	$H < H_{min}$
	$P = 0.462 \cdot H^2 + 2.372 \cdot H - 1.921$	$H_{min} \leq H \leq H_{normal}$
	$P = 13.2$	$H > H_{normal}$
Discharge (m3/s)	$Q = 0$	$H < H_{min}$
	$Q = -24.777 \cdot H^2 + 217.270 \cdot H + 59.204$	$H_{min} \leq H \leq H_{normal}$
	$Q = 3270 \cdot H^{-1.416}$	$H > H_{normal}$

Notes: H_{min}: Minimum operating head; H_{normal}: Normal operating head.

2.4.7 Different tidal power project operating modes

A tidal power plant can be designed to operate under various modes which usually include the modes of ebb generation, flood generation, two-way generation, single-basin, and multi-basins.

Ebb generation: The mode of ebb generation represents the operation of the turbines such that power is only generated when the direction of flow is the same as that of the ebb tide, usually from the tidal lagoon (basin) towards the ocean. A full operating process of ebb generation includes the four stages: (i) holding, (ii) generating, (iii) holding, and (iv) filling, as shown in Figure 2.10. These stages can be described as:

(i) Turbine and sluices gates are kept closed until the sea level falls to create sufficient head (i.e., the starting head) across the tidal basin (holding stage 1 to 2);

(ii) Turbine gates are opened so that the turbines generate power until the head is again low, with the low water head being often defined as the minimum head required for turbine operation (generating stage 2 to 3);

(iii) Sluices and turbine gates are closed again due to the low head until the sea level is greater than the basin level (holding stage again 3 to 4); and

(iv) Tidal basin is filled through the sluices until high tide, and then the sluice gates are closed (filling stage 4 to 1).

Flood generation: The mode of flood generation means that power is generated when the discharge direction through the turbine is in the same direction as the flood tide, i.e. from the ocean to-

wards the enclosed basin. The sketched operating mode is as shown in Figure 2.11. Therefore, flood generation is virtually a mirror image of ebb generation. However, the former is generally much less efficient than the latter, because the volume contained in the upper half of the basin (which is where ebb generation operates) is greater than the volume of the lower half (filled first during flood generation). Therefore, the available level difference between the basin side and the seaward side reduces more quickly than it would for the mode of ebb generation.

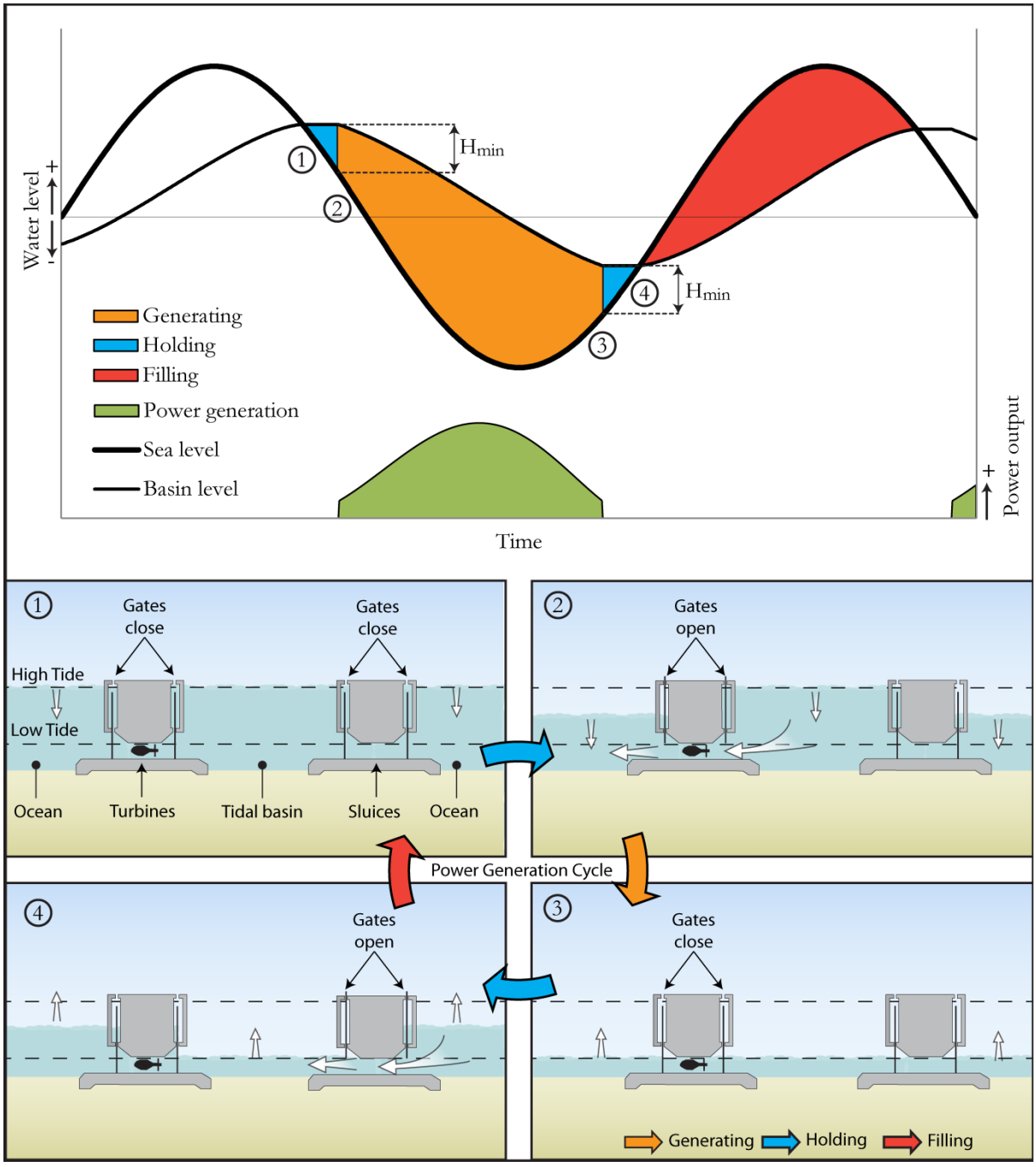

Figure 2.10: Ebb generation.

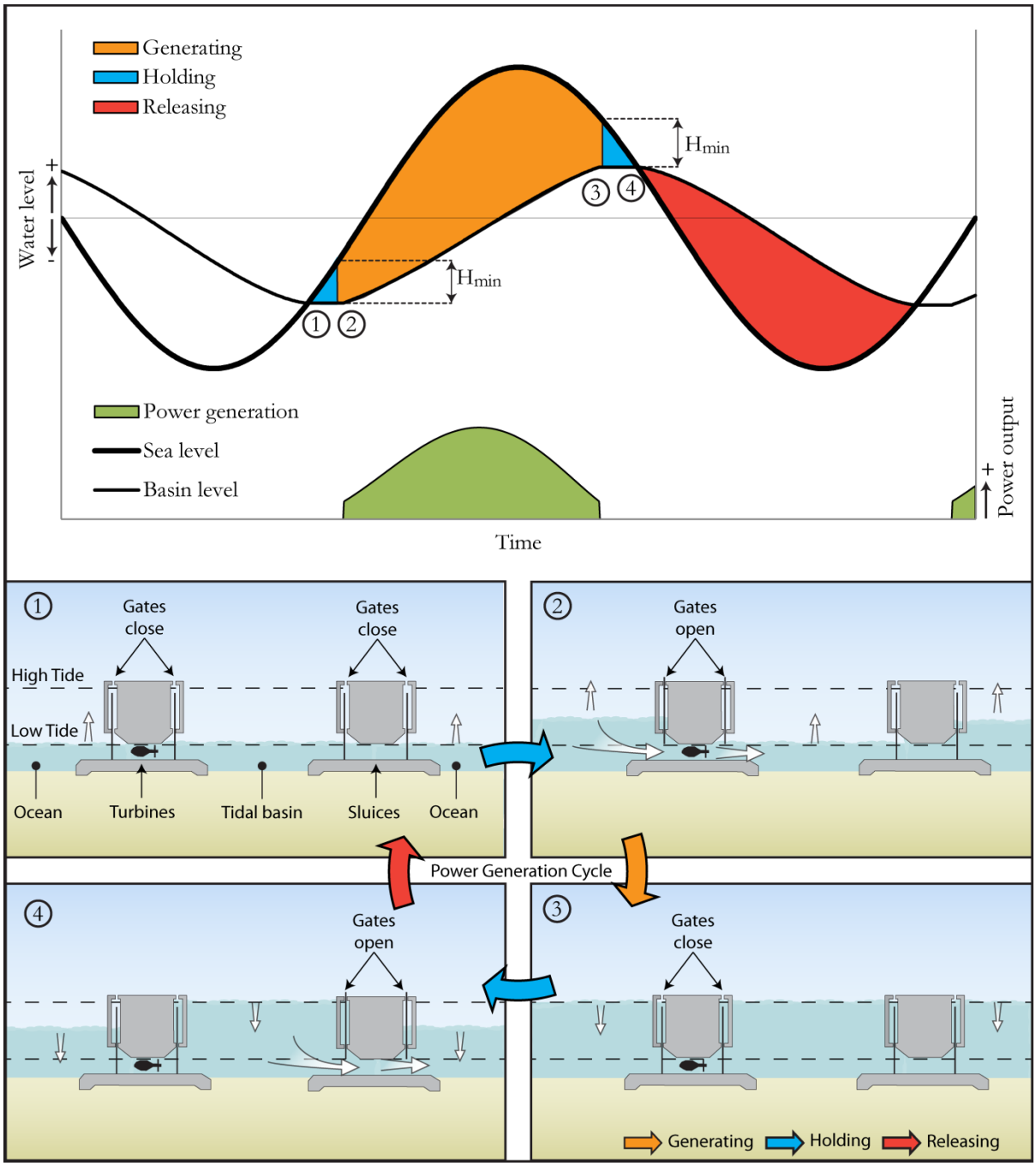

Figure 2.11: Flood generation.

Two-way generation: The mode of two-way generation is relatively complicated compared with the other operating modes. The sketched operating mode is shown in Figure 2.12. A full operating process of two-way generation includes 8 stages:

(i) Both the turbine and sluices gates are kept closed until the sea level falls to create sufficient head (i.e. the starting head) across the tidal basin (holding stage 1 to 2);

(ii) The turbine gates are opened and operate in a mode of ebb generation (ebb generating stage 2 to 3).

(iii) Towards the end of the ebb generation, the sluices are opened in order to draw down the water level in the basin by allowing enough water to flow from the basin to the ocean. This process has to be included if a reasonably large difference in the water levels is to result during the next flood generation phase (generating and releasing stage 3 to 4).

(iv) Turbine gates are closed due to the low head but sluices gates are kept opened (releasing stage 4 to 5).

(v) Following low tide, at the instant when the ocean and basin levels are equal, the gates are closed and the basin level remains constant until the optimum difference in levels is reached for the next phase of generation (holding stage 5 to 6).

(vi) The turbine gates are opened and operate in the flood generation mode (flood generating stage 6 to 7).

(vii) Towards the end of the flood generation, the tidal basin is filled through the sluices until high tide, and then the sluice gates are closed (filling stage 7 to 8).

(viii) Turbine gates are closed due to the low head but sluices gates are kept opened (filling stage 8 to 1).

For this scheme, the tidal range within the tidal basin is much closer to the natural range and is generally regarded as being more acceptable in terms of minimizing environmental changes.

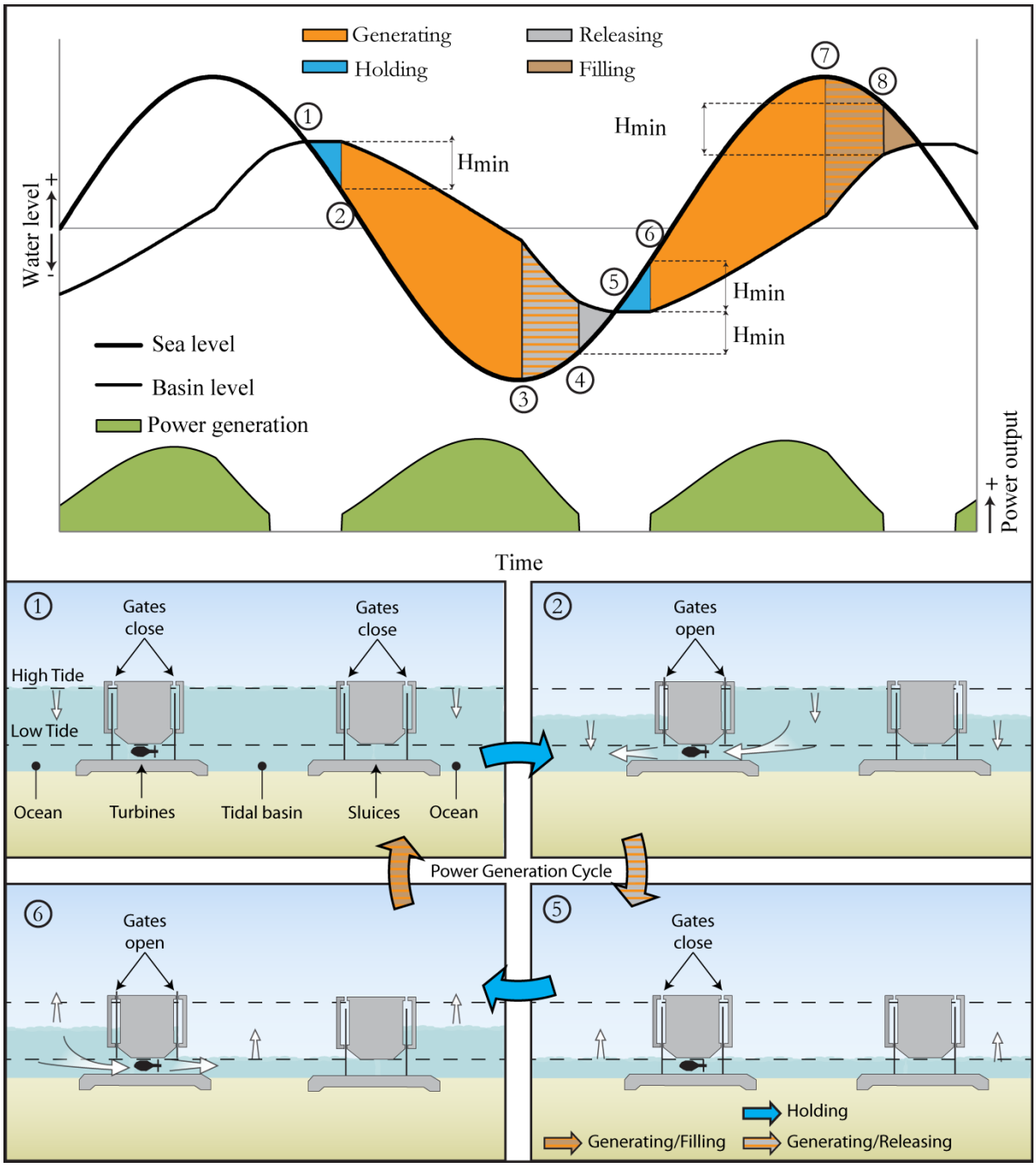

Figure 2.12: Two-way generation of tidal lagoons.

Single basin: The single-basin scheme is less complex and less expensive compared to the multi-basins scheme. However, the single-basin concept cannot produce constant, stable power throughout the day since it varies depending on the tidal cycle. It is possible, depending on the time and day, that such a system could generate power at a low peak demand. The problem of discontinuous energy output from a single-basin scheme can be overcomed by using a multi-basin layout.

Multi-basins: There are many possible multi-basin designs to generate continuous electric power. An example for such design would involve constructing two basins where one is larger than the other. Both basins would have a set of gates link with the ocean and one set of gates linked to each other. The power would be generated with the set of gates between the two basins where the larger basin would fill during high tide, and the smaller basin would empty during low tide. Thus, the larger basin would act like a reservoir. The water level in the larger basin must always remain higher than one in the smaller basin in order to make the system work. A major drawback of multi-basins, however, is that the energy production is less than that resulting from a single-basin scheme using either of the basins separately.

2.4.8 Impact of different operating modes

Xia et al. (2010b) used an existing two-dimensional hydrodynamic model with the integration of a new algorithm to estimate the tidal power output. The algorithm accounted for three barrage operating modes, including ebb generation, flood generation, and two-way generation. Predicted results indicated that the mode of flood generation would produce the least electrical energy and cause a larger reduction in the maximum water levels upstream of the tidal barrage. Two-way generation would provide an improvement, and would produce an equivalent amount of electricity to that obtained from ebb generation, with a low installed capacity and a small loss of intertidal zones. Therefore, the mode of ebb generation or two-way generation would appear to be a preferred option for power generation, because both would offer benefits of acceptable electrical energy and reduced flood risk.

2.5 Hydrodynamic modeling – A brief review

2.5.1 Hydrodynamic models

Hydrodynamics is the study of motion of liquids, and in particular case, of water. A hydrodynamic model is a tool able to describe or represent in some way the motion of water. Prior to

the advent of computers, the effects of marine projects on tidal flows have been investigated with the help of physical models. Although physical models are still widely used, for example in port developments, their use for tidal power projects has been limited. One reason is that the tidal power operation, particularly that of the turbines, is difficult to model accurately at the small scale needed. Another reason is that the time needed to set up and carry out a test is much longer, and therefore, inherently more expensive.

There are four basic types of hydrodynamic numerical models for tidal lagoons:

1. Box-type (0-D) models
2. One dimensional (1-D) dynamic models
3. Two-dimensional (2-D) dynamic models
4. Three-dimensional (3-D) dynamic models.

Each type is described and discussed below.

Box-type models: This type of model is the simplest. Such a model does not describe the motion of fluids. The model is based on the assumptions that a volume of water let into the basin will raise the level of the basin by an amount equal to the volume let in divided by the area of the basin at the time, i.e., the water would spread uniformly over the basin. Thus, the basin is defined by a simple depth curve. The tide on the seaward side is assumed to be unaltered by the flows into or out of the tidal basin. This type of model is quick to operate. Although important simplifying assumptions are built in, a large number of tests can be carried out quickly. This type of model is therefore very useful at the start of a study, enabling alternative tidal basin arrangements, different numbers and sizes of turbines, their generator capacity, different types of turbines, different operating principles and different sluice areas to be tested and compared. Although this type of model provides quick results, they must be treated with caution. The extent to which the results will differ from the real world depends largely on the size and location of the tidal lagoon. Large dynamic effects due to power extraction could alter the tide characteristics. This type of model was used by Delta Marine Consultants (DMC) (2007) in their study.

3-D dynamic models: These hydrodynamic dynamic models use the Navier-Stokes equations that describe the motion of fluids. These equations are derived from Newton's laws of motion and describe the action of forces applied to the fluid; that is, the resulting changes in flow characteristics as a result of these forces. This is the conservation of momentum represented by Newton's

second law: the acceleration is dependent upon the force exerted and is inversely proportional to its mass. These equations also involve the continuity principle: mass and energy are conserved, unless they pass out of the domain. Such models are used in coastal modeling when vertical accelerations cannot be ignored.

2-D dynamic models: For 2-D depth-integrated hydrodynamic models, the Navier-Stokes equations are simplified in the form of the shallow water (or Saint-Venant) equations, called as such since the scale of features in horizontal direction is much greater than in the vertical one. This type of model is the extensively used for coastal and ocean modeling.

1-D dynamic models: For 1-D depth-integrated and width–integrated hydrodynamic model, the Navier-Stokes equations are further simplified such that flow velocities do not vary with depth or width. One-dimensional models are rarely (if ever) used in coastal and ocean modeling.

Previous modeling studies, Greenberg (1979), Sucsy et al. (1992), Sankaranarayanan et al. (2003), and Dupont et al. (2005), have used both 2-D and/or 3-D models to simulate the hydrodynamics in the Bay of Fundy. Sucsy et al. (1992) developed a two-dimensional and three-dimensional finite element model to simulate the effects of a tidal barrier in the Upper Bay of Fundy using the tides in the Gulf of Maine. The study shows tidal amplitudes in the presence of a barrier increased 30-50 cm for both models. The three-dimensional model with tide barrier produced water levels of 3.5 cm (or 7%) less than the two-dimensional model. The study demonstrates that the vertical circulation due to the tide is less significant than the horizontal movement in the Bay of Fundy. Therefore, a two dimensional model is assumed sufficient to describe the hydrodynamics of such tidal bays for tide-generation purposes.

2.5.2 Computational grids

Most numerical methods reproduce the physical domain by separating it into numerous components through a discretization process that produces in a model grid. Two types of computational grids are commonly used in hydrodynamic dynamic models: structured grids (primarily finite difference algorithms) and unstructured grids (including finite element and finite volume methods).

Structured grid models tend to use quadrilateral grid cells that limit the grid's flexibility in resolving the complex shoreline but they are characterized by their straightforward and efficient algo-

rithms. The work presented by Greenberg (1979) and Sucsy et al. (1992) are typical examples that made use of regular rectangular grid.

Unstructured grid models have much more flexibility in varying their grid resolution by employing variable triangular elements, but tend to be more time consuming to run and more sensitive to numerical errors. Recent studies such as the ones of Xia et al. (2010a, 2010b, 2010c) and Falconer et al. (2009) used an unstructured grid to represent the natural topography, as well as irregular boundaries, tidal barrages and tidal lagoons.

2.5.3 Boundary condition

Most estuarine and coastal models have two types of boundaries: landward boundaries and seaward boundaries. The seaward boundary is usually an open boundary, where water levels are specified at each time step, while the landward boundary is a solid boundary. In the study performed by Falconer et al. (2009), an open boundary was specified at some landward boundary along the Severn Estuary to represent a river inflow.

2.5.4 Hydrodynamic impacts of different tidal power projects

Two versions of the hydrodynamic model are required to investigate the potential impacts generated by tidal lagoon projects. The first grid represents the existing conditions without the presence of tidal lagoons. The model is calibrated by adjusting the value of the roughness coefficient throughout the computational domain and by subsequently comparing predicted tidal water levels and current velocities at different sites with observed (field) data. The second model is developed to account for the implementation of tidal lagoons. Usually, the computational grid is refined in the vicinity of the lagoons in order to ensure it a higher resolution and a more detailed investigation of the flow and water levels at locations of interest.

Garrett (1972) used the "resonance iteration" numerical method of Platzman, which neglects friction, with a grid size of approximately 25 km to determine the normal mode frequencies of the Gulf of Maine and to estimate changes to the tide levels induced by tidal dam construction. He concluded that a tidal barrier placed in the Bay of Fundy would raise the M2 tide component in the Gulf of Maine because the new system would be in closer resonance with the tide, and because of a change of shape of the normal mode. Garrett estimated an increase of 25% in the M2 amplitude at Boston if an impermeable barrier would be placed across Minas Basin.

Greenberg (1977, 1979) used a conventional two-dimensional tide model with a nested finite-difference grid of 2.3 to 21 km grid scale to simulate the existing and post barrier tides. An accuracy of 0.15 m and 5° in tide phase was generally achieved in the Bay of Fundy, except for the Minas Basin where the differences in phase and amplitudes were greater than the ones observed. Greenberg estimated that an impermeable tidal barrier placed across Minas Basin would increase the M2 tide at Boston by 33%, equivalent to a change in level of 40 cm. The model was extended by DeWolfe (1986) to include other tidal constituents (N2, S2, O1, K1) and he found similar results to those of Greenberg (1979).

Sucsy et al. (1992) used two- and a three-dimensional tide models to simulate the M2 tide with and without the presence of a tidal barrier in the Upper Bay of Fundy. Tidal amplitudes in the presence of a barrier increased 30 to50 cm in the case of both models, corroborating well the results of previous studies by Greenberg (1979). The three-dimensional model with the presence of a tidal barrier uniformly produced water levels of 3.5 cm (or 7%) less than the two-dimensional model.

Falconer et al. (2009) used a two-dimensional to assess the potential hydro-environmental impacts and power outputs of a barrage placed across the Severn River Estuary. The results showed that the Severn Barrage has the potential to reduce the tidal currents in a highly dynamic estuary. The maximum water levels were predicted to decrease by up to 0.5 m downstream of the barrage. In the region upstream of the barrage, the maximum water levels were predicted to decrease by 0.5−2.0 m due to the construction of the barrage. Falconer et al. (2009) estimated a reduction of suspended sediment loads (particularly upstream of the barrage), an increase of light penetration within the water column and, hence, an increase in the benthic bio-diversity and the level of aquatic life in the estuary. The results also show that the barrage will reduce markedly the risk of tidal flooding upstream of the barrage and to a lesser extent the one downstream of the structure.

Xia et al. (2010a, 2010b, 2010c) used a two-dimensional hydrodynamic model to assess the hydrodynamic impact of constructing tidal power projects in the Severn Estuary. The model was applied to predict the water levels and velocity distributions in the Severn Estuary, both with and without the proposed tidal power projects. Three projects were considered: the Cardiff–Weston Barrage, the Fleming Lagoon and the Shoots Barrage. The model-predicted hydrodynamic processes have been analysed in detail, both without and with the presence of the struc-

tures, including the discharge processes at key sections, the contours of maximum and minimum water levels, the envelope curves of high and low water levels, the maximum tidal currents, the local velocity fields around the structures and the mean power output curves. For the barrage scheme, Xia et al. estimated a 50% decrease in the peak discharges entering the upstream region and a reduction of maximum water levels upstream of the barrage by 0.3–1.2 m. As for the construction of the Fleming Lagoon, it was estimated to have little influence on the hydrodynamic processes in the Severn Estuary. Due to the construction of the Shoots Barrage, Xia et al. estimated a decrease in maximum water levels upstream by between 0.3 and 1.0 m.

In studies performed by Falconer et al. (2009) and by Xia et al. (2010a, 2010b, 2010c), they have provided different roughness coefficients for spring and neap tides to accurately calibrate their model to the observed (field) data.

Chapter 3

Design of Tidal Lagoons

3.1 Introduction

This chapter discusses the implementation of various tidal lagoon designs in the Upper Bay of Fundy in order to study their effects on the complex hydrodynamics in the Bay of Fundy and Gulf of Maine. The proposed types of tidal lagoons will be analyzed in the next chapter (Chapter 4) using a numerical model.

3.1.1 DMC tidal lagoon design

Delta Marine Consultants (DMC) (2007), commissioned by Tidal Electric Canada, conducted a conceptual design study for a tidal lagoon in the Minas Basin. DMC proposed constructing a tidal lagoon on the tidal flats along the northern shore of Minas Basin between Five Islands and Economy Point. Various plant layouts were investigated by DMC, including lagoons with single and multiple basins and lagoons with a direct and rectified flow through the power station. They concluded that a single basin with a direct flow through the power station would be most cost efficient for the Minas Basin site.

DMC developed conceptual designs for two lagoon types: coastal and offshore lagoon. The coastal lagoon comprised of a power station and a 24 km^2 impoundment formed between a 10.2 km long dike and the existing shoreline (Figure 2.5). The offshore lagoon comprised a power station and a 12 km^2 circular impoundment enclosed by a 11.9 km long dike detached from the shore. A rubble mound structure was recommended for the tidal containment dike since it is more cost efficient and more sustainable than monolithic structure (caisson or cofferdam). According to DMC, a 12 km^2 offshore lagoon fitted with fourteen 7.5 m diameter bulb turbine generators (up to 20 MW each) and 15 sluice gates (56 m^2 area each) would have an average power output of approximately 124 MW. The larger coastal lagoon, equipped with twenty-four 20 MW bulb turbines and 15 sluices, is estimated to have an average power output of approximately 220 MW. For further details, please refer to the report prepared by Delta Marine Consultants (DMC) (2007).

3.1.2 Proposed design of the tidal lagoon

In this study, the tidal lagoon design was based on the study performed by Delta Marine Consultants (DMC) (2007). Since DMC only studied two tidal lagoons on the tidal flats along the northern shore of Minas Basin between Five Islands and Economy Point, other potential site in the Upper Bay of Fundy were studied based on tidal lagoon capacity and efficiency. Tidal lagoon capacity and efficiency was based on basin design and power plant design, respectively. Each design has different components as shown in the schematic figure, Figure 3.1, for which each component design are found in a section as indicated in the figure.

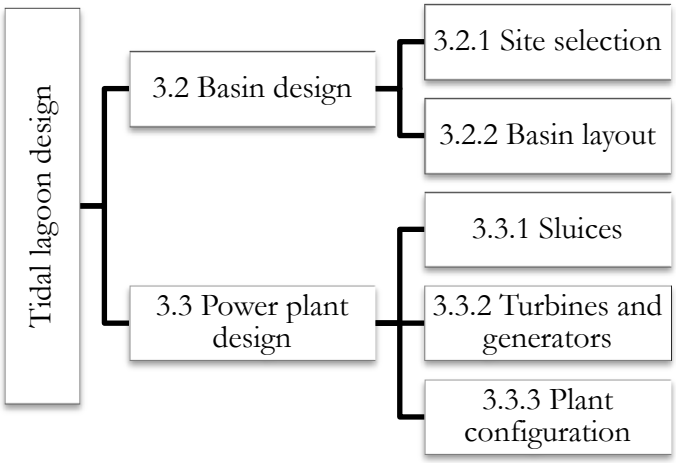

Figure 3.1: Diagram of tidal lagoon design.

3.2 Basin Design

3.2.1 Site selection

Elevation and tidal range data were used to determine potential sites for tidal lagoons. Elevation data came from three sources: (1) Geobase Canadian Digital Elevation Data, (2) CHS Multibeam Bathymetry, and (3) CHS Nautical Charts. The first dataset was used to define the elevations on tidal mudflats. Sources (2) and (3) covered the rest of the Bay of Fundy. The three datasets were originally referenced to different tidal datum and were therefore adjusted to the Universal Transverse Mercator North American Datum (NAD) 83 (Zone 19) coordinates in horizontal plane and referenced to the North American Vertical Datum of 1988 (NAVD 88) in vertical plane. The tidal range was calculated from the highest astronomical tide (HAT) and the lowest astronomical tide (LAT), derived from the harmonic constituents obtained by Dupont et al.

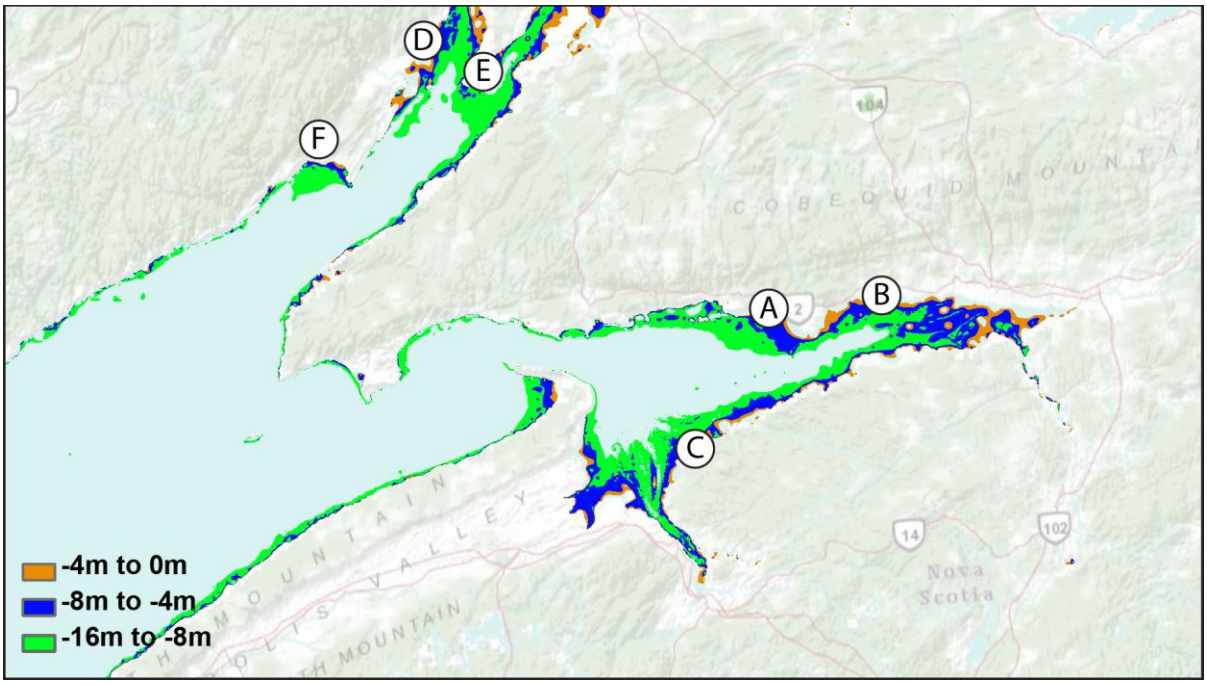

Figure 3.2: Potential site selection.

(2005). For further information on bathymetric and topographic data, and tidal range, please refer to Annexe A.

Elevation between -16.0 and 0.0 m was assumed to be a suitable location for implementing a tidal lagoon. Figure 3.2 shows different elevation ranges in the Upper Bay of Fundy. The site recommend by DMC (Site A) and five other sites, as indicated in the figure, were considered in this study:

Site A: This site is along the northern shore of Minas Basin between Five Islands and Economy Point. Site A was the only site recommended by DMC.

Site B: Site B is also along the northern shore of Minas Basin but further to the east from Site A beside upper Economy.

Site C: This site is along the southern shore of Minas Basin near Cambridge.

Site D: This site is along the western shore of Chignecto Bay near Mountville.

Site E: Site E is on the eastern shore of Chignecto Bay near Ragged Reef.

Site F: Site F is on the south-western shore of Chignecto Bay between Alma and Cape Enrage.

3.2.2 Tidal lagoon layout

As investigated by DMC, a single basin with a direct flow through the power station would be the most cost efficient for the Minas Basin site. Single basin was also assumed to be the most cost efficient in the Chignecto Bay.

As shown in Figure 3.3 and Figure 3.4, 16 other basin layouts were proposed based on the six sites. Each site has at least one coastal lagoon and one offshore. A sensitivity analysis with respect to the hydrodynamic impacts and the size of lagoon will be further performed for Site A. Site A has 3 different coastal lagoon layouts and 3 different offshore lagoon layouts including the two tidal lagoons designed by DMC.

3.3 Power Plant Design

3.3.1 Sluices

Sluices are considered in order to maximise the capacity of the tidal power plant. As proposed by DMC, sluices with cross-sectional area of 56m^2 were considered in this study.

To simulate adequately the hydrodynamic processes caused by the sluices, Falconer et al. (2009) and Xia et al. (2010a, 2010b, 2010c) applied the orifice equation to approximate the water head-discharge relationship. The orifice equation, Equation (2.1), is a simple equation, quick to implement, and computationally efficient. Although this type of equation provides rapid results, they must be treated with caution. The extent to which the results will differ from the realistic results depends largely on the dimensions and the position of the sluices. If sluices are positioned well below the water level, they will most likely behave like an orifice. Otherwise, they will behave like a culvert. The hydrodynamic processes of culverts are given through Equation (2.2) to Equation (2.5). These relationships are more complex and consequently take more time to compute.

The orifice equation is only applicable if the sluices are positioned well below water surface and behaves like an orifice. Figure 3.5 illustrates the highest invert elevation of a sluice that behaves similar to an orifice. The invert elevation is positioned at -20 m below the mean sea level. The figure shows the upstream water head-discharge relationship with a downstream water head of -8 m and 0 m. The dotted lines represent the orifice equation and the solid lines represent the culvert equations. During this process, the sluice was assumed to have a circular cross-sectional area of 56m^2 where tidal range fluctuated 16 m. A discharge coefficient of 0.75 was applied for

the orifice equation. Further details on the application of these formulas are provided Appendix C.1.

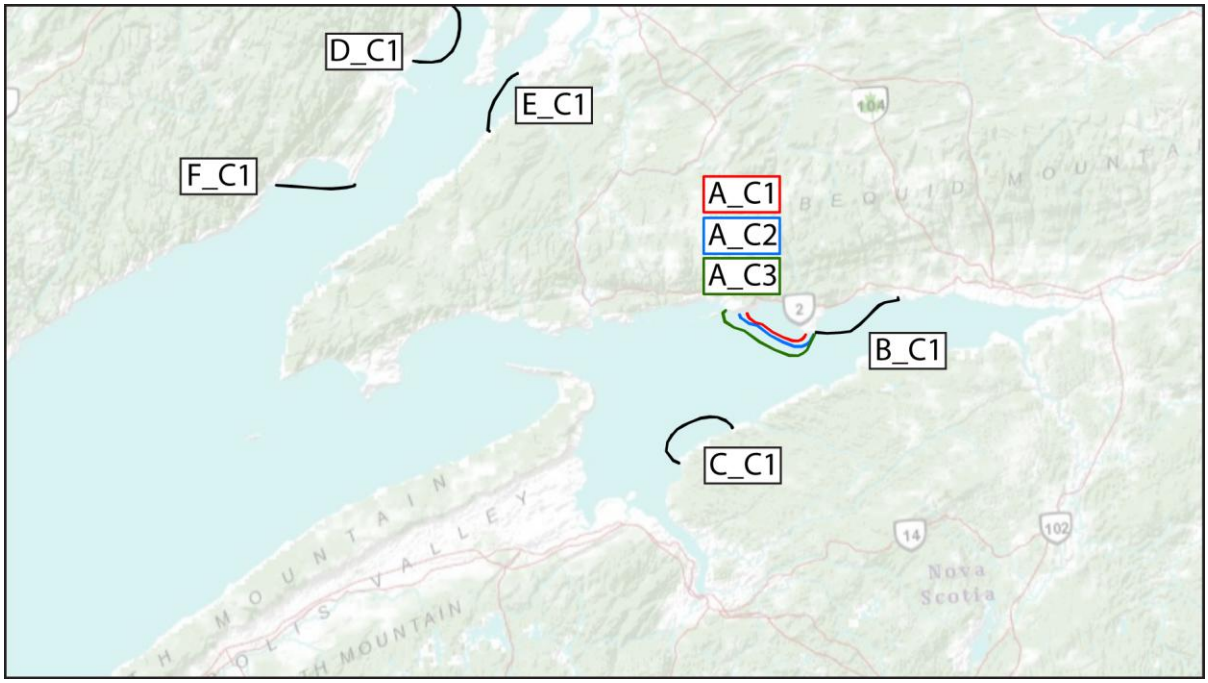

Figure 3.3: Coastal basin layouts place in the Upper Bay of Fundy.

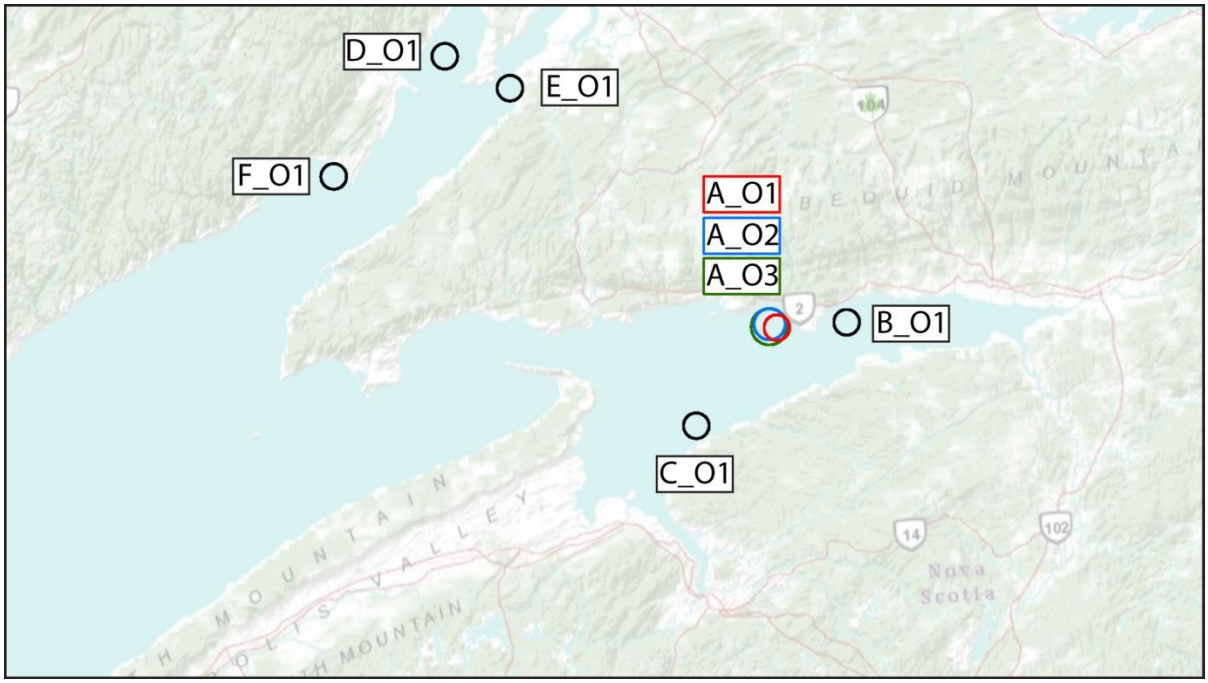

Figure 3.4: Offshore basin layouts place in the Upper Bay of Fundy.

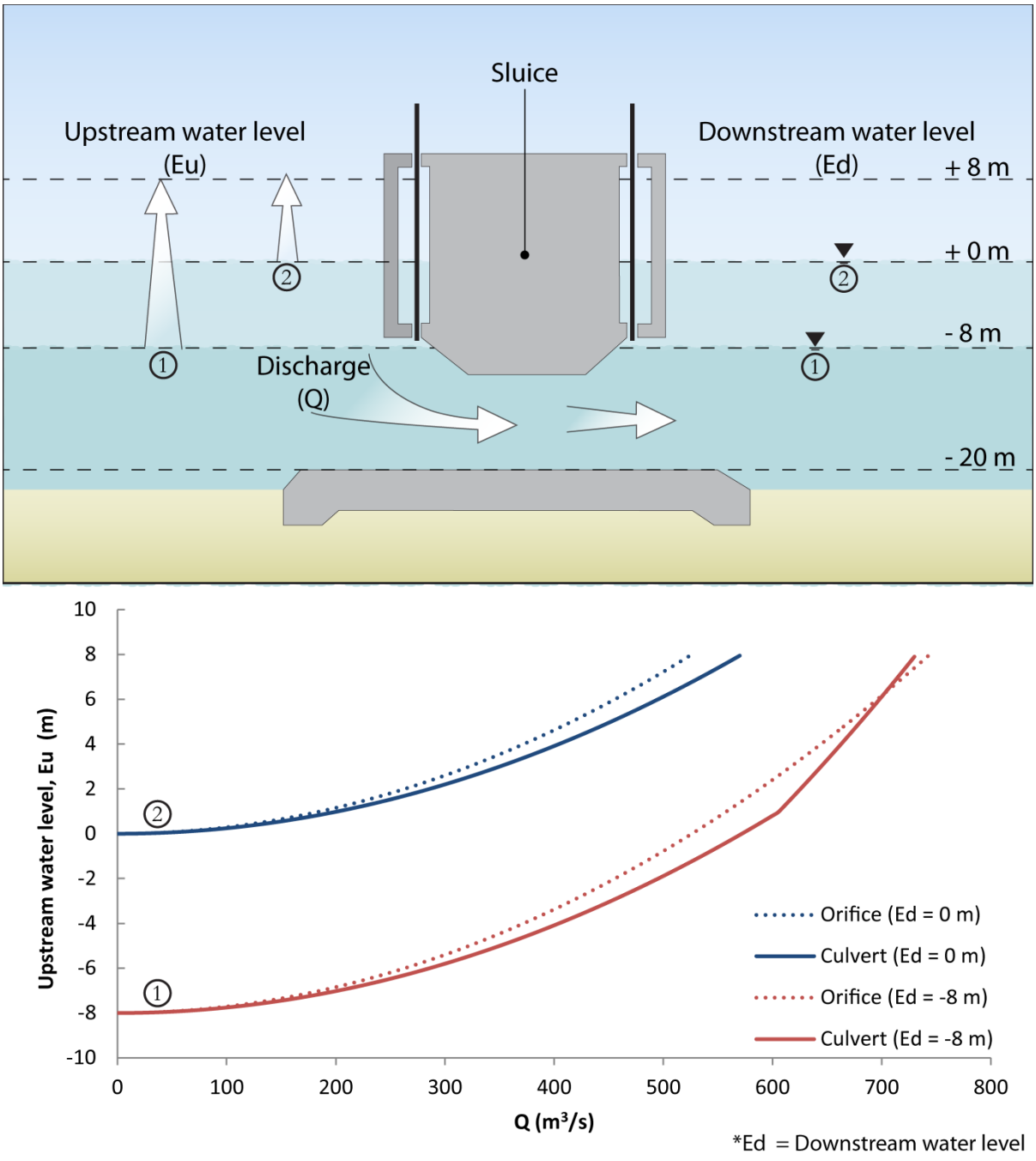

Figure 3.5: Flow-stage for a sluice for an invert elevation of -20 m using the orifice equation and the culvert equations.

3.3.2 Turbines and generators

As proposed by DMC, bulb turbines with a diameter of 7.5 m and 20 MW generators are considered in this study. It was assumed that turbines can operate in the a two-way mode described in Section 2.4.7.

The performance of a turbine is often defined as a hill chart, relating specific discharge, unit speed and efficiency. These are based largely on physical and computational fluid dynamics models. Turbines and generators for tidal power schemes are a commercially sensitive subject where manufacturers are reluctant to disseminate their design. The designer of a tidal power project has to approach manufacturers directly to assess the most appropriate design for the particular circumstances of tidal range, water depth and available volumes of water that apply to that site. The performance of turbines will be based on Figure 2.9 provided by Baker (1991). The turbine performance chart was developed based upon a maximum power output of the generator of 20 MW, a minimum operating head of 2.0 m, and suitable for a normal operating head of 6.0 m.

In this study, efficiencies of 90% on direct flow direction (ebb tide) and 80% on the reverse flow direction (flood tide) were assumed. Figure 3.6 shows the turbine performance chart. As shown in the figure, the power increases with water head up to a maximum value of 6.0 m. The power remains constant after the maximum head of 20 MW. The flow discharge through the turbine also reaches its maximum value when the water head is around 6.0 m and then decreases for higher water head. Table 3.1 summarises the theoretical turbine performance relationships.

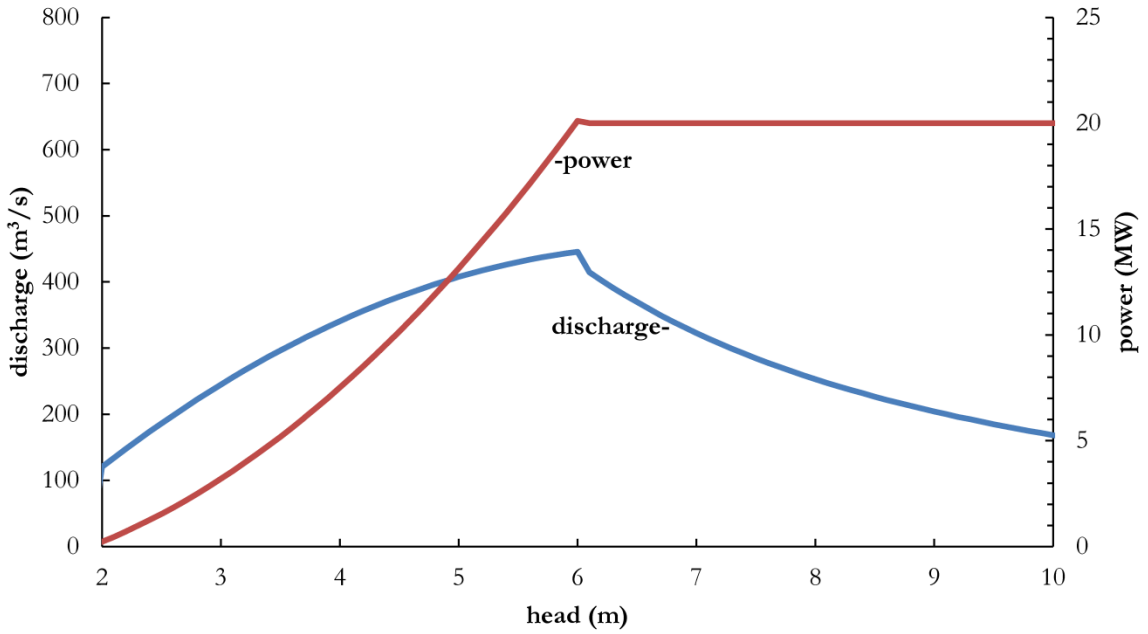

Figure 3.6: Theoretical turbine performance chart.

Table 3.1: Theoretical turbine performance relationships.

Output (1)	Relationship (2)	Flow conditions (3)
Power (MW)	$P = 0$	$H < H_{min}$
	$P = 0.6638 \cdot H^2 - 0.3376 \cdot H - 1.7601$	$H_{min} \leq H \leq H_{normal}$
	$P = 20$	$H > H_{normal}$
Discharge (m³/s)	$Q = 0$	$H < H_{min}$
	$Q = -14.45 \cdot H^2 + 196.94 \cdot H - 215.81$	$H_{min} \leq H \leq H_{normal}$
	$Q = 11185 \cdot H^{-1.822}$	$H > H_{normal}$

Notes: H_{min}: Minimum operating head(= 2 m); H_{normal}: Normal operating head(= 6 m).

3.3.3 Plant configuration

A box type model approach was applied to optimize the number of turbines and sluices to generate maximum power. The model is based on the assumptions that a volume of water allowed into the basin will raise the level of the basin by an amount equal to the volume allowed in, divided by the area of the basin at the time, i.e. spread uniformly over the basin. Thus the basin is defined by a simple depth/area curve. Depth/area curves for all the sites are shown in Appendix C.3.1.

The sluice water-head relationship and turbine performance chart are included in the model as described in Section 3.3.1 and Section 3.3.2, respectively. The model provides a good realistic

description of water level variations inside the basin, head differences, time varying discharge of turbines and sluices, and resulting energy generation. Flow processes inside the basin and leakage through the closure dam are neglected in the model and they will be investigated at a later stage.

The model was applied for the assessment of the effect of the turbine configuration on plant capacity and for the effect of sluice capacity on plant efficiency. For each of the 16 tidal lagoon layout, the model was applied to optimize the number of turbines and sluices for two-way generation, ebb generation and flood generation. The model applied constant wave amplitude of 6 m for one tidal cycle.

Figure 3.7 is an example of the resulting power output with different number of turbines and sluices for tidal lagoon layout *B_C1*. For a relatively small number of turbines (1-10 turbines), the capacity of the tidal power plant is increasing rapidly with an increasing number of turbines. For a larger number of turbines (20-25 turbines), the capacity of the tidal power plant is stabilising. The maximum capacity is reached at 29 turbines for 31 sluices. Additional turbines will result in a lower plant capacity.

The capacity of the tidal power plant is increasing steadily with an increase in the number of gates. However, the efficiency of an individual sluice (i.e. the increase in power generation for each additional gate) is decreasing, when the total number of gates is increasing.

Figure 3.7 also shows that an infinite number of sluices would produce the highest power generation since the filling and releasing stage would be negligible. Since it is unrealistic to have an infinite number of sluices, 31 sluices (or 80% of the maximum power generation) were considered in this study.

Figure 3.8 illustrates the two-way generation with sea level and basin level for tidal layout *B_C1*. Table 3.2 summarises the tidal lagoons characteristics with respect to area, dike length, and plant configuration.

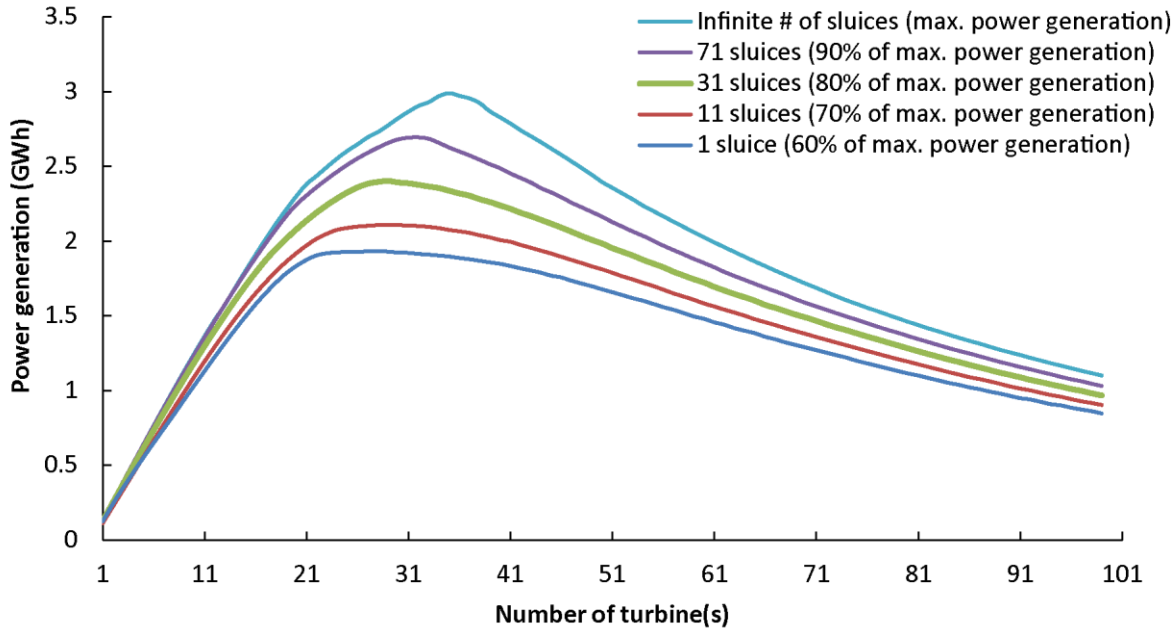

Figure 3.7: Optimization of turbines and sluices with power output for B_C1:two-way generation.

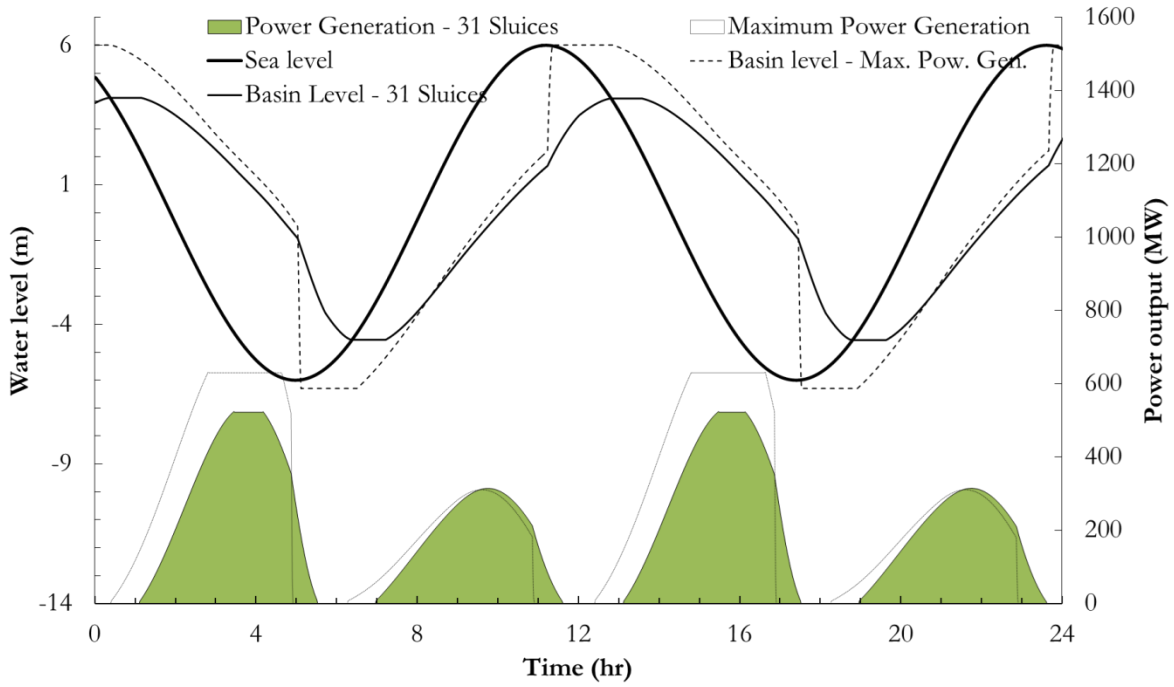

Figure 3.8: Two-way power generation for B_C1.

Table 3.2: Tidal lagoon characteristics.

Lagoon Scenario	Area (km^2)	Dike length (km)	Two-way generation		Ebb generation		Flood generation	
			Number of turbines	Number of sluices	Number of turbines	Number of sluices	Number of turbines	Number of sluices
A_C1[i]	26.66	10.92	24	15	20	26	16	17
A_O1[i]	12.01	12.44	14	15	10	12	10	12
A_C1	26.66	10.92	22	31	20	26	16	17
A_C2	35.10	13.92	30	41	26	34	22	25
A_C3	57.65	19.00	52	72	45	54	41	47
A_O1	12.01	12.44	12	23	10	12	10	12
A_O2	17.98	15.20	19	29	14	17	15	19
A_O3	23.99	17.52	23	39	20	23	20	25
B_C1	34.16	14.43	29	31	26	32	18	19
B_O1	12.01	12.44	12	22	10	12	10	12
C_C1	33.96	16.32	31	40	26	32	24	28
C_O1	12.01	12.44	12	24	10	12	10	13
D_C1	28.95	14.90	25	32	22	27	19	22
D_O1	12.01	12.44	12	23	10	12	10	12
E_C1	22.13	10.63	21	31	18	21	17	20
E_O1	12.00	12.44	12	23	10	12	10	12
F_C1	32.94	12.38	32	48	26	31	26	31
F_O1	12.01	12.44	12	23	10	12	10	12

[i] Recommended by Delta Marine Consultants (DMC) (2007)

Chapter 4

Hydrodynamic Analysis

4.1 Introduction

This chapter focuses on studying the hydrodynamics with and without the presences of tidal lagoons in the Bay of Fundy. As previously stated, the main goal of this thesis is to understand the hydrodynamics impacts of tidal lagoons in the Bay of Fundy and further away in the Gulf of Maine. Relationships between tidal lagoon characteristics and hydrodynamic impacts were studied to fulfill these objectives.

The hydrodynamic analysis is divided into several sections: model development, tidal lagoon hypothetical scenarios, model development with tidal lagoons, results, analysis of results, and relationships development. Figure 4.1 shows a schematic figure of the hydrodynamic analysis.

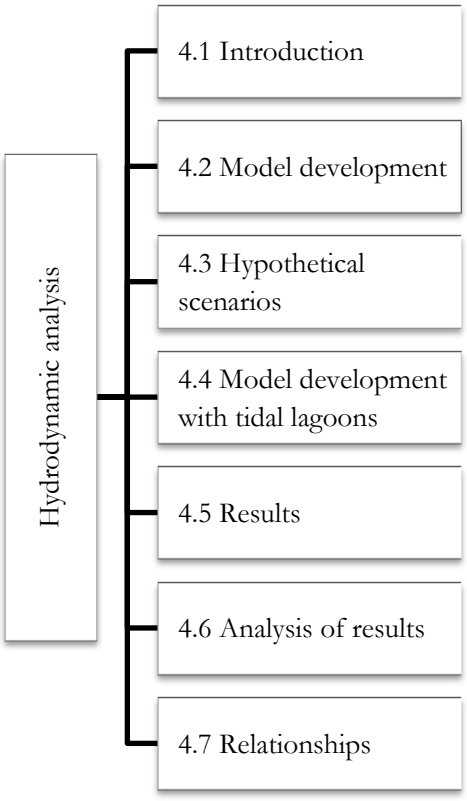

Figure 4.1: Schematic layout of Chapter 4.

4.2 Model Development

4.2.1 Description of the numerical model

In this study, tidal hydrodynamics in the BoF and GoM have been simulated using a numerical model based on the TELEMAC System, developed by *Electricité de France* as described by Hervouet (2007). The TELEMAC System is a suite of programs which are able to simulate the flow of water and the movement of water pollutants and sediments through lakes, rivers, canals, estuaries, and oceans. The propagation of waves (due to winds and tides) and their effects can also be simulated. TELEMAC uses an unstructured triangular mesh enabling complex shorelines and bathymetries to be represented in a highly realistic manner. Areas of particular interest can be modelled with very high resolution while regions of lesser interest can be represented with coarser resolution. TELEMAC can be applied to a wide range of phenomena, from small eddies behind bridge piers to pollutant transport in large coastal areas. TELEMAC has numerous applications in both river and maritime hydraulics including studies of hydrodynamics (i.e. river, estuaries and coastal waters), tidal circulation, failure of dams and dikes, pollutant dispersion, water quality planning, environmental impact of reclamations and dredging, dredged material disposal, port and harbour design, wave action including harbour resonance, and navigation and design of shipping channels.

TELEMAC-2D employs finite-element methods to solve the Saint-Venant equations over a computational domain, subject to initial as well as boundary conditions. The Saint-Venant equations can be written as

$$\frac{\partial h}{\partial t} + \vec{u} \cdot \vec{\nabla}(h) + h div(\vec{u}) = S_h \tag{4.1}$$

$$\frac{\partial u}{\partial t} + \vec{u} \cdot \vec{\nabla}(u) = -g\frac{dZ}{dx} + S_x + \frac{1}{h} div\left(h v_t \vec{\nabla} u\right) \tag{4.2}$$

$$\frac{\partial v}{\partial t} + \vec{u} \cdot \vec{\nabla}(v) = -g\frac{dZ}{dy} + S_y + \frac{1}{h} div\left(h v_t \vec{\nabla} v\right) \tag{4.3}$$

where h is the total water depth (m), x, y are horizontal space coordinates (m), u, v are depth-averaged velocities in x, y direction, respectively (m/s), g is the gravitational acceleration (m/s^2), v_t is the eddy viscosity (m^2/s), Z is the free surface water elevation (m), t is the time (s), and S_h, S_x, S_y are source terms (m/s^2). In this study, the effects of bed friction and Coriolis force are

included in the source terms. The effect of bed friction and the Coriolis force are explained in Section 4.2.1.1 and Section 0, respectively. The eddy viscosity was calculated using the Smagorinsky model (Smagorinsky , 1963) as described in Section 4.2.1.3. The wetting and drying of inter-tidal flats was also included in the modeling. Linear interpolation is used to calculate the free surface slope where there are semi-wet elements.

4.2.1.1 Strickler's equation

The bottom shear stress acting on a fluid is equivalent to

$$\vec{\tau} = -\mu \frac{d\vec{u}}{dh} \tag{4.4}$$

Based on the velocities in the vicinity of the bottom, the two-dimensional bottom shear stress is expressed by the following formula:

$$\vec{\tau} = -\frac{1}{2}\rho C_f \sqrt{u^2 + v^2}\vec{u} \tag{4.5}$$

where ρ is the water density (kg/m^3), C_f is the friction coefficient, and u, v are depth-averaged velocities in x, y direction, respectively (m/s). The C_f coefficient is rarely used and it is traditionally replaced by other coefficients among which the most common is the coefficient of Chézy denoted by C. C and C_f are linked by

$$C = \sqrt{\frac{2g}{C_f}} \tag{4.6}$$

where g is the gravitational acceleration (m/s^2). The friction at the bottom is equal to

$$\vec{F} = -\frac{1}{\rho h}\vec{\tau}\vec{n}, \quad \vec{F} = -\frac{1}{\cos\theta}\frac{g}{hC^2}\sqrt{u^2 + v^2}\vec{u} \tag{4.7}$$

where $\vec{n} = \sqrt{1 + (\partial Z/\partial dx)^2 + (\partial Z/\partial dy)^2} = 1/\cos\theta$ is the normal vector at the bottom which is the reciprocal of the cosine of the steepest slope on a given surface, and h is the water depth (m). The empirical law of Manning-Strickler defines the value of the coefficient of Chézy

$$C = KR^{1/6} \tag{4.8}$$

where K is the Strickler's coefficient (m$^{1/3}$/s), and R is the hydraulic radius (m). The Strickler's coefficient was adjusted spatially during the calibration of the model where it ranged between 20

and 40. For very wide channels when $R \approx h$, the equation, also known as Strickler's equation, can be simplified as

$$F_x = -\frac{1}{\cos\theta}\frac{g}{h^{4/3}K^2}\sqrt{u^2+v^2}u \tag{4.9}$$

$$F_y = -\frac{1}{\cos\theta}\frac{g}{h^{4/3}K^2}\sqrt{u^2+v^2}v \tag{4.10}$$

The equations above were added in the source terms, $S_x \; and \; S_y$, to the momentum equation.

4.2.1.2 The Coriolis force

The Coriolis effect is caused by the rotation of the Earth and the inertia of the mass experiencing the effect. Since the Earth completes only one rotation per day, the Coriolis force is quite small, and its effects generally become noticeable only for motions occurring over large distances and long periods of time, such as large-scale movement of air in the atmosphere or water circulation in the ocean. The rotation vector, velocity of movement, and the Coriolis acceleration expressed are

$$\Omega = \omega\begin{pmatrix}0\\ \cos\varphi\\ \sin\varphi\end{pmatrix}, v = \begin{pmatrix}v_e\\ v_n\\ v_u\end{pmatrix}$$

$$a_c = -2\Omega \times v = 2\omega\begin{pmatrix}v_n\sin\varphi - v_u\cos\varphi\\ -v_e\sin\varphi\\ v_e\cos\varphi\end{pmatrix}$$

where v_n is the northing velocity (m/s), v_e is the easting velocity (m/s), v_n is the upward velocity (m/s), and ω is the angular velocity of the earth, 7.27x10^{-5}(rad/s). To get a better visual understanding of each parameter, please refer to Figure 4.2.

When considering oceanic dynamics, the vertical velocity is small and the vertical component of the Coriolis acceleration is small compared to the gravity. For such cases, only the horizontal components are considered. Thus, the equations can be simplified as

$$v = \begin{pmatrix}v_e\\ v_n\end{pmatrix}, f = 2\omega\sin\varphi$$

$$a_c = \begin{pmatrix}v_n\\ -v_e\end{pmatrix}f \tag{4.11}$$

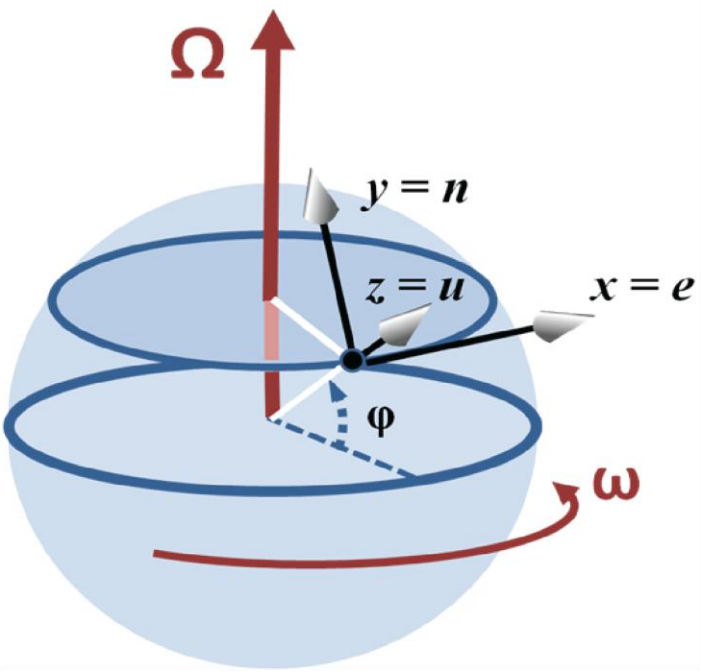

Figure 4.2: Coriolis effect(Courtesy of Brews Ohare).

The Coriolis force expressed below were added in the source terms, S_x *and* S_y, to the momentum equation.

$$F_x = f v_n = 2\omega \sin\varphi \, v \tag{4.12}$$

$$F_y = -f v_e = -2\omega \sin\varphi \, u \tag{4.13}$$

4.2.1.3 Smagorinsky model

The presence of a turbulence model is related to finding the average of the Navier-Stokes equations over time. This averaging introduces additional terms which form the Reynolds tensor, due to the energy transfers between the average movement and the eddies caused by the turbulence. Large eddy simulation (LES) with the Smagorinsky subgrid-scale model (SGS model) was used in this study:

$$\tau_{ij}{}^{Smag} - \frac{1}{3}\tau_{kk}\delta_{ij} = -2v_T\tilde{S}_{ij}, \quad v_T = (c_s\Delta)^2\left|\tilde{S}\right| \tag{4.14}$$

$\tilde{S}_{ij} = 0.5(\partial u/\partial y + \partial v/\partial x)$ is the strain rate tensor and $\left|\tilde{S}\right| = \sqrt{2\tilde{S}_{ij}\tilde{S}_{ij}}$ is its magnitude, Δ is the local grid size, and c_s is the Smagorinsky coefficient. Although c_s is not a universal constant,

$c_s$value of around 0.1 has been found to yield the best results for a wide range of flows (Smagorinsky, 1963), and is the default value in TELEMAC.

4.2.1.4 Numerical model

Two numerical methods are common in hydrodynamic models: structured grid approaches (primarily finite difference algorithms) and unstructured grid approaches (including finite element and finite volume methods). The objective of the numerical method is to separate the domain into components through a discretization process that produces a model grid. Structured grid models tend to use quadrilateral grid cells that limit the grid's flexibility in resolving complex shorelines but which are characterized by straightforward and efficient algorithms. Unstructured grid models have much more flexibility in their grid resolution by employing variable triangular elements, but tend to be more time consuming to run and more sensitive to numerical errors.

A finite element method, based on a flexible unstructured triangular mesh was applied in this study, to provide a detailed representation of the complex and irregular land boundaries in the Bay of Fundy and the Gulf of Maine.

4.2.2 Model grid

The areas of interest include the Bay of Fundy and the entire Gulf of Maine since the hydrodynamic impacts of tidal lagoons may affect both of these regions. Accuracy and computational costs are directly related to the size of the grid. Because of the large domain, the model requires different grid sizes over different areas depending on its level of interest. Figure 4.3 shows the two level of impact, high and low, in the Bay of Fundy and Gulf of Maine, respectively. Finer grid resolution was develop in high level of impact while coarser grid resolution was develop in areas low level of impact. The model grid development is divided in three components: depth/elevation, shorelines and grid resolution.

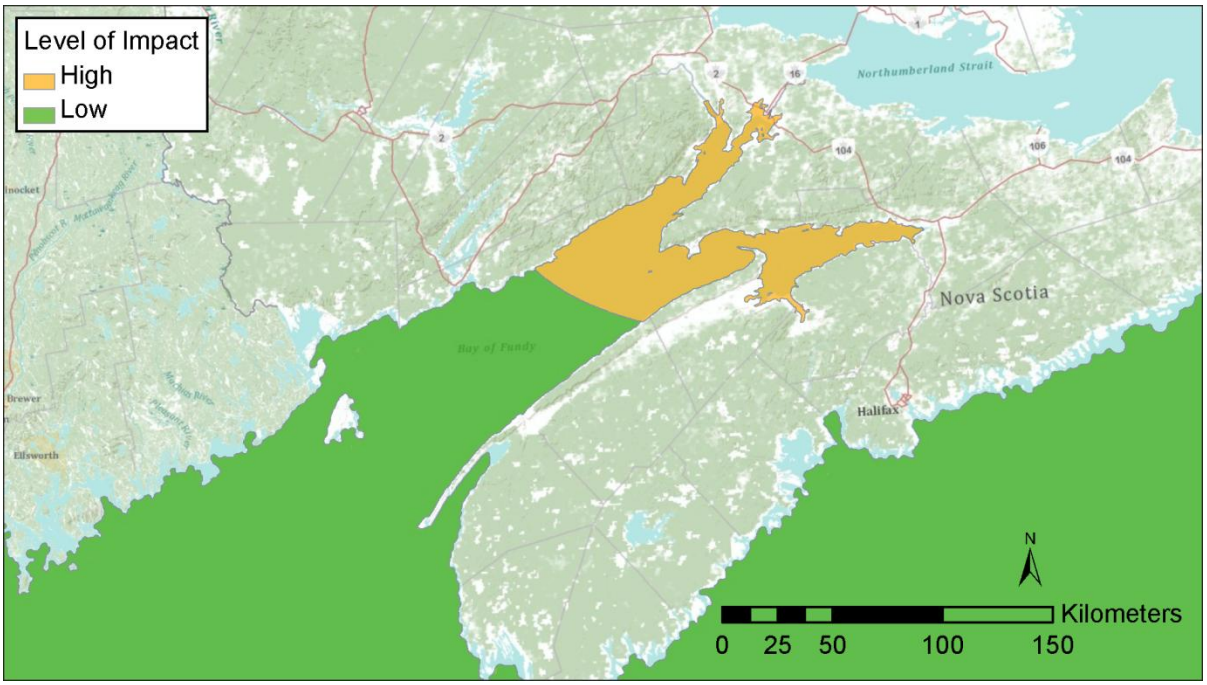

Figure 4.3: Level of impact in the BoF and GoM.

4.2.2.1 Depth / Elevation

The depth/elevation of each node was populated with topographic and bathymetric data from six sources: (1) Geobase Canadian Digital Elevation Data, (2) USGS National Elevation Dataset, (3) CHS Multibeam Bathymetry, (4) CHS Nautical Charts, (5) NOAA Soundings and Electronic Navigational Charts Bathymetry, and (6) BODC Gridded Bathymetric Chart of the Oceans. The first two datasets were used to define the elevations on tidal mudflats. Sources (3), (4) and (5) cover the GoM, the BoF and the Nova Scotian continental shelf. Deep ocean areas not covered by datasets (1) – (5) were populated with the BODC bathymetric dataset. The six datasets were originally referenced to different tidal datums and were adjusted to Universal Transverse Mercator North American Datum (NAD) 83 (Zone 19) coordinates in horizontal plane and referenced to North American Vertical Datum of 1988 (NAVD 88) in vertical plane. The procedure is described in Annexe A.

4.2.2.2 Model boundaries

The model grid was developed to have two types of boundaries: land boundaries and ocean boundaries. The land boundaries were developed to include inter-tidal flats up to the highest astronomical tide (HAT) shoreline in the higher level of interest (Upper Bay of Fundy). To reduce computational time during simulations, inter-tidal flats were excluded in areas of lesser interest (Lower Bay of Fundy and Gulf of Maine) by developing the boundary to the lowest astro-

nomical tide (LAT). The HAT and LAT were calculated from model results produced by a depth-integrated finite-element tidal circulation model performed by Dupont et al. (2005).

4.2.2.3 Computational grid resolution

Elements size in the model varies throughout the domain depending on various criteria. In areas judged as potentially high level of impact, elements have a grid resolution of 100 m (near the shoreline). In areas of lower level of interest, elements have a grid resolution of 1,000 m near the shoreline. A relatively fine grid resolution of 1,000 m was also generated along the continental shelf to accurately reflect the bathymetric variability. The size of grid elements was increase by a maximum factor of 1.1 from the shorelines to a maximum element size of 10,000 m.

4.2.2.4 Grid characteristics

The unstructured model grid developed for this study consists of 109,214 nodes and 205,601 triangular elements, varying in size from 100 m to 10 km. The computational domain spans an area of 235,289 km^2, extending from Providence, Rhode Island, to Halifax, Nova Scotia. The domain includes the Bay of Fundy and the entire Gulf of Maine (see Figure 4.4).

4.2.3 Boundary conditions

Land boundaries are considered to be solid boundaries where the flux of energy is set equal to zero. The ocean boundaries are considered to be open boundaries where the sea surface elevation is specified at each time step.

Many previous researchers, such as Greenberg (1979), Sucsy et al. (1992) and Karsten et al. (2008), considered only the M2 tidal constituent when studying the hydrodynamic impacts due to tidal power projects in the Bay of Fundy. While the M2 constituent is certainly the dominant one and contributes over 80% of the total tidal energy in the Upper Bay of Fundy as explained by Greenberg (1983), Lynch et al. (1993) and Zhang et al. (2003), in order to achieve better accuracy and refine the results, other constituents must be included in the model as well.

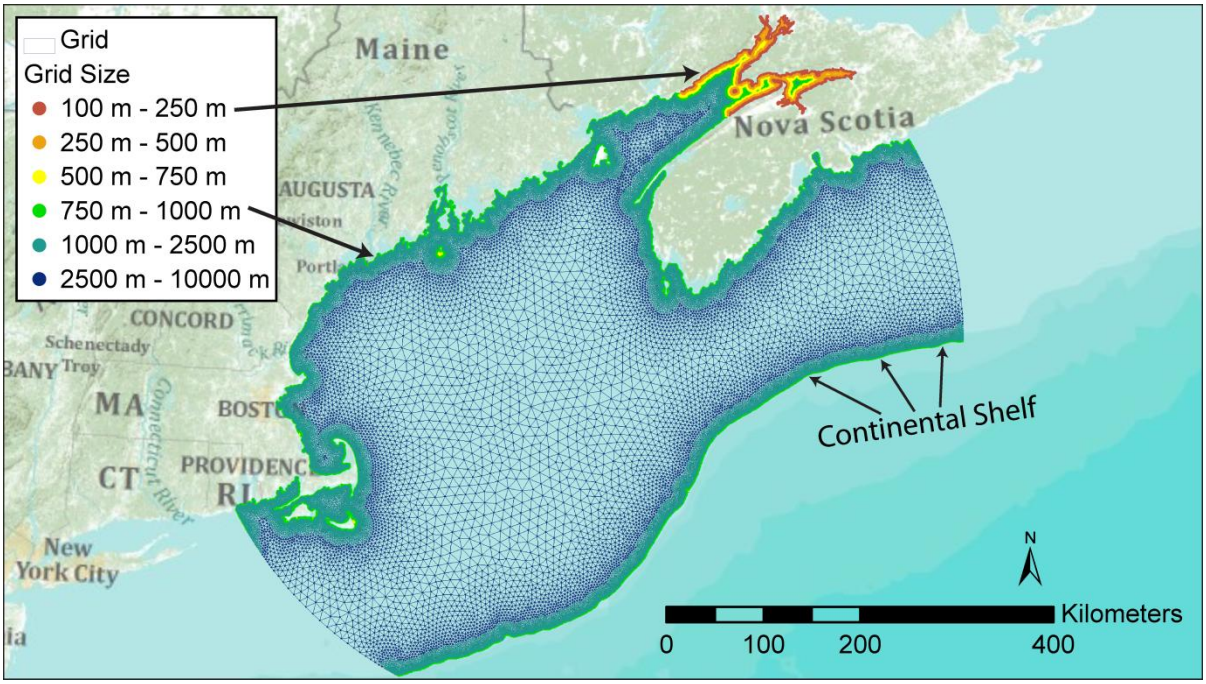

Figure 4.4: Computational domain of the Bof and GoM.

The tidal flows due to the M2 constituent and nine other leading constituents have been considered in the present study. Sea surface elevations and initial depth-averaged currents were interpolated along the open ocean boundary using harmonic constants for ten leading constituents (M2, N2, S2, K1, 01, K2, L2, 2N2, NU2, M4). The boundary conditions were calculated from model results produced by a depth-integrated finite-element tidal circulation model from Dupont et al. (2005). This 2D tidal model has a domain covering the Gulf of Maine, Bay of Fundy and part of the Scotian Shelf, and assimilates tidal constituents derived from sea level observations made by the TOPEX-Poseidon altimeter. According to Dupont et al.(2005) the 9 constituents, excluding M4, account for 88% of the sum of the amplitudes of the 67 official tidal constituents at Saint John. Freshwater inflows from rivers are insignificant relative to the tidal flows, and were therefore ignored in the present study.

4.2.4 Model Calibration and validation

The model was calibrated by adjusting the bottom roughness in different parts of the computational domain (see Figure 4.5) to minimize the error in tidal range and time-of-tide between the model's predictions and water level time histories recorded at 142 NOAA/DFO tidal stations distributed throughout the domain. For each tidal station, model results were compared to synthesized predictions from harmonic constants established by DFO and NOAA. The same set of

10 constituents (M2, N2, S2, K1, 01, K2, L2, 2N2, NU2, M4) used to drive the numerical model was also used to generate the target water level time histories for each tidal station.

The model was first calibrated for the M2 tidal constituent alone, and then for all 10 constituents combined together. A sensitivity analysis was conducted with respect to the model time step and its influence on the model numerical stability. It was finally concluded that a model time step of 10 seconds was sufficient to ensure the numerical stability.

Tides were simulated for 7-days periods during the calibration process. Once successfully calibrated, the model was validated by predicting the tides at various locations over a different 28-day period in order to capture two full spring-neap tidal cycles. Predicted depth-averaged current velocities from the model were also compared with available ADCP data (see Section 4.2.4.3). Three different time period, as shown in Table 4.1, were simulated during validation.

Table 4.1: Calibration and validation simulation period.

	Simulation without tidal lagoons	
Simulation period	Calibration	Validation
10/08/2007 00:00 - 17/08/2007 00:00	C1	
17/08/2007 00:00 - 14/09/2007 00:00		V1
07/01/2009 00:00 - 04/02/2009 00:00		V2
17/07/2009 00:00 - 15/08/2009 00:00		V3

4.2.4.1 Bottom roughness

The Strickler's roughness coefficient for different areas was adjusted with values ranging from 20 to 40 in order to minimize the calibration errors throughout the domain. Strickler's coefficient usually ranges from 20 to 40 for natural river beds and from 50 to 90 for a concrete-lined channel (Hervouet, 2007). The characteristics of the seabed were taken into consideration when selecting the bottom roughness coefficient for each area. Figure 4.5 shows the calibrated bottom roughness values throughout the domain.

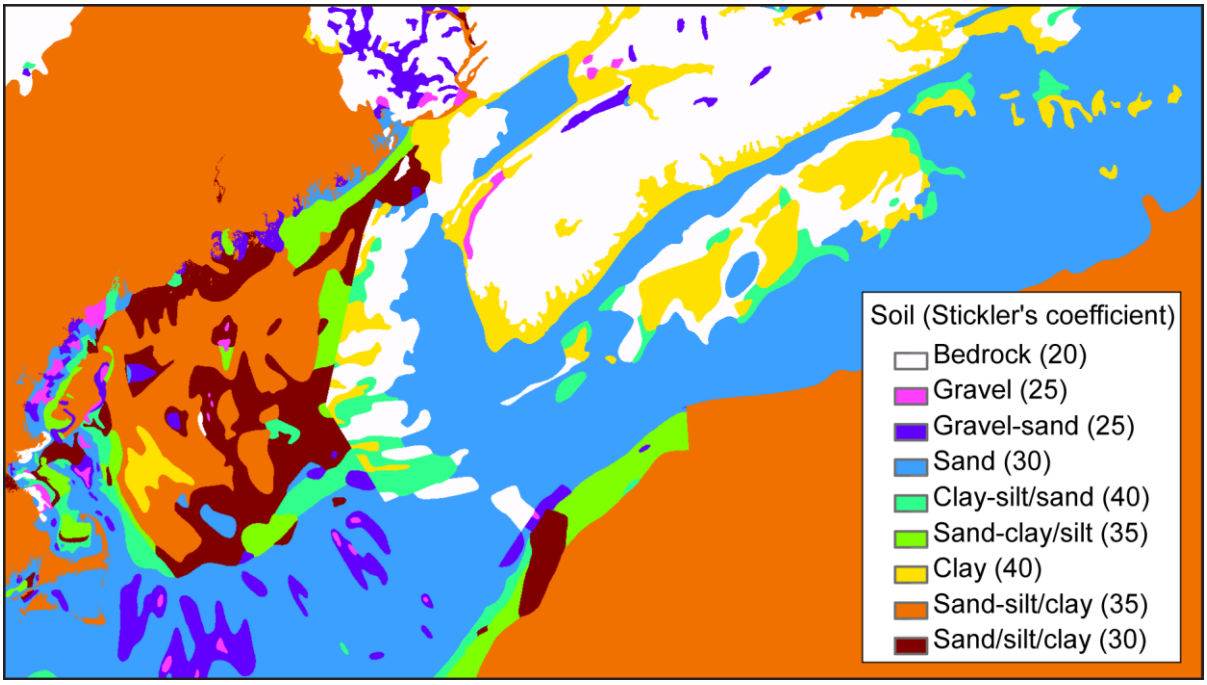

Figure 4.5: Strickler's coefficient for various regions in the computational domain.

4.2.4.2 Water level validation and error analysis

Figure 4.7 shows the water level fluctuation during the simulation of validation 3, V3, for two stations (Five Islands and Boston). Only the last 10-days of simulation are shown for clarity and brevity. It can be seen that the numerical model predictions agree very well with astronomical tide projection. Both the minimum and maximum water levels, as well as their phase, are accurately predicted.

Table 4.2 shows the RMS relative error and the RMS phase difference in minutes of high tides and low tides at selected stations for simulations V1, V2, and V3. The selected stations, as indicated in the table, are shown in Figure 4.7. They cover the Bay of Fundy and most of the Gulf of Maine. The relative error was calculated by:

$$e = \frac{\eta_m - \eta_o}{\eta_o} \tag{4.15}$$

where η_m is the computed water level while η_o is the observed one.

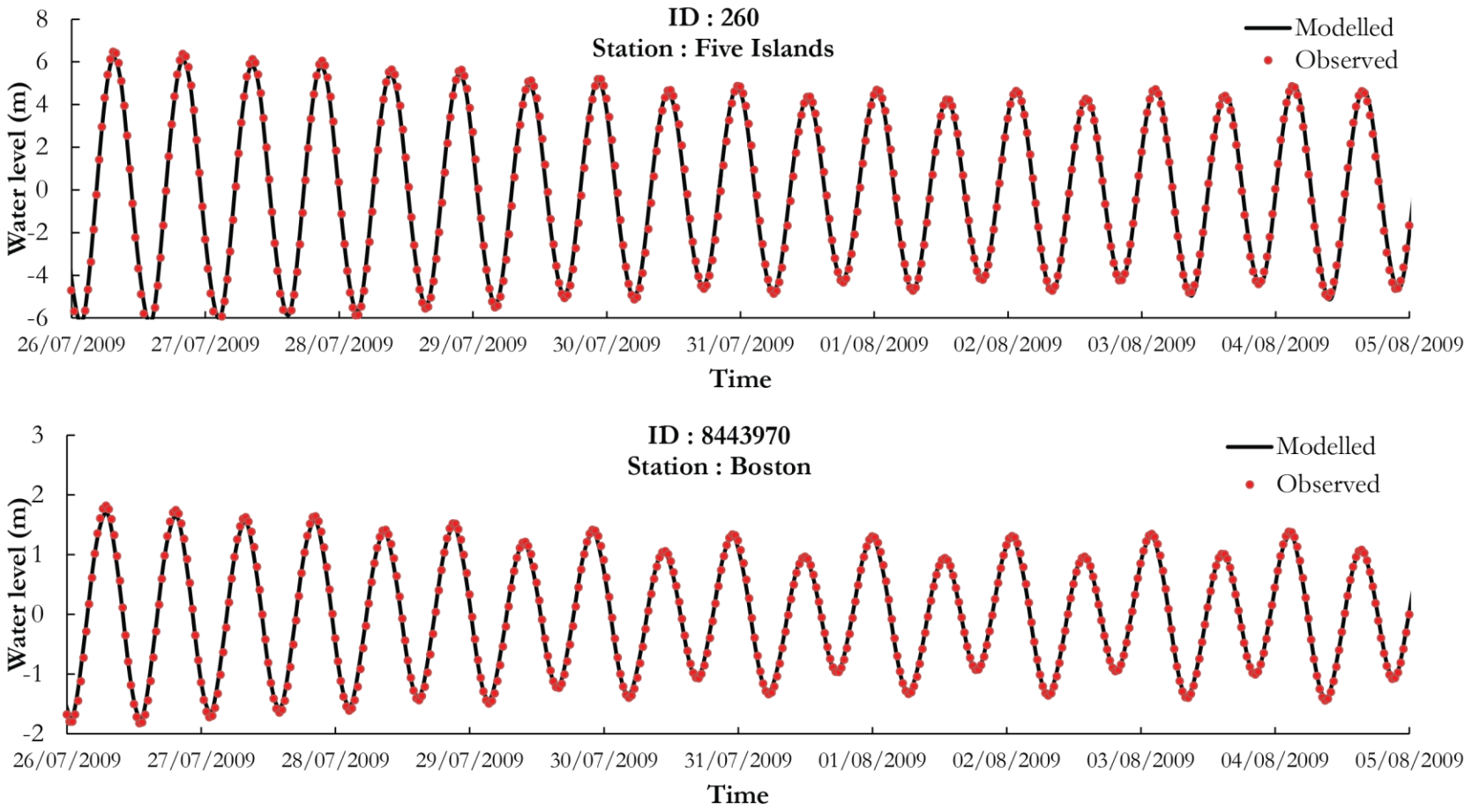

Figure 4.6: Modelled and observed water level data at two stations (Boston and Five Islands) during validation V3.

Table 4.2: Error analysis of the validation simulations.

		V1				V2				V3			
		High tide		Low tide		High tide		Low tide		High tide		Low tide	
ID	**Station**	RMS Relative error (%)	RMS Phase difference (min)	RMS Relative error (%)	RMS Phase difference (min)	RMS Relative error (%)	RMS Phase difference (min)	RMS Relative error (%)	RMS Phase difference (min)	RMS Relative error (%)	RMS Phase difference (min)	RMS Relative error (%)	RMS Phase difference (min)
5	SEAL COVE	4.42%	14	4.78%	13	4.69%	11	5.09%	16	4.85%	11	5.32%	13
14	SOUTH LUBEC	4.70%	13	4.94%	14	4.03%	15	5.21%	6	3.99%	14	5.17%	12
42	BLACKS HARBOUR	3.51%	16	2.89%	16	4.52%	15	4.07%	12	4.85%	16	4.37%	12
65	SAINT JOHN	6.15%	15	7.37%	14	7.71%	15	9.22%	11	7.07%	16	8.49%	13
140	HERRING COVE	10.20%	21	9.99%	24	6.43%	16	6.96%	18	6.71%	19	7.43%	19
240	CAPE D'OR	9.70%	16	6.12%	15	8.95%	15	3.41%	17	9.21%	15	3.50%	19
247	DILIGENT RIVER	7.46%	21	6.02%	20	7.76%	19	7.10%	11	7.16%	18	6.53%	13
260	FIVE ISLANDS	6.67%	19	6.07%	19	8.18%	16	7.49%	16	7.45%	15	6.82%	15
270	BURNTCOAT HEAD	7.26%	23	8.13%	30	7.57%	21	7.28%	29	6.83%	23	6.41%	32
282	HANTSPORT	6.99%	18	6.84%	27	7.36%	22	6.23%	22	7.69%	24	6.57%	24
325	DIGBY	9.67%	15	9.88%	14	9.53%	11	9.85%	11	9.91%	13	10.11%	14
365	YARMOUTH	7.32%	18	6.90%	13	4.21%	18	4.19%	13	3.40%	16	3.30%	12
425	SHELBURNE	4.45%	11	5.03%	18	4.82%	11	5.14%	19	4.70%	10	5.09%	15
490	HALIFAX	7.85%	17	6.78%	19	7.39%	21	7.36%	20	6.92%	20	7.66%	19
40139	CHIGNECTO (RAY .4)	7.02%	15	6.43%	17	6.85%	20	6.19%	21	6.76%	20	6.20%	22
8410140	EASTPORT	10.23%	16	10.24%	14	10.48%	12	10.98%	10	10.71%	14	10.97%	13
8413320	BARHARBOR	5.31%	13	6.23%	11	5.00%	11	6.38%	10	5.13%	13	6.55%	11
8418150	PORTLAND	3.72%	11	2.93%	18	2.40%	8	2.42%	18	2.71%	11	2.58%	18
8441551	ROCKPORTHARBOR	6.66%	14	4.53%	13	5.90%	7	4.42%	14	6.00%	13	4.45%	15
8443970	BOSTON	4.08%	14	3.80%	11	3.41%	11	3.70%	9	3.61%	9	3.72%	8

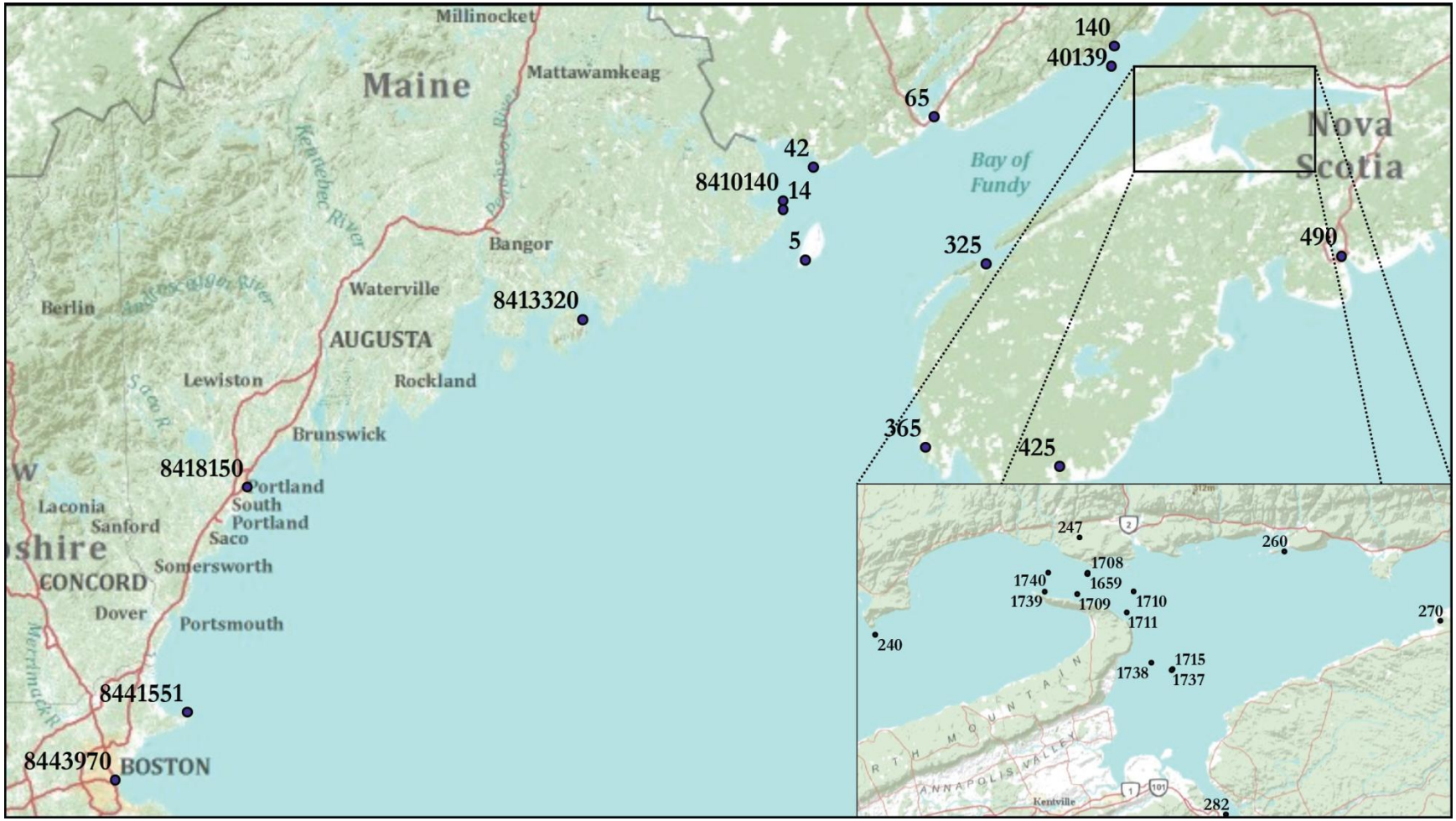

Figure 4.7: Observed and measured water level and velocity stations (ID).

4.2.4.3 Tidal currents velocity comparison

Although the velocity from tidal currents can also be predicted from synthesized harmonic constants, it was not considered in this study. The records of current velocities in the Bay of Fundy are not sufficient to perform a harmonic analysis and obtain velocity harmonic constituents. Instead, velocities from simulations were compared directly with Acoustic Doppler Current Profiler (ADCP) measurements which were obtained by DFO. These ADCP measurements were collected at a fixed point and only captured spatial averages of velocity in individual "bins" throughout a vertical column of water. Table 4.3 shows different values of velocity data collected at different locations and at different time periods. The locations of the ACDP collection data are shown in Figure 4.7.

Table 4.3: Current velocity measurements.

ID	Longitude	Latitude	Start	End
1658	-64.40383	45.35648	17/08/2007 19:15	28/08/2007 14:30
1659	-64.40335	45.35615	28/08/2007 16:30	14/09/2007 16:45
1708	-64.40330	45.35760	07/01/2009 14:43	07/02/2009 15:00
1709	-64.42103	45.33210	07/01/2009 15:19	20/02/2009 00:00
1710	-64.32438	45.33525	07/01/2009 14:16	12/02/2009 06:46
1711	-64.33605	45.31007	07/01/2009 13:52	15/02/2009 14:14
1715	-64.25802	45.24182	28/01/2009 14:35	18/02/2009 10:14
1737	-64.25968	45.24060	17/07/2009 11:57	27/08/2009 10:50
1738	-64.29440	45.24967	17/07/2009 12:12	27/08/2009 11:19
1739	-64.47642	45.33508	17/07/2009 13:22	23/08/2009 13:00
1740	-64.47026	45.35777	17/07/2009 13:48	14/08/2009 13:49

Since the hydrodynamic numerical model is two-dimensional vertical (2DV), only depth-averaged velocities can be obtained. In order to compare the modelled results with the ADCP velocity measurements, the latter were transformed into depth-averaged velocities. The transformation is divided in two steps. The first step is to calculate the unit discharge, q, of each bin as:

$$q = \sum_{i=0}^{n} V_i \cdot H_i \tag{4.16}$$

where V_i is the averaged-velocity of the bin and H_i is the depth of bin. It was assumed that the velocity at the water surface was 0.8 smaller than the closest velocity near the water surface captured by the ADCP. In addition, the velocity near the bed was assumed to be null (non-slip condition). The second step was to determine the depth-averaged velocity, $\bar{V}$, as

$$\bar{V} = \frac{q}{D} \tag{4.17}$$

where $\bar{V}$ is the depth-averaged velocity, and D is the water depth. Figure 4.8 shows an example of depth-averaged velocities in x and y directions for station 1737. Although the model overestimates the velocities, the results are comparable. Besides instrumental measuring errors from the ADCPs and the method of converting velocity profile to depth-averaged velocity, the numerical model does not include important factors such as the influence of wind waves, turbulence, and storm surge that may influence on tidal currents.

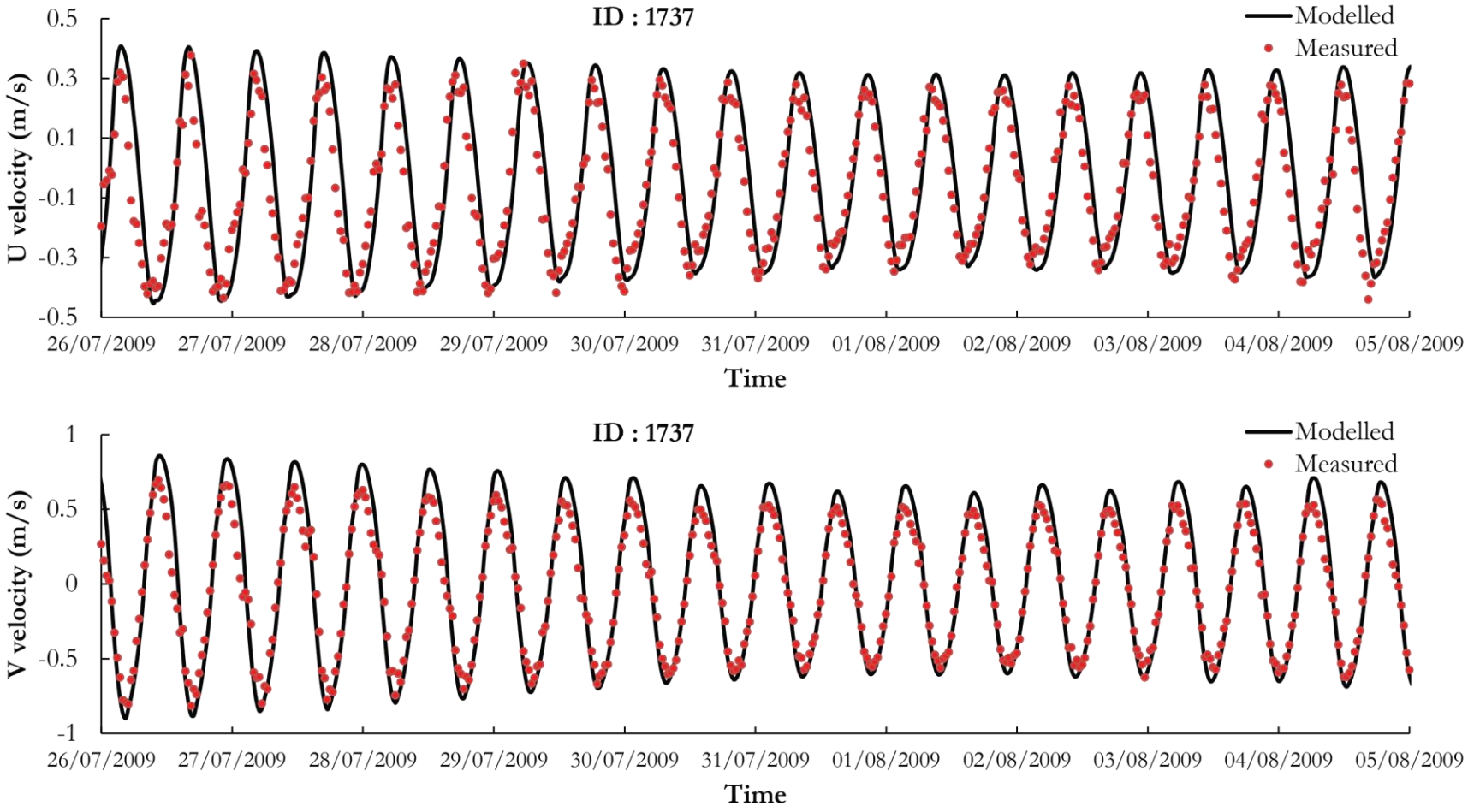

Figure 4.8: Modelled and measured depth-averaged velocities at station 1737 during V3.

4.3 Hypothetical Tidal Lagoons Scenarios

A number of different hypothetical scenarios with one or more tidal lagoons located in Minas Basin and/or in the Chignecto Bay have been considered to study the hydrodynamic effects of tidal lagoons throughout the Bay of Fundy and Gulf of Maine. As such, the relationship between the scale of lagoon development and the scale of potential impact could be ascertained.

The hypothetical scenarios are divided into two categories: (1) single tidal lagoon, and (2) multiple tidal lagoons.

4.3.1 Single tidal lagoon

A single tidal lagoon scenario consists of implementing one tidal lagoon in the Minas Basin. Four group scenarios were considered to assess different relationships. They are based on:

A. Coastal and offshore tidal lagoon design by DMC

B. Operation mode

C. Lagoon size

D. Lagoon location

Each group scenario is described below.

4.3.1.1 Coastal and offshore tidal lagoon design by DMC

For this group scenario, two simulations are considered and they are based on the coastal and offshore lagoons proposed by DMC, as explained in Section 3.1.1. Lagoon layout A_C1[i] with 24 turbines and 15 sluices, as defined in Table 3.2, was selected for the coastal design simulation. As for the offshore design simulation, lagoon layout A_O1[i] with 14 turbines and 15 sluices was selected. The power operating mode - the two-way generation - was selected for each simulation. The scenarios characteristics are summarized in Table 4.4.

Table 4.4: DMC's coastal and offshore lagoons simulation scenarios.

Simulation	Lagoon layout	Impoundment area (m^2)	Operating mode	Number of turbine(s) [-]	Number of sluice(s) [-]
S1	A_C1[i]	26.66	Two-way	24	15
S2	A_O1[i]	12.01	Two-way	14	15

[i] Recommended by Delta Marine Consultants (DMC) (2007)

4.3.1.2 Operating mode

Xia et al. (2010b) concluded that different operating modes have different hydrodynamic impacts and power outputs, as explained in Section 2.4.8. For this reason, a simulation for two-way generation, ebb generation, flood generation, as well as non-power operating mode such as opened-gates, and closed-gates was considered in this study. Each power operating mode is explained in Section 2.4.7. In this study, the opened-gates mode is when sluices gates are opened and turbines gates are closed throughout the entire simulation. As for the closed-gates mode, the gates for turbines and sluices are always closed.

Lagoon layout A_C1 with 22 turbines and 31 sluices, as defined in Table 3.2, was selected for all the simulations. The scenarios are summarized in Table 4.5.

Table 4.5: Operating mode simulation scenarios.

Simulation	Lagoon layout	Impoundment area (m^2)	Operating mode	Number of turbine(s) [-]	Number of sluice(s) [-]
S3	A_C1	26.66	Two-way	22	31
S4	A_C1	26.66	Ebb	20	26
S5	A_C1	26.66	Flood	16	17
S6	A_C1	26.66	Gates-opened	-	-
S7	A_C1	26.66	Gates-closed	-	-

4.3.1.3 Lagoon size

The simulations in this group are to assess the relationship between the scale of lagoon development and the scale of potential impact for both types of tidal lagoon: coastal and offshore. Lagoon layout A_C1, A_C2, and A_C3 were selected for the coastal lagoon simulations and A_O1, A_O2, and A_O3 was selection for the offshore lagoon simulations. The scenarios are summarized in Table 4.6.

Table 4.6: Lagoon size scenarios.

Simulation	Lagoon layout	Impoundment area (m^2)	Operating mode	Number of turbine(s) [-]	Number of sluice(s) [-]
S3[i]	*A_C1*	*26.66*	*Two-way*	*22*	*31*
S8	A_C2	35.10	Two-way	30	41
S9	A_C3	57.65	Two-way	52	72
S10	A_O1	12.01	Two-way	12	23
S11	A_O2	17.98	Two-way	19	29
S12	A_O3	23.99	Two-way	23	39

[i] Simulated in Section 4.3.1.2.

4.3.1.4 Lagoon location

In this section, the relationship between the lagoon's location within the Minas Basin and the scale of potential impact of a coastal tidal lagoon were studied. Lagoon layout A_C1, B_C1, and C_C1 were selected for the coastal lagoon simulations. The scenarios are summarized in Table 4.7.

Table 4.7: Lagoon location scenarios.

Simulation	Lagoon layout	Impoundment area (m^2)	Operating mode	Number of turbine(s) [-]	Number of sluice(s) [-]
S3[i]	*A_C1*	*26.66*	*Two-way*	*22*	*31*
S13	B_C1	34.16	Two-way	29	31
S14	C_C1	33.96	Two-way	31	40

[i] Simulated in Section 4.3.1.2.

4.3.2 Multiple tidal lagoons

Multiple tidal lagoons involved implementing two or more tidal lagoons in the Minas Basin and/or in Chignecto Bay. Three group scenarios were considered and they are based on the implementation of tidal lagoons in the following locations:

A. Minas Basin

B. Chignecto Bay

C. Chignecto Bay and Minas Basin

Each group scenario is described below.

4.3.2.1 Minas Basin

Two scenarios were considered in this group. The first consists of implementing three coastal tidal lagoons in Minas Basin, lagoon layout A_C1, B_C1, and C_C1. The second simulation consists of implementing three offshore tidal lagoons in Minas Basin, lagoon layout A_O1, B_O1, and C_O1. These scenarios are summarized in Table 4.8.

Table 4.8: Minas Basin scenarios.

Simulation	Lagoon layout	Impoundment area (m^2)	Operating mode	Number of turbine(s) [-]	Number of sluice(s) [-]
S15	A_C1, B_C1, and C_C1	94.78	Two-way	22, 29, and 31	31, 31, and 40
S16	A_O1, B_O1, and C_O1	36.03	Two-way	12, 12, and 12	23, 22, and 24

4.3.2.2 Chignecto Bay

Similar to the previous sections, one scenario with three coastal tidal lagoons in Chignecto Bay and one scenario with three offshore tidal lagoons in Chignecto Bay were proposed and modeled. The selected lagoon layouts for this scenario are summarized in Table 4.9.

Table 4.9: Chignecto scenarios.

Simulation	Lagoon layout	Area (m^2)	Operating mode	Number of turbine(s) [-]	Number of sluice(s) [-]
S17	D_C1, E_C1, and F_C1	84.02	Two-way	25, 21, and 32	32, 31, and 48
S18	F_O1, E_O1, and F_O1	36.03	Two-way	12, 12, and 12	23, 23, and 23

4.3.2.3 Chignecto Bay and Minas Basin

Finally, the last scenario considered three offshore tidal lagoon in Chignecto Bay and three offshore tidal lagoons in Minas Basin. The selected lagoons layout for this scenario is summarized in Table 4.10.

Table 4.10: Chignecto Bay and Minas Basin scenarios.

Simulation	Lagoon layout	Impoundment area (m^2)	Operating mode	Number of turbine(s) [-]	Number of sluice(s) [-]
S19	A_O1, B_O1, C_O1, F_O1, E_O1, and F_O1	72.06	Two-way	12, 12, 12, 12,12, and 12	23, 22, 24, 23, 23, and 23

4.4 Model Development with Tidal Lagoons

4.4.1 Model grid

In addition to the existing grid without tidal lagoons, 13 grids with tidal lagoons have been developed to represent hypothetical scenarios. The grid is only refined near the lagoon and remains unchanged elsewhere. The grid along the impoundment dike and the powerhouse has a resolution of 100 m. The dike and powerhouse are idealized in the model as vertical sided structures having a width 50 m. Figure 4.9 shows details of the model grid development for the model grid layout A_C1 and A_O1. A domain decomposition technique has been employed in order to simulate the lagoons and the flows through the turbines and sluices. This technique was employed by several authors such as Falconer et al. (2009) and Xia et al. (2010a, 2010b, 2010c). This approach involves subdividing the domain into non-overlapping sub-domains, each with its own unstructured mesh. This technique is widely recognized as an efficient and flexible way of simulating complex physical processes. As shown in Figure 4.9, the model domain was divided into two sub-domains representing the outer ocean and the inner tidal lagoon basin, respectively. A total of 13 different grids were created to accommodate all the hypothetical scenarios. For more information on model development with tidal lagoons, refer to Annexe A.

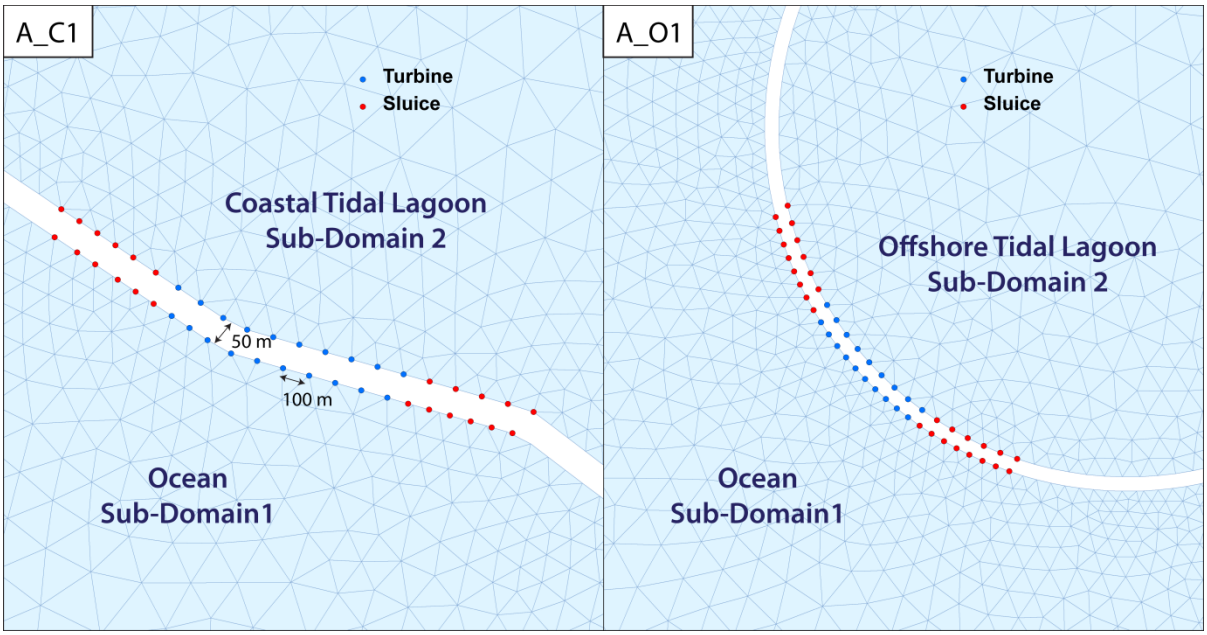

Figure 4.9: Model grid details.

4.4.2 Boundary conditions

The same boundary conditions, as explain in Section 4.2.3, were applied to the model except in the vicinity of the tidal lagoon. Multiple pairs of sources and sinks were defined to transfer mass between the two domains, simulating the flows through the sluices and turbines within the powerhouse. Open boundary conditions were specified at the sources and sinks, and were linked dynamically using a head-discharge relationship. The head-discharge relationship for the sluices and turbines are explained in Section 3.3.1 and Section 3.3.2, respectively.

For each lagoon layout, the powerhouse was assumed to have turbines located centrally between the sluices as shown in Figure 4.9. A similar powerhouse layout scheme was also employed by Xia et al. (2010c). The turbine zone was assumed to have a length of 1000m and sluice zone of 500m on each side. The powerhouse length was assumed to have 2,000 m for each hypothetical scenario.

Depending on the lagoon layout, the turbine zone engulfs 7 to 10 nodes and the sluice zones cover 9 to 13 nodes. To accommodate the number of turbines and sluices for each tidal lagoon, the total area of turbines and sluices were divided according to the number of nodes representing the powerhouse.

For example, lagoon layout A_C1 has 22 turbines and 31 sluices. Turbine area is equal to 44 m^2 and the sluice area is equal to 56 m^2, as explained in Section 3.3.1. Therefore, the total areas of

the turbines and sluices are 968 m^2 and 1736 m^2, respectively. For model grid layout A_C1, there are 10 nodes for turbines and 10 nodes for sluice. Therefore each turbine node and sluice node would have an area of 96.80 m^2 and 173.60 m^2, respectively. Table 4.11 summarizes the number of nodes used for turbines and sluices at each tidal lagoon layout for two-way generation.

Predicted current velocity from the model might be higher at the powerhouse to realistic results since multiple structures (sluices or turbines) are represented by one node. Nevertheless, current velocities near the powerhouse (a few grid elements away from the powerhouse) should unify and generated reasonable results. Although this is out of the scope of this study, a three-dimensional model should be generated to investigate the hydrodynamics around the tidal lagoons.

Table 4.11: Number of nodes used for turbines and sluices for two-way generation.

	Turbine			**Sluice**		
Lagoon layout	**Number of turbines [-]**	**Number of turbine nodes [-]**	**Adjusted turbine area (m^2)**	**Number of sluices [-]**	**Number of sluice nodes [-]**	**Adjusted sluice area (m^2)**
A_C1[(i)]	24	10	105.60	15	10	84.00
A_O1[(i)]	14	8	77.00	15	11	76.36
A_C1	22	10	96.80	31	10	173.60
A_C2	30	10	132.00	41	10	229.60
A_C3	52	9	254.22	72	9	448.00
A_O1	12	8	66.00	23	11	117.09
A_O2	19	8	104.50	29	10	162.40
A_O3	23	8	126.50	39	12	182.00
B_C1	29	10	127.60	31	10	173.60
B_O1	12	9	58.67	22	11	112.00
C_C1	31	10	136.40	40	10	224.00
C_O1	12	8	66.00	22	11	112.00
D_C1	25	10	110.00	32	10	179.20
D_O1	12	8	66.00	23	11	117.09
E_C1	21	9	102.67	31	9	192.89
E_O1	12	8	66.00	23	10	128.80
F_C1	32	6	234.67	48	11	244.36
F_O1	12	7	75.43	23	13	99.08

4.4.3 Simulation period

For all the hypothetical scenarios, the simulations spanned over 14 days 18 hours and 30 minutes to capture a spring and neap tide. The simulation period was from 28/08/2007 00:00 to

11/09/2007 18:30. A warm-up simulation of 3-days was performed prior to the simulation to obtain reasonable water level and current velocities throughout the domain. The flow through the powerhouse was not calculated during the warm-up simulation.

4.5 Results

Every simulation was analysed in the aim to determine the following results:

- Water levels
    - Maximum water levels
    - Minimum water levels
    - Maximum tidal range
- Current velocities
    - Maximum current velocities
    - RMS current velocities
    - Residual currents
- Shear stress
    - Maximum shear stress
    - RMS shear stress
- Average power outputs

In addition to modeling hypothetical scenarios S1 to S19 as described above, the tidal flows for existing conditions without lagoons (scenario S0) were also modelled for the same 14.8 day period using the same boundary conditions. Changes in tidal hydrodynamics due to each hypothetical scenario with lagoons were estimated by differencing the model results for each hypothetical scenario from those determined for the existing conditions (no lagoons). The impact of each hypothetical scenario on water levels, tidal range, depth-averaged tidal current speed and bed shear stress have all been assessed in this manner.

4.5.1.1 Water level

A - Maximum water level

The maximum water level was determined by obtaining the maximum water level during the simulation. The analysis was done for every grid node. The maximum water level, η_{max}, is defined as

$$\eta_{max} = \max_{i=1 \to n} (\eta_i) \tag{4.18}$$

where η is the water level (m), i is the simulation step number, and n is the number of steps in the simulation.

B - Minimum water level

Using the same approach, the minimum water level was determined by obtaining the minimum water level during the simulation. The minimum water level, η_{min}, is defined as

$$\eta_{min} = \min_{i=1 \to n} (\eta_i) \tag{4.19}$$

where η is the water level (m), i is the simulation step number, and n is the number of steps in the simulation.

C - Maximum tidal range

The maximum tidal range at one node, Φ_{max},was determined by subtracting the minimum water level from the maximum water level, as shown in Equation (4.20).

$$\Phi_{max} = \eta_{max} - \eta_{min} \tag{4.20}$$

The maximum tidal range doesn't correspond to the maximum difference in height between consecutive high and low waters. It only corresponds to the maximum difference between the maximum and minimum water level obtained from the simulation.

4.5.1.2 Current velocity

A - Maximum current velocity

The maximum current velocity, V_{max}, was determined by obtaining the maximum current velocity during the simulation. It is defined as

$$V_{max} = \max_{i=1 \to n} \left(\sqrt{{u_i}^2 + {v_i}^2} \right) \tag{4.21}$$

where u_i, v_i are depth-averaged velocities at time step i in x, y direction, respectively (m/s), i is the simulation step number, and n is the number of steps in the simulation.

B - RMS current velocity

The RMS current velocity, V_{RMS}, was calculated using the following equation

$$V_{RMS} = \sqrt{\frac{\sum_{i=1}^{n} {V_i}^2}{n}} \tag{4.22}$$

where V_i is the depth-averaged velocity at time step *i* (m/s), i is the simulation step number, and n is the number of steps in the simulation.

C - Residual currents

The residual currents were calculated by

$$V_R = \sqrt{\left(\frac{\sum_{i=1}^{n} u_i}{n}\right)^2 + \left(\frac{\sum_{i=1}^{n} v_i}{n}\right)^2} \tag{4.23}$$

where u_i, v_i are depth-averaged velocities at time step *i* in x, y direction, respectively (m/s), i is the simulation step number, and n is the number of steps in the simulation.

4.5.1.3 Shear stress

A - Maximum shear stress

The maximum bottom shear stress, τ_{max}, is defined as

$$\tau_{max} = \max_{i=1 \to n} \left(\rho \frac{{u_i}^2 {v_i}^2}{C^2}\right) \tag{4.24}$$

where ρ is the density of water, u, v are depth-averaged velocities in x, y direction, respectively (m/s), and C is the Chézy coefficient.

B - RMS bottom shear stress

$$\tau_{RMS} = \sqrt{\frac{\sum_{i=1}^{n} \left(\rho \frac{{u_i}^2 {v_i}^2}{C^2}\right)^2}{n}} \tag{4.25}$$

where ρ is the density of water, u, v are depth-averaged velocities in x, y direction, respectively (m/s), and C is the Chézy coefficient.

4.5.2 Power output and power generation results

Every simulation was analysed in the aim to determine the average power output and the power generation for one spring-neap tidal cycle. Average power output, P_{avg}, is defined as

$$P_{avg} = \frac{\sum_{i=1}^{m}\left(\sum_{j=1}^{n} P_{i,j}\right)}{m} \tag{4.26}$$

where $P_{i,j}$ is the power output; defined in Table 3.1, i is the simulation step number, j is the turbine number, n is the number of turbine, , and m is the number of steps in the simulation. Results are given in megawatt (MW).

The power generation for one spring-neap tidal cycle, E_{cycle} is defined as

$$E_{cycle} = \sum_{j=1}^{m}\left(\sum_{i=1}^{n} P_{i,j} t_{step}\right) \tag{4.27}$$

where t_{step} is the time step. The power generation is given in gigawatt hour for one averaged spring-neap cycle.

4.5.3 Hydrodynamic changes

Hydrodynamic changes were determined by subtracting the results from the model without a tidal lagoon from the results with the presence of a tidal lagoon. The general change in a hydrodynamic variable, $\Delta\psi$, or the percentage difference, $(\Delta\psi)_{\%}$, are defined as

$$\Delta\psi = \psi_p - \psi_e \; or \; (\Delta\psi)_{\%} = \frac{\psi_p - \psi_e}{\psi_e} \times 100 \tag{4.28}$$

where ψ represents a hydrodynamic variable (e.g. maximum water level, minimum water level), ψ_e is a hydrodynamic variable from the model without the presence of tidal lagoons, and ψ_p is a hydrodynamic variable from a model with tidal lagoons.

4.6 Analysis of Results

Table 4.12 shows a summary table of the analysed results presented in this paper. S0 to S2 are presented Section 4.6 and S3 to S19 are presented in Annexe D. Table 4.14 shows a summary table of the change in maximum tidal range and RMS current velocity for S0 to S19. These changes are based on the reference stations and sites as shown in Table 4.13. The first five points of interest (1-5) were tabulated for maximum tidal range results, and the last five (6-10) were tabulated for RMS velocity. As shown in Figure 4.10, they are located throughout the domain to have a good representation of the changes that may occur in the Bay of Fundy and the Gulf of Maine.

Table 4.12: Simulation results presented herein.

	Simulation	Water level			Current velocity			Shear stress	Power
		Max. water level	Min. water level	Max. tidal range	Max. current velocity	RMS current velocity	Current circulation	Max. shear stress	Power out./gen.
Section 4.6	S0			x		x	x	x	
	S1	x	x		x		x	x	
	S2	x	x		x		x	x	
Appendix E	S3			x	x	x	x		x
	S4			x	x	x	x		x
	S5			x	x	x	x		x
	S6			x	x	x	x		
	S7			x	x	x	x		
	S8			x		x	x		
	S9			x		x	x		
	S10			x		x	x		
	S11			x		x	x		
	S12			x		x	x		
	S13			x		x	x		
	S14			x		x	x		
	S15			x		x	x		
	S16			x		x	x		
	S17			x		x	x		
	S18			x		x	x		
	S19			x		x	x		

Table 4.13: Reference stations and sites.

	Name	**Longitude**	**Latitude**	**Distance from Site A (km)**
For maximum tidal range	Boston	-71.052	42.355	675
	BarHarbor	-68.205	44.392	400
	Saint John	-66.067	45.267	175
	Chignecto	-64.983	45.483	125
	Five Islands	-64.067	45.383	15
For RMS current velocity	Minas Basin	-64.211	45.314	25
	Minas Passage	-64.443	45.349	35
	MB Entrance	-64.784	45.224	75
	CB Entrance	-65.043	45.450	115
	Chignecto	-64.652	45.636	150

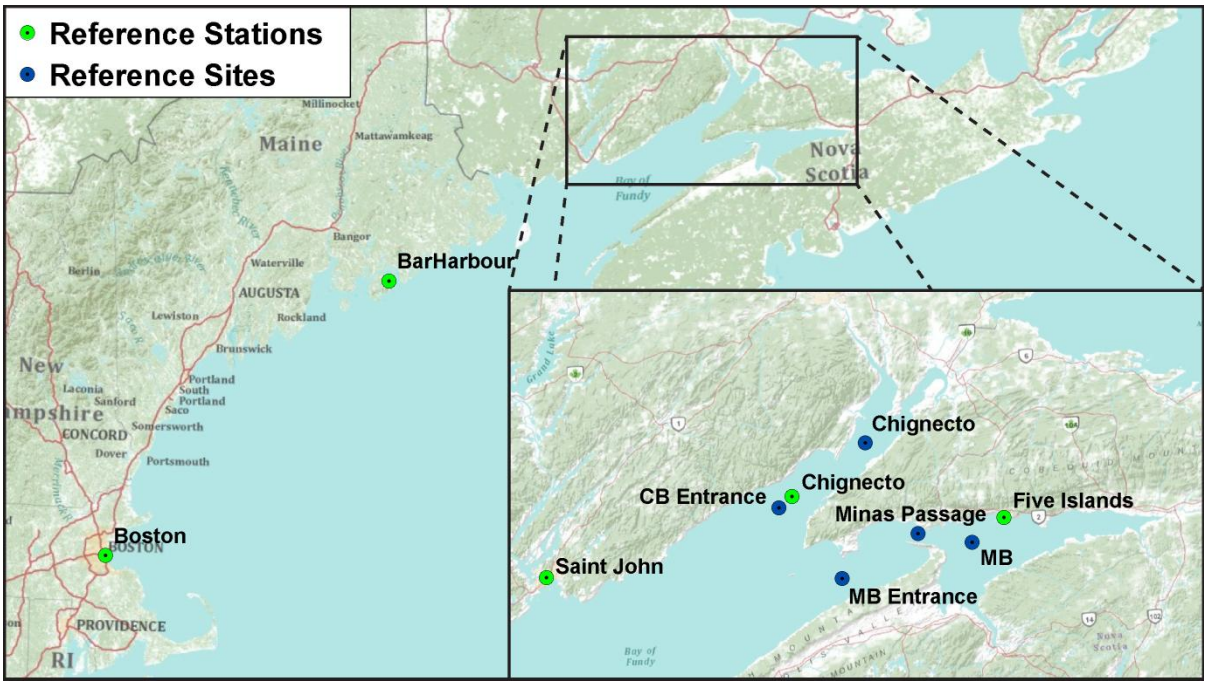

Figure 4.10: Reference stations and sites.

4.6.1 Simulation without tidal lagoons (S0)

A - Water level: Maximum tidal range

Figure 4.11 shows the maximum tidal range in the Upper Bay of Fundy for S0. Its amplitude varies from 11 to 14 m in Minas Basin and 10 to 12 m in Chignecto Bay. The simulation period was taken during an averaged spring and neap tides; therefore maximum tidal range values do not reach extreme values of 15 to 16 m recorded in the Minas Basin. The highest tidal ranges were found to be around 13 to 14 m in the middle of the Minas Basin in between Economy and Highland Village.

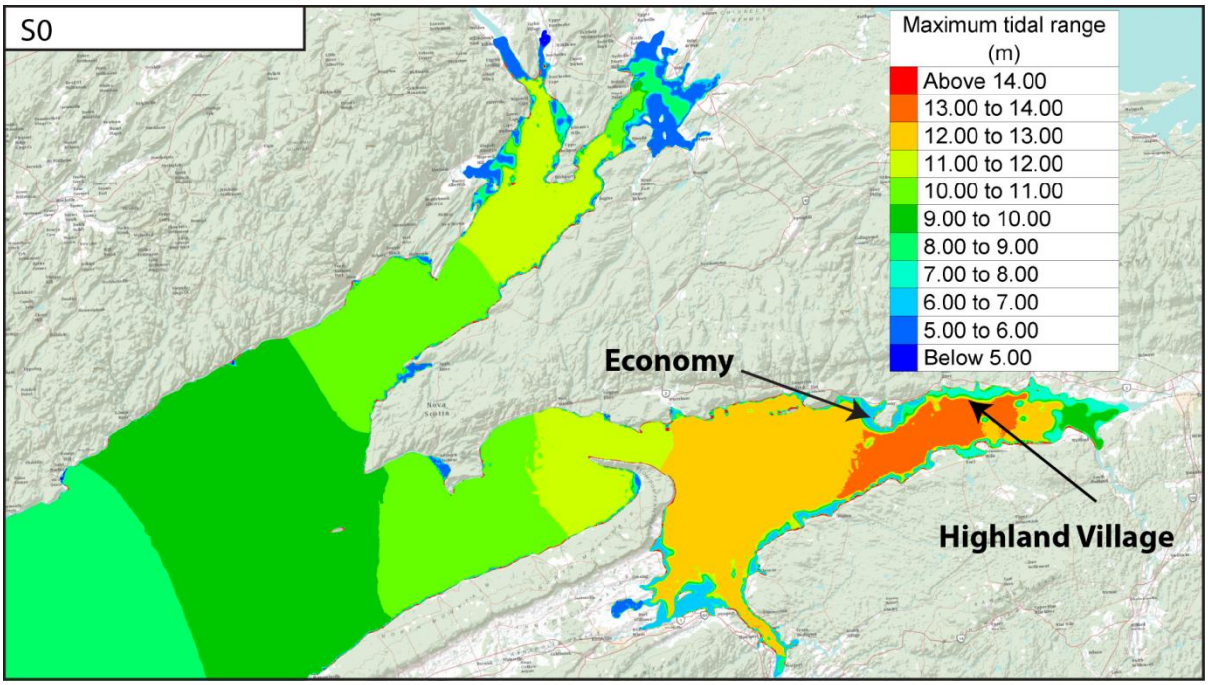

Figure 4.11: Maximum tidal range for S0.

B - Current velocity: RMS current velocity

The RMS velocity of depth-averaged currents is mapped in Figure 4.12. The most intense current was found around Cape Split, located on the southern coast of Minas Passage. RMS velocities were estimated to be around 1.50 to 2.50 m/s. In other regions in the Upper Bay of Fundy, such as Minas Basin and Chignecto Bay, RMS velocities were estimated to be around 0.5 to 1.5 m/s.

A - Shear stress: Maximum shear stress

The maximum shear stress of depth-averaged currents is mapped in Figure 4.13. There is a strong correlation between shear stress and current velocity since water depth and bottom roughness does not vary by much throughout the Minas Basin. Shear stress is a function velocity, water depth and bottom roughness.

As shown in Figure 4.13, significant current activities were found around Cape Split where maximum shear stresses were estimated to be around 14.00 to 25.00 Pa. In other regions of the Bay of Fundy, maximum shear stresses were estimated to be around 2.00 to 8.00 Pa.

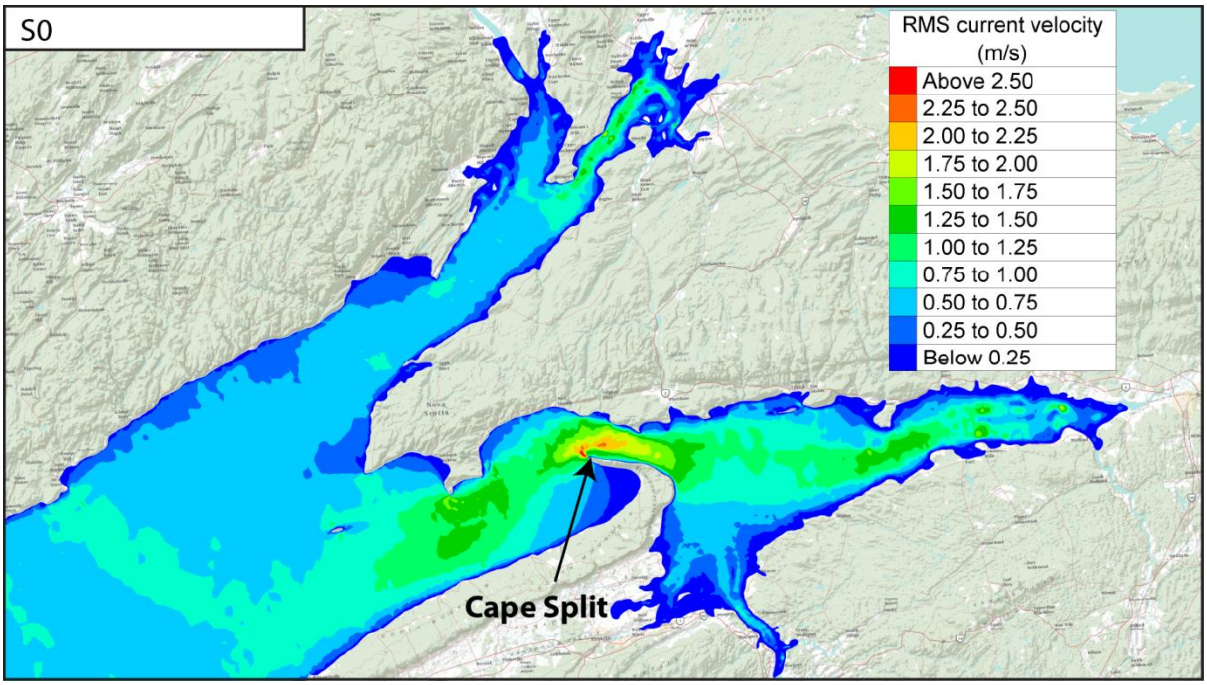

Figure 4.12: RMS current velocity and circulation patterns for S0.

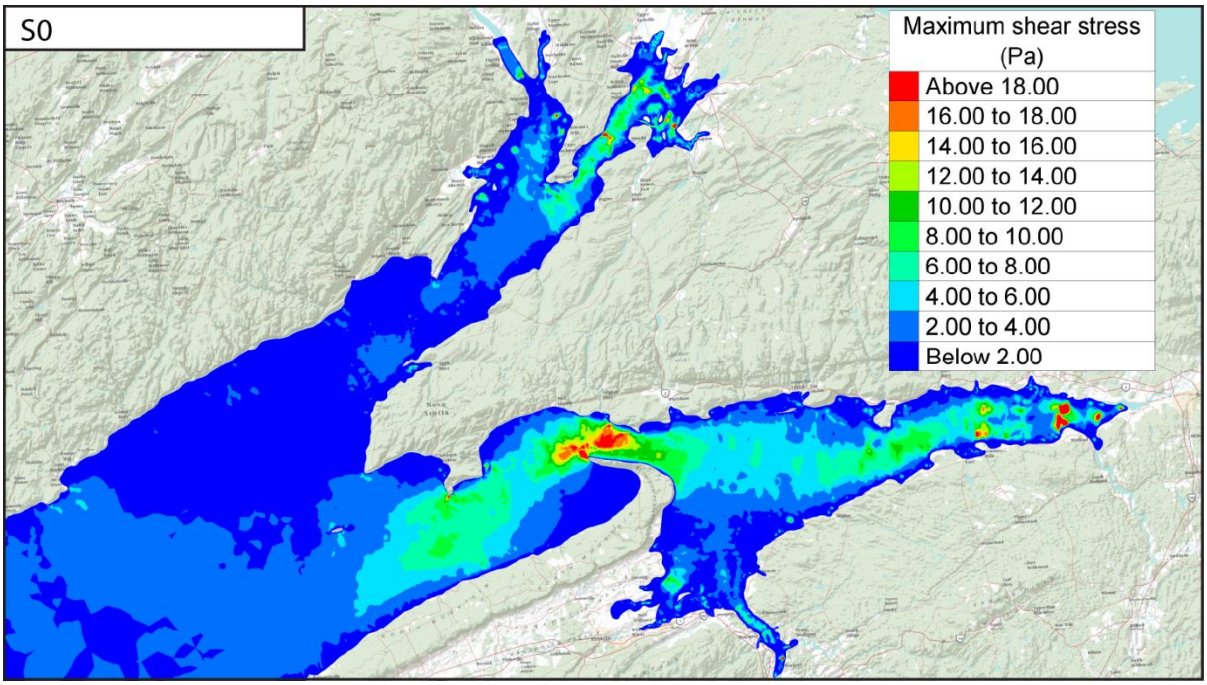

Figure 4.13: Maximum shear stress for S0.

4.6.2 Coastal and offshore lagoons proposed by DMC (S1 and S2)

A - Water Levels: Maximum water level and minimum water levels

Figure 4.14.a and Figure 4.14.b shows the change in maximum water levels due to the coastal and offshore tidal lagoon, respectively. These lagoons were proposed by DMC. For the coastal

tidal lagoon, the high water levels will increase by 2 to 4 cm at the entrance of Minas Basin and Chignecto Bay, and by 1 to 2 cm in the lower Bay of Fundy. As for the offshore tidal lagoon, high water levels will only increase between 1 and 2 cm in some location in the Upper Bay of Fundy. These two tidal lagoons show no change in high water levels in the Gulf of Maine. Figure 4.15.a and Figure 4.15.b show the change in minimum water levels due to the coastal and offshore lagoon, respectively. The changes in minimum water levels are less than the changes in high water levels for both cases. Results show a decrease in water levels by 1 to 2 cm in the Bay of Fundy for the coastal tidal lagoon and no change for the case of the offshore tidal lagoon.

By far, the largest changes in water levels occur within the lagoon itself, where tidal range is reduced by several meters, relative to existing conditions. The exact tidal range reduction will depend on the operation schemes and the characteristics of turbines and sluices. For S1 and S2, the estimated reduction in tidal range is around 7.0 m for the coastal tidal lagoon and around 5.6 m for the offshore tidal lagoon.

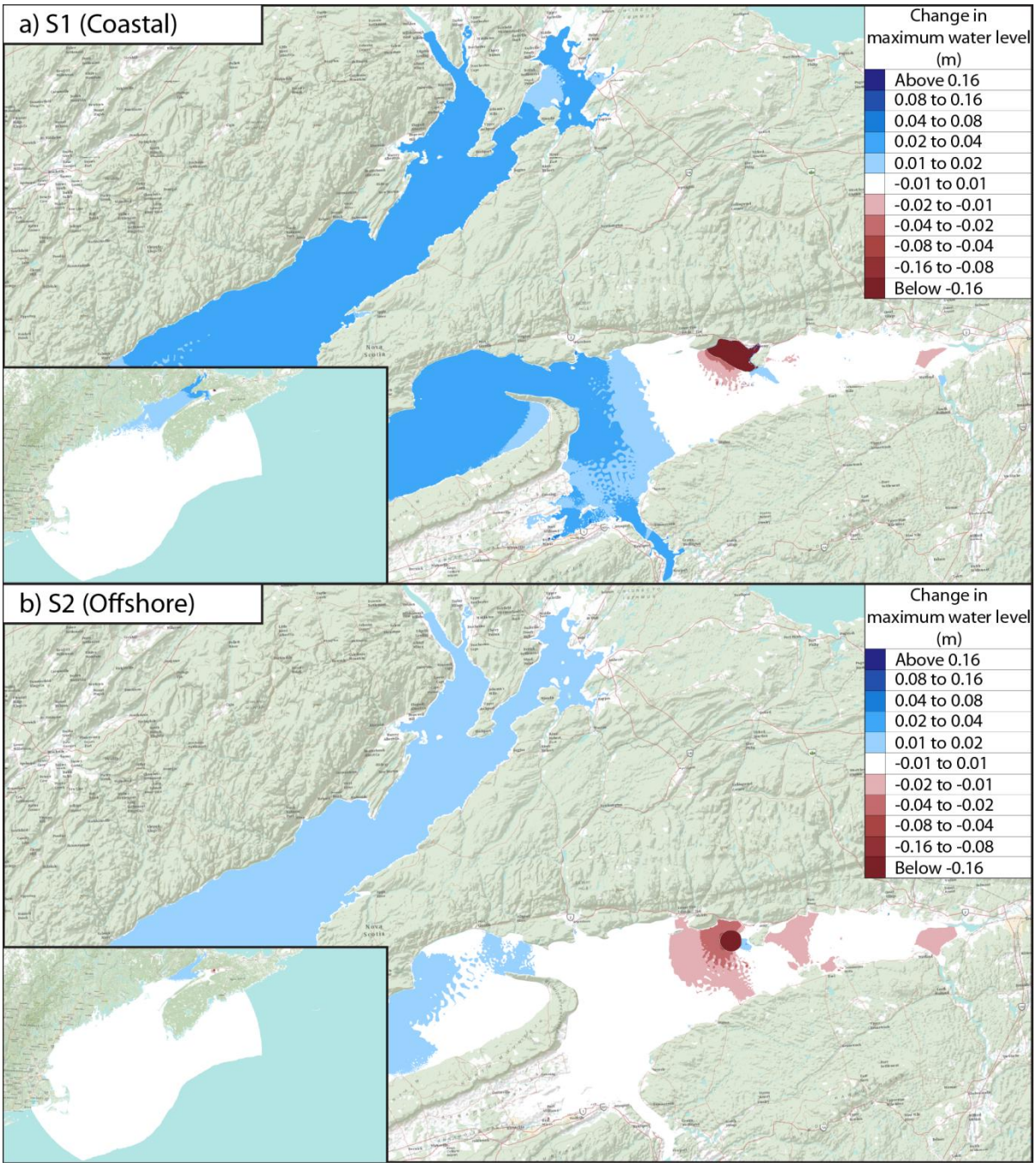

Figure 4.14: Changes in maximum water levels for S1 and S2.

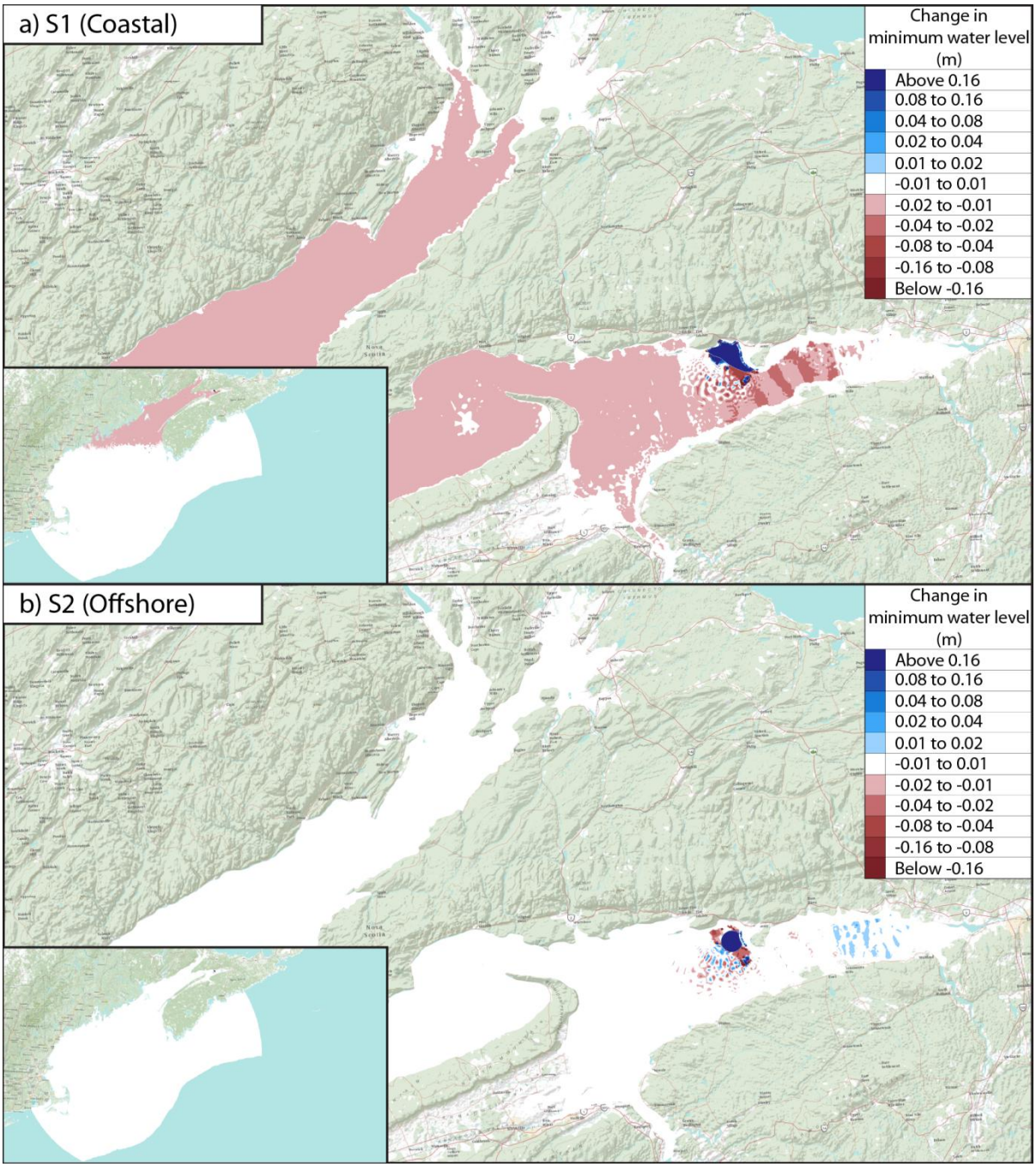

Figure 4.15: Changes in minimum water level for S1 and S2.

B - Current velocities: Maximum current velocities and residual current

Predicted changes in the maximum velocities of the depth-averaged tidal currents due to the studied coastal and offshore lagoons operating in Minas Basin are mapped in Figure 4.16.a and Figure 4.16.b, respectively. The maximum tidal current in Minas Passage will be approximately 2 to 4 cm/s slower with the coastal tidal lagoon and from 1 to 2 cm/s slower with the offshore tidal lagoon. This change represents a 1% to 2% reduction in the peak velocities in Minas Pas-

sage. However, changes in the maximum tidal current due to both lagoon schemes remain below 1 cm/s throughout most of the Bay of Fundy and inside the entire Gulf of Maine. Hence, for the lagoons considered in this study, tidal currents outside Minas Basin are very weakly affected, if at all.

Figure 4.17.a and Figure 4.17.b shows the predicted flow field from residual currents near the coastal and offshore lagoon, respectively. In these figures, the colour pattern denotes the change in maximum current velocities while the black arrows indicate the average flow direction and its magnitude at each node. The tidal lagoon will induce changes in the direction and strength of tidal currents both within the lagoon and outside it, especially near the powerhouse and along the external perimeter of the impoundment dike. The pattern of these local changes is rather complex and depends on many factors such as the lagoon location, the local bathymetry, the configuration of the impoundment dike and of the shoreline, and the configuration and location of the powerhouse.

For these lagoons, velocities will increase near the powerhouse, on the seaward side, by 0.40 to 1.60 m/s. Inside the tidal lagoon, maximum velocities will not change near the powerhouse but will decrease as low as 0.80 m/s. Velocities at the powerhouse were not investigated because the predicted velocities might be higher at the powerhouse to realistic results since multiple structures (sluices or turbines) are represented by one node. Nevertheless, current velocities near the powerhouse (a few grid elements away from the powerhouse) should unify and generated reasonable results.

C - Shear stress: Maximum shear stress

Predicted changes in the bottom shear stress due to the studied coastal and offshore lagoons operating in Minas Basin are mapped in Figure 4.18.a and Figure 4.18.b, respectively. The maximum shear stress in Minas Passage will decrease by 0.40 to 0.80 Pa in the presence of the coastal lagoon, and by 0.20 to 0.40 Pa in the presence of the offshore lagoon. The change in shear stress near the tidal lagoon is more pronounced because of the increase in current velocity. The maximum shear stress near the lagoon will increase by 15 to 25 Pa with the coastal lagoon, and by 10 to 20 Pa with the offshore lagoon.

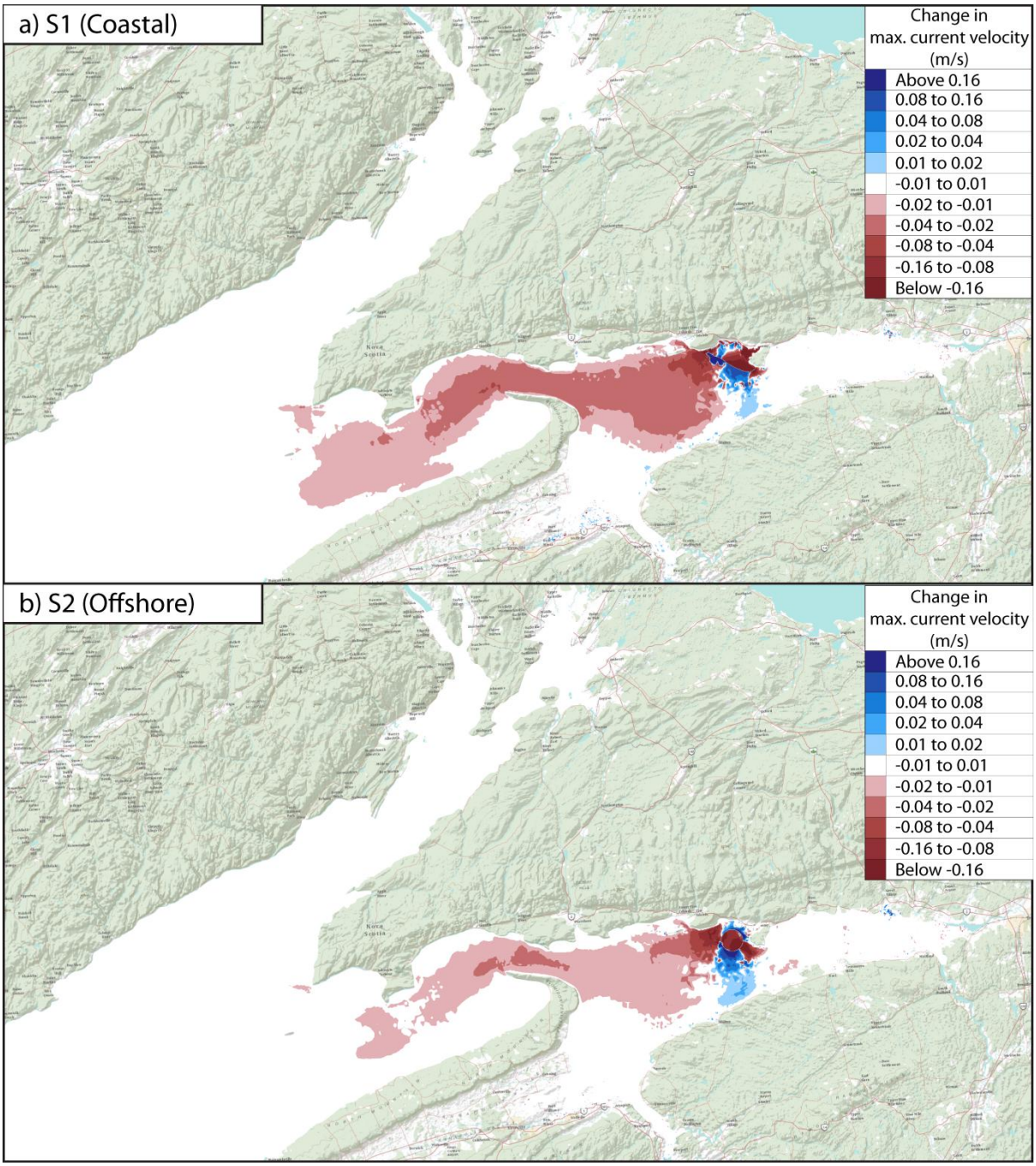

Figure 4.16: Changes in maximum current velocity for S1 and S2.

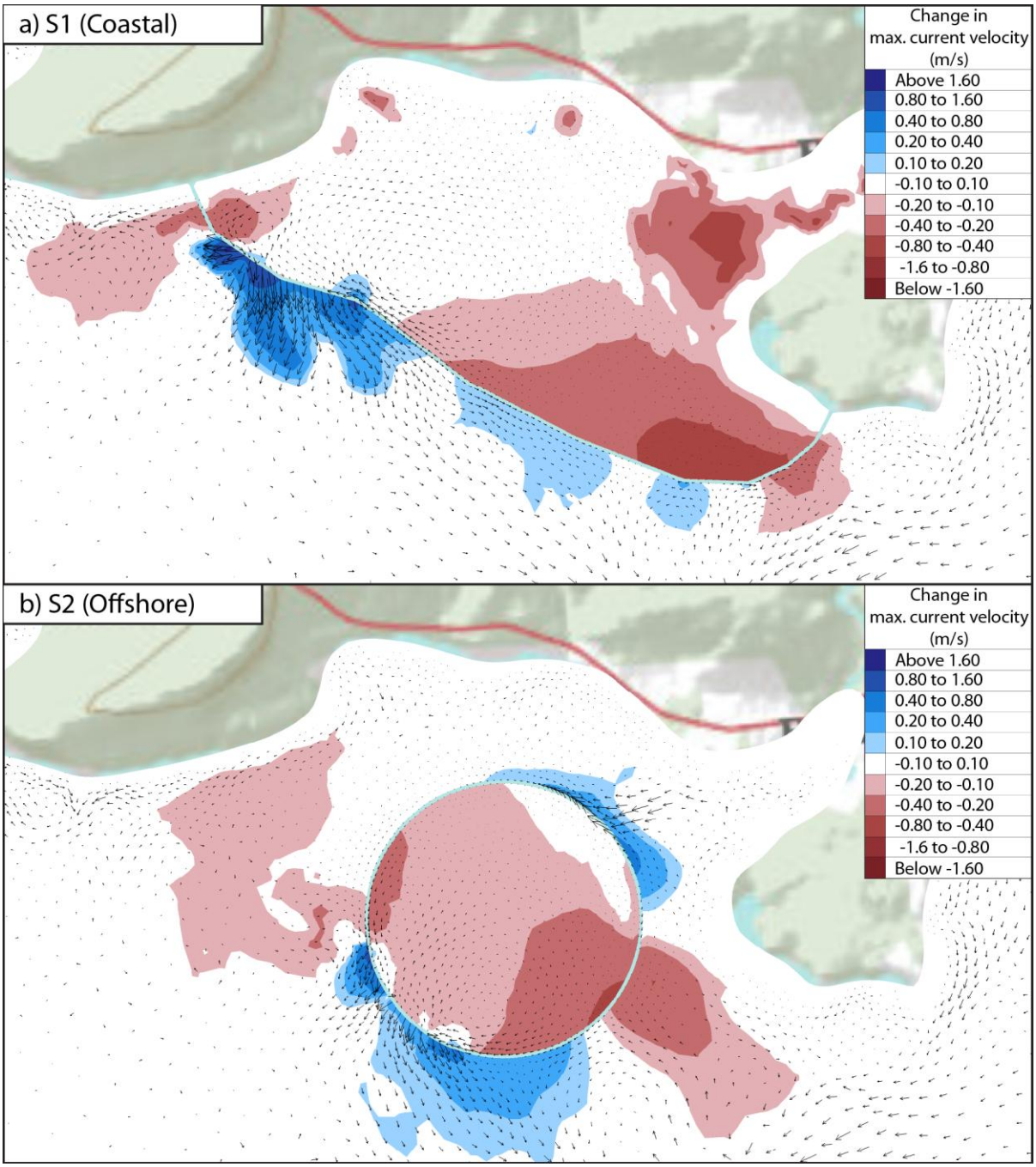

Figure 4.17: Changes in maximum current velocity and residual current circulation for S1 and S2 near the tidal lagoon.

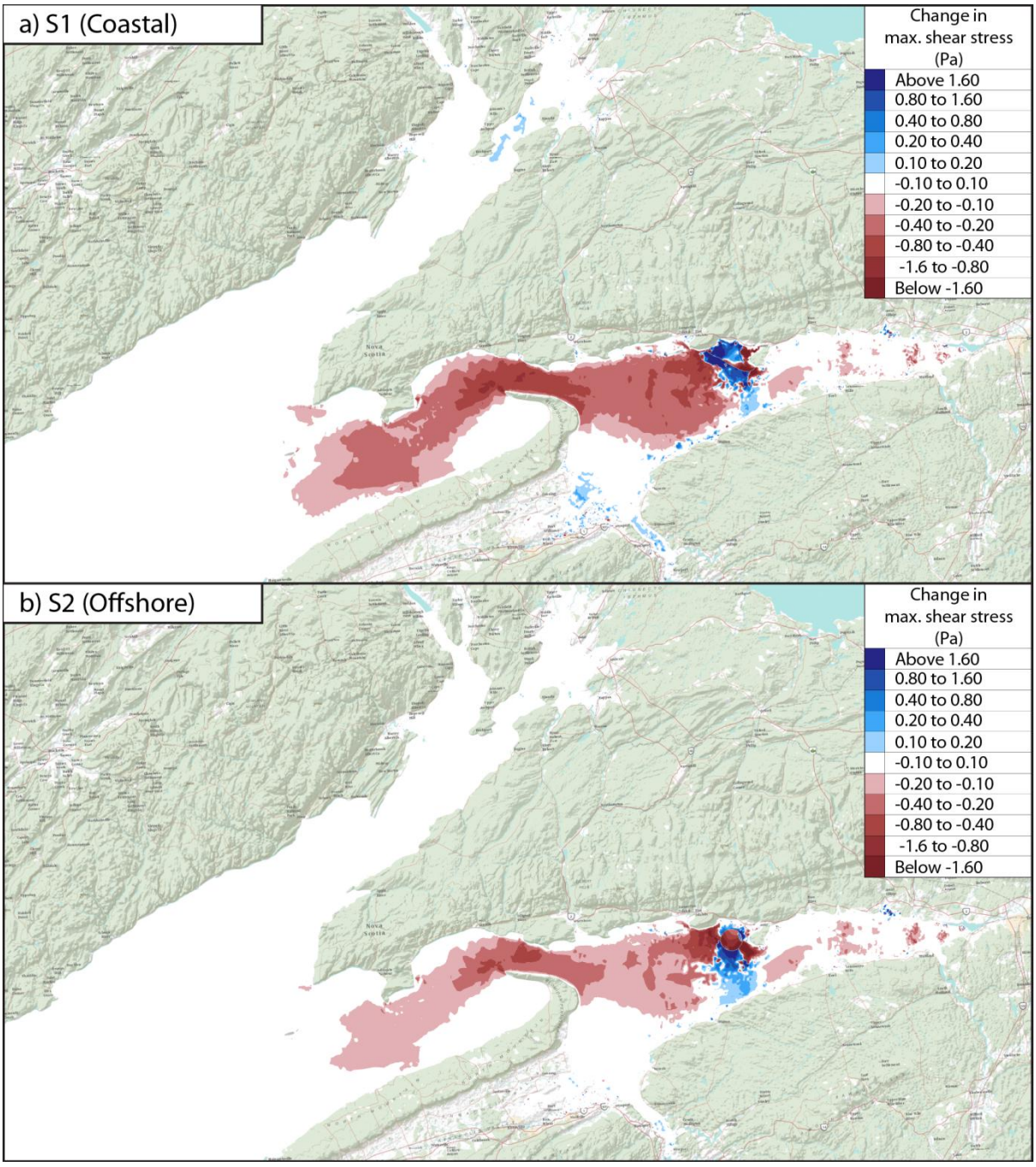

Figure 4.18: Changes in maximum shear stress for S1 and S2.

Table 4.14: Summary of simulation results.

		Maximum tidal range, Φ_{max}					RMS current velocity, V_{RMS}					Averaged power output[1]	Power generation for one spring-neap tidal cycle
		Boston (m)	Bar Harbour (m)	Saint John (m)	Chignecto (m)	Five Islands (m)	Minas Basin (m/s)	Minas Passage (m/s)	MB Entrance (m/s)	CB Entrance (m/s)	Chignecto (m/s)	(MW)	(GWh)
S0		3.60	3.89	7.32	10.14	12.76	0.22	2.01	0.37	0.58	0.70	0	0
S1	Δ	0.4%	0.5%	0.5%	0.4%	0.0%	-13.4%	-2.2%	-5.1%	0.2%	0.4%	202	71
S2	Δ	0.3%	0.3%	0.2%	0.2%	-0.1%	-7.9%	-1.4%	-3.2%	0.2%	0.1%	123	42
S3	Δ	0.4%	0.5%	0.5%	0.4%	0.1%	-14.4%	-2.4%	-5.6%	0.2%	0.4%	203	72
S4	Δ	0.5%	0.4%	0.5%	0.4%	0.0%	-12.0%	-1.9%	-4.3%	0.3%	0.4%	168	60
S5	Δ	0.4%	0.4%	0.5%	0.4%	0.0%	-11.6%	-1.9%	-4.3%	0.3%	0.4%	108	37
S6	Δ	0.3%	0.3%	0.2%	0.1%	-0.7%	-7.4%	-1.4%	-3.7%	0.0%	0.1%	0	0
S7	Δ	0.4%	0.5%	0.5%	0.5%	0.4%	-11.6%	-1.8%	-3.5%	0.5%	0.6%	0	0
S8	Δ	0.7%	0.8%	0.7%	0.6%	0.2%	-20.8%	-3.5%	-8.0%	0.3%	0.6%	288	102
S9	Δ	1.2%	1.6%	1.2%	1.0%	*	-38.0%	-6.4%	-14.4%	0.7%	1.0%	508	180
S10	Δ	0.3%	0.3%	0.2%	0.2%	-0.1%	-8.3%	-1.4%	-3.5%	0.0%	0.1%	109	39
S11	Δ	0.4%	0.5%	0.4%	0.3%	-0.1%	-13.9%	-2.4%	-5.6%	0.2%	0.3%	185	66
S12	Δ	0.6%	0.7%	0.6%	0.5%	-0.1%	-19.4%	-3.3%	-7.5%	0.3%	0.4%	230	82
S13	Δ	0.5%	0.6%	0.8%	0.7%	0.9%	-16.2%	-2.4%	-4.8%	0.7%	0.7%	282	100
S14	Δ	0.6%	0.8%	0.5%	0.4%	0.0%	-12.5%	-3.9%	-9.4%	0.2%	0.4%	295	105
S15	Δ	1.7%	2.2%	1.7%	1.4%	0.8%	-45.8%	-9.0%	-20.3%	0.9%	1.4%	774	274
S16	Δ	0.7%	1.0%	0.7%	0.5%	0.0%	-20.8%	-4.6%	-11.0%	0.2%	0.4%	320	114
S17	Δ	2.4%	0.8%	0.0%	-0.9%	-0.4%	-2.3%	-0.5%	-2.1%	-12.0%	-18.5%	533	189
S18	Δ	1.3%	0.4%	-0.2%	-0.9%	-0.6%	-2.8%	-0.6%	-2.7%	-8.2%	-14.1%	223	79
S19	Δ	2.0%	1.5%	0.5%	-0.4%	-0.8%	-23.1%	-5.2%	-13.6%	-8.0%	-13.6%	565	190

* Invalid data; [1]Averaged power output for an averaged spring-neap cycle

4.7 Relationships between tidal lagoon characteristics and hydrodynamic impacts

The results from Table 4.14 were analysed to find relationships between tidal lagoon characteristics and hydrodynamic impacts such as:

- Average power output and tidal lagoon's impoundment area;
- Hydrodynamic impacts due to different operation modes; and,
- Hydrodynamic impacts due to different lagoon layout characteristics.

4.7.1 Power output and tidal lagoon's impoundment area

Figure 4.19 shows the average power output with respect to tidal lagoon's impoundment area. The triangular and circular symbols stand for results from the proposed scenarios with coastal and offshore tidal lagoons, respectively. Two equations were best fitted to the dataset; one for coastal tidal lagoons and the other for offshore tidal lagoons. They are given as

$$A = 0.1197 \cdot P_{avg} + 0191 \quad \text{for coastal tidal lagoons} \tag{4.29}$$

$$A = 0.1234 \cdot P_{avg} - 3.9672 \quad \text{for offshore tidal lagoons} \tag{4.30}$$

where A is the lagoon's impoundment area at an elevation of +4 m above mean sea level (km^2), and P_{avg} is the average power output (MW). These equations are only applicable for a two-way operation mode operating in Minas Basin. These equations were not developed for lagoons in Chignecto Bay because of the lack of data.

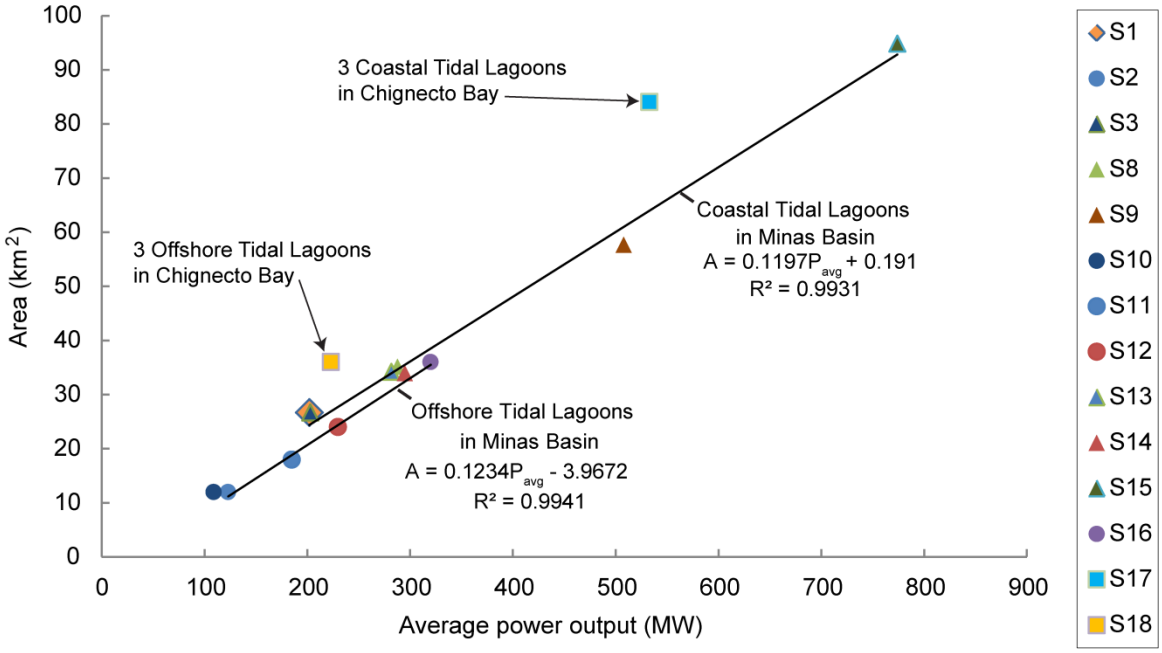

Figure 4.19: Tidal lagoon's impoundment area versus average power output for S1 to S18.

4.7.2 Hydrodynamic impacts due to different operating mode

4.7.2.1 Maximum tidal range

The graph shown in Figure 4.20 was prepared to illustrate the influence of the operating mode on the changes in maximum tidal range induced by a 26.7 km^2 coastal lagoon in Minas Basin located at site A. The changes in maximum water levels at the five reference stations mapped in Figure 4.10 are plotted in Figure 4.20 as a function of the distance from site A. Different symbols are used to represent the results from scenarios S3-S7. The water level at Five Islands, located only 15 km from site A, is relatively sensitive to the operating mode, whereas the water level at more distant sites, such as Bar Harbor and Boston, are fairly insensitive to changes in operating mode. These results show that the far-field change in tidal range is minimized for scenario S6, where the sluice gates are always open, and maximized for scenario S7, where the sluices are always closed. The hydrodynamic impacts at each reference station are similar for the three different power generating operating modes modelled in scenarios S3, S4 and S5 (2-way generation, ebb-generation and flood-generation, respectively).

4.7.2.2 RMS of current velocity

The changes in maximum depth-averaged current speed at the five reference sites mapped in Figure 4.10 are plotted in Figure 4.21 as a function of the distance from site A. Different symbols are used to present the results from scenarios S3-S7. At each site, the impacts are smallest

for scenario S6, where the sluice gates are always open, and largest for scenario S3, where a 2-way generation scheme was modelled. The predicted changes in tidal flows at distant locations are very small and quite insensitive to changes in operating mode. As expected, closer to the lagoon, the changes are larger and more sensitive to the operating mode.

4.7.3 Hydrodynamic impacts due to different lagoon layout characteristics

4.7.3.1 Change in maximum tidal range at Boston and Saint John

The predicted impacts of the various hypothetical scenarios considered in this study on the maximum tidal range at Boston are plotted in Figure 4.22 (tidal range versus average power output). Blue diamonds are used to denote results for scenarios with tidal lagoons in Minas Basin (scenarios S1-S3 and S8-S16), violet squares denote results for scenarios S17 and S18, with tidal lagoons in Chignecto Bay, and a red diamond denotes the result for scenario S19, where lagoons in Minas Basin and Chignecto Bay were modelled together. For tidal power lagoons located in Minas Basin, these results reveal a strong linear relationship between the power output and the change in amplitude of the Boston tides. Although lagoons in Chignecto Bay were only considered in two scenarios, these results also suggest a linear relationship between power output and the change in the amplitude of the tides at Boston. Greater power generation is clearly linked to more significant hydrodynamic impacts. Moreover, for the same power output, the impact on the Boston tidal levels due to the presence of tidal power lagoons in Chignecto Bay will be roughly double the impact due to lagoons in Minas Basin. In other words, tides at Boston are roughly twice as sensitive to power generation in Chignecto Bay compared to equivalent power generation in Minas Basin.

The predicted change in the maximum tidal range at Saint John is plotted versus average power output in Figure 4.23. Again, the results indicate a strong linear relationship between power generation in Minas Basin and the impact on the tidal range at Saint John. Greater power generation is again clearly linked to stronger hydrodynamic impacts. However, results for scenarios with lagoons in Chignecto Bay do not follow this rule. In fact, although only two data points are available and they suggest that producing power in Chignecto Bay has virtually no impact on the tidal range at Saint John.

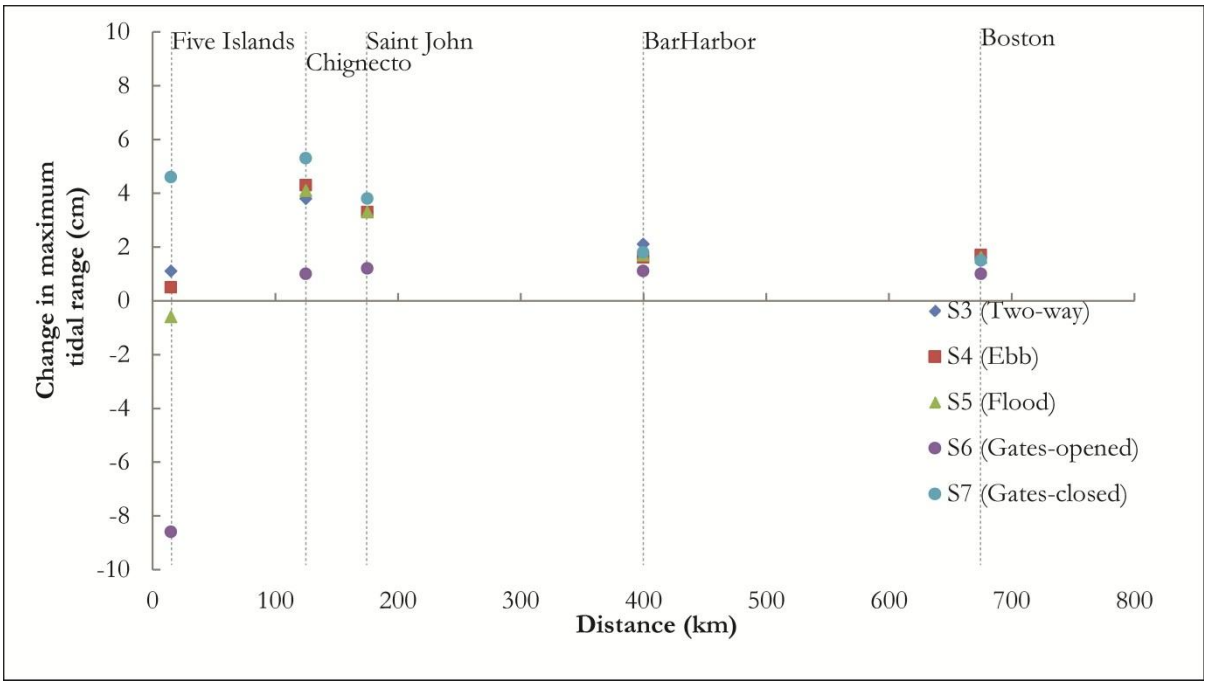

Figure 4.20: Changes in maximum tidal range with respect to distance due to different operation mode.

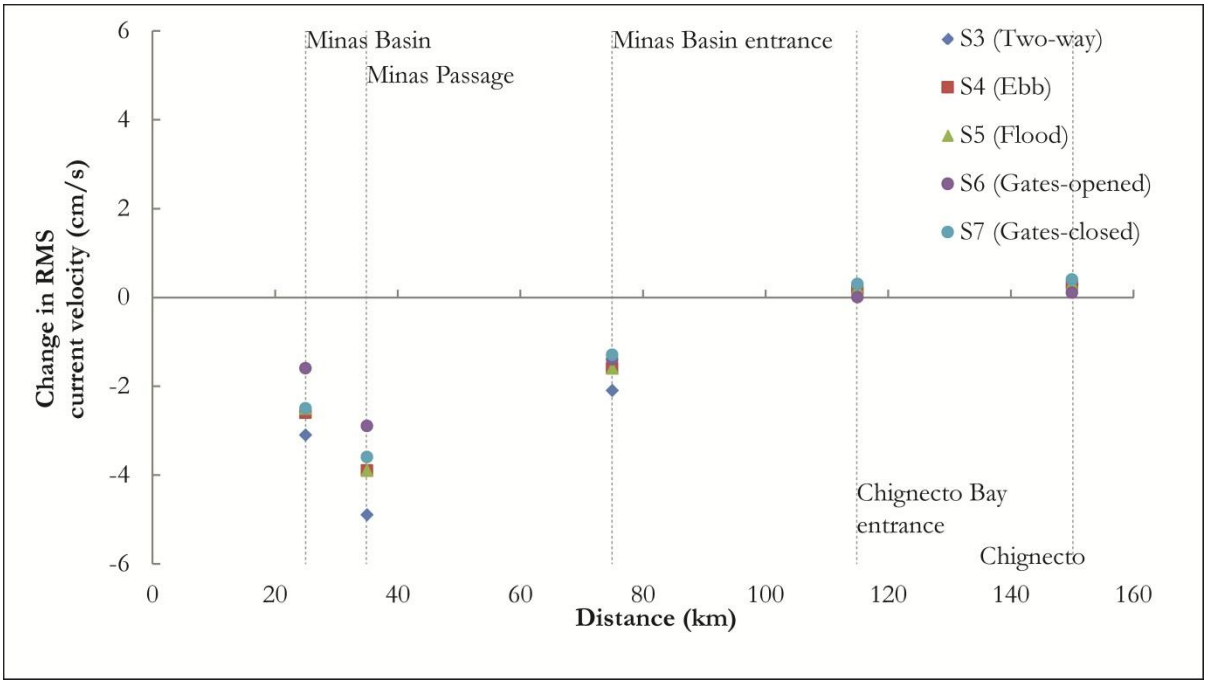

Figure 4.21: Changes in RMS current velocity with respect to distance due to different operation mode.

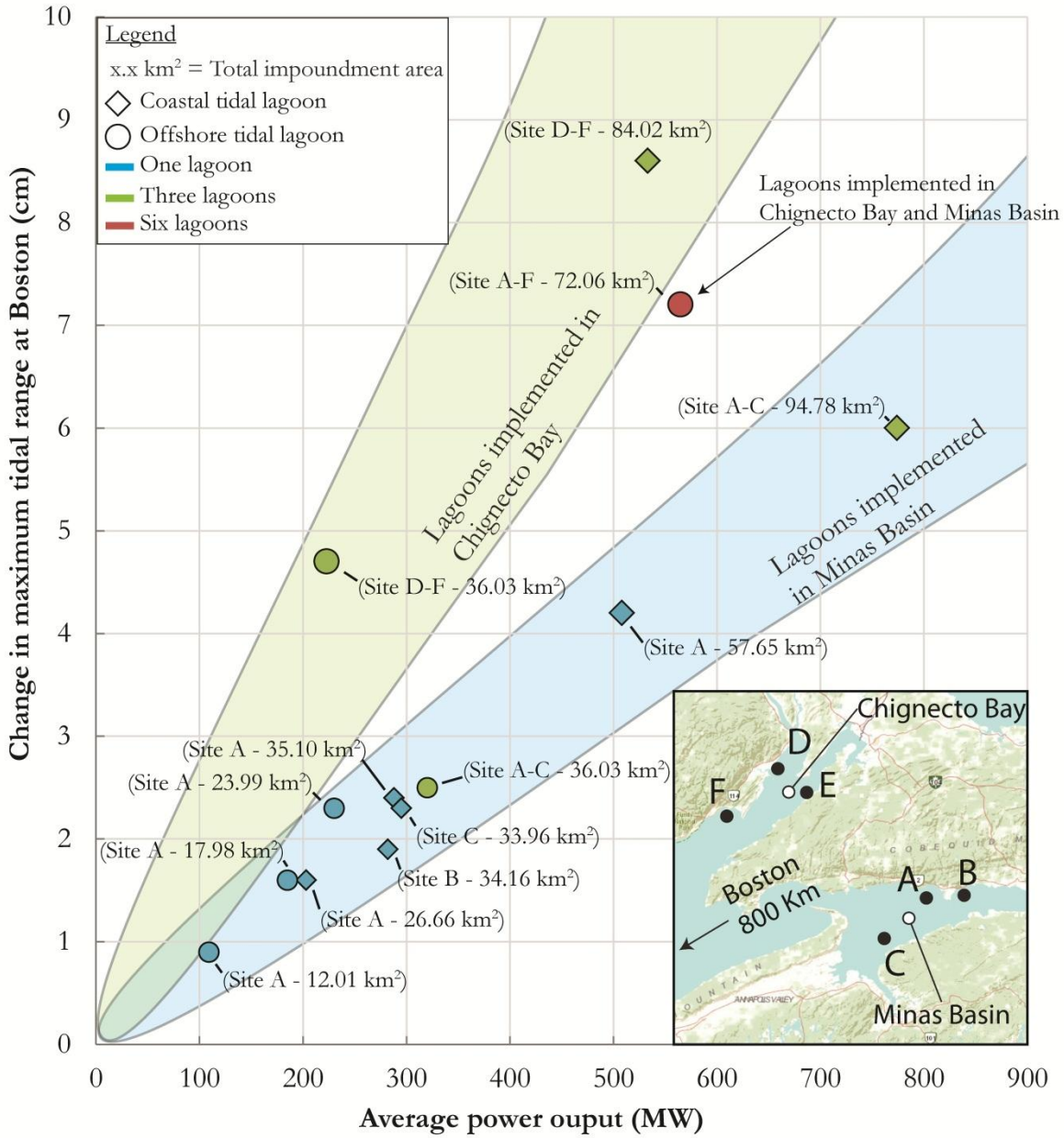

Figure 4.22: Changes in maximum tidal range with respect to average power output at Boston for different hypothetical scenarios.

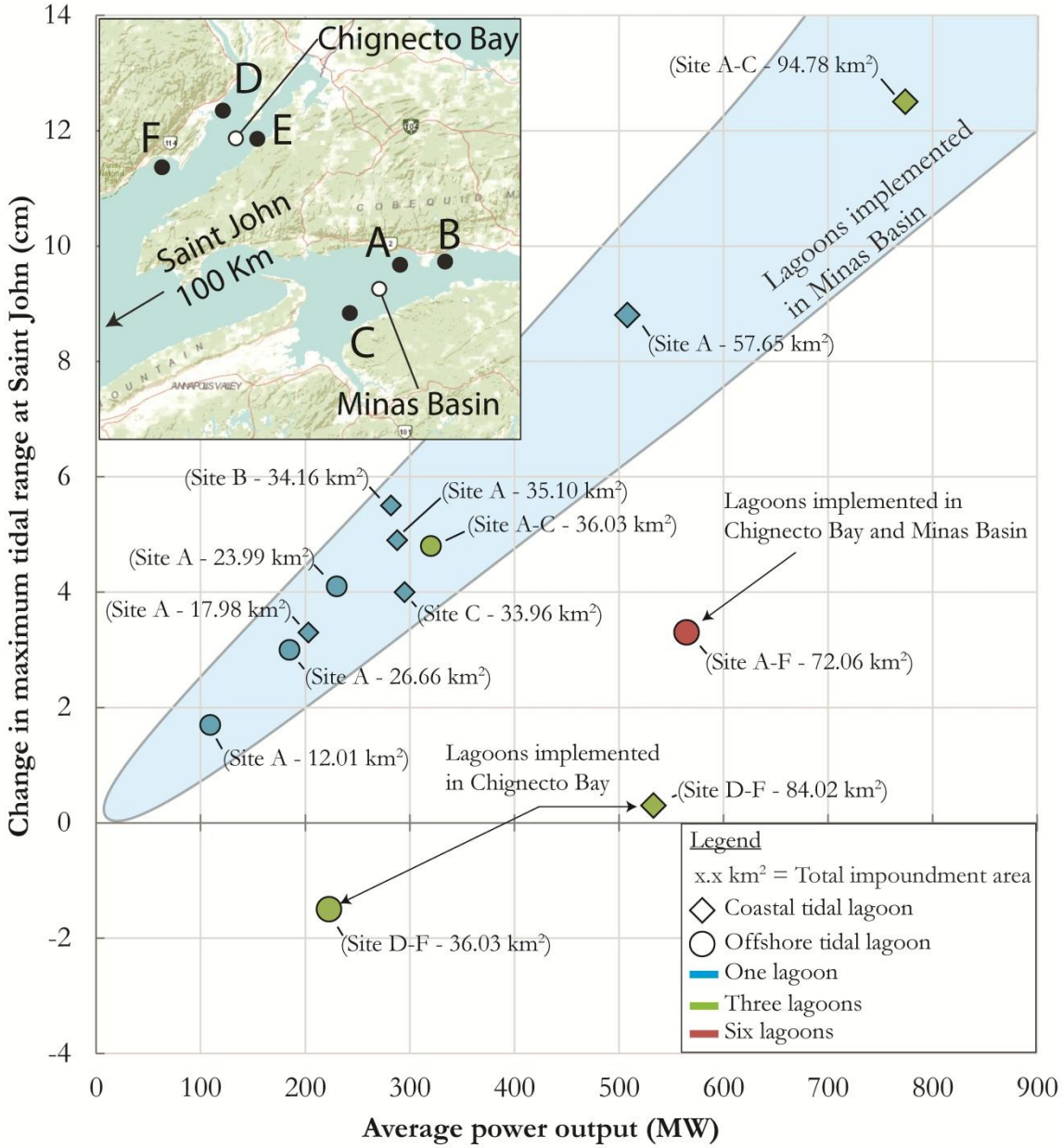

Figure 4.23: Changes in maximum tidal range at Saint John with respect to average power output for different hypothetical scenarios.

4.7.3.2 Change in maximum tidal range throughout the Bay of Fundy and the Gulf of Maine

The variation in hydrodynamic impacts (change in maximum tidal range) with distance for scenarios S3 and S8-S14 is plotted in Figure 4.24. All these scenarios feature a single tidal power lagoon operating in Minas Basin. Coastal lagoons at site A were modelled for scenarios S3, S8, and S9. Offshore lagoons at site A were modelled for scenarios S10-S12, and coastal lagoons at sites B and C were modelled for scenarios S13 and S14, respectively. In all cases, the magnitude of the hydrodynamic impacts attenuates with increasing distance from the lagoons. The pattern of attenuation is similar for all lagoons at sites A and C. However, the pattern for site B is different: the near-field change in tidal range for scenario S13 (coastal lagoon at site B) is significantly larger than for all other cases. Figure 4.24.a and Figure 4.24.b also highlight the strong dependence of far-field hydrodynamic impact on lagoon size. The magnitude of the change in tidal range increases linearly with increasing lagoon size (area).

4.7.3.3 RMS current velocity in Minas Passage

The predicted change in RMS current speed at Minas Passage for each of the various hypothetical scenarios considered in this study is plotted in Figure 4.25 as a function of average power output. These results reveal the presence of a strong linear relationship between power generation from tidal lagoons in Minas Basin and reductions in current velocities in Minas Passage. They also show that flows at Minas Passage are not sensitive to power generation from tidal lagoons installed in Chignecto Bay.

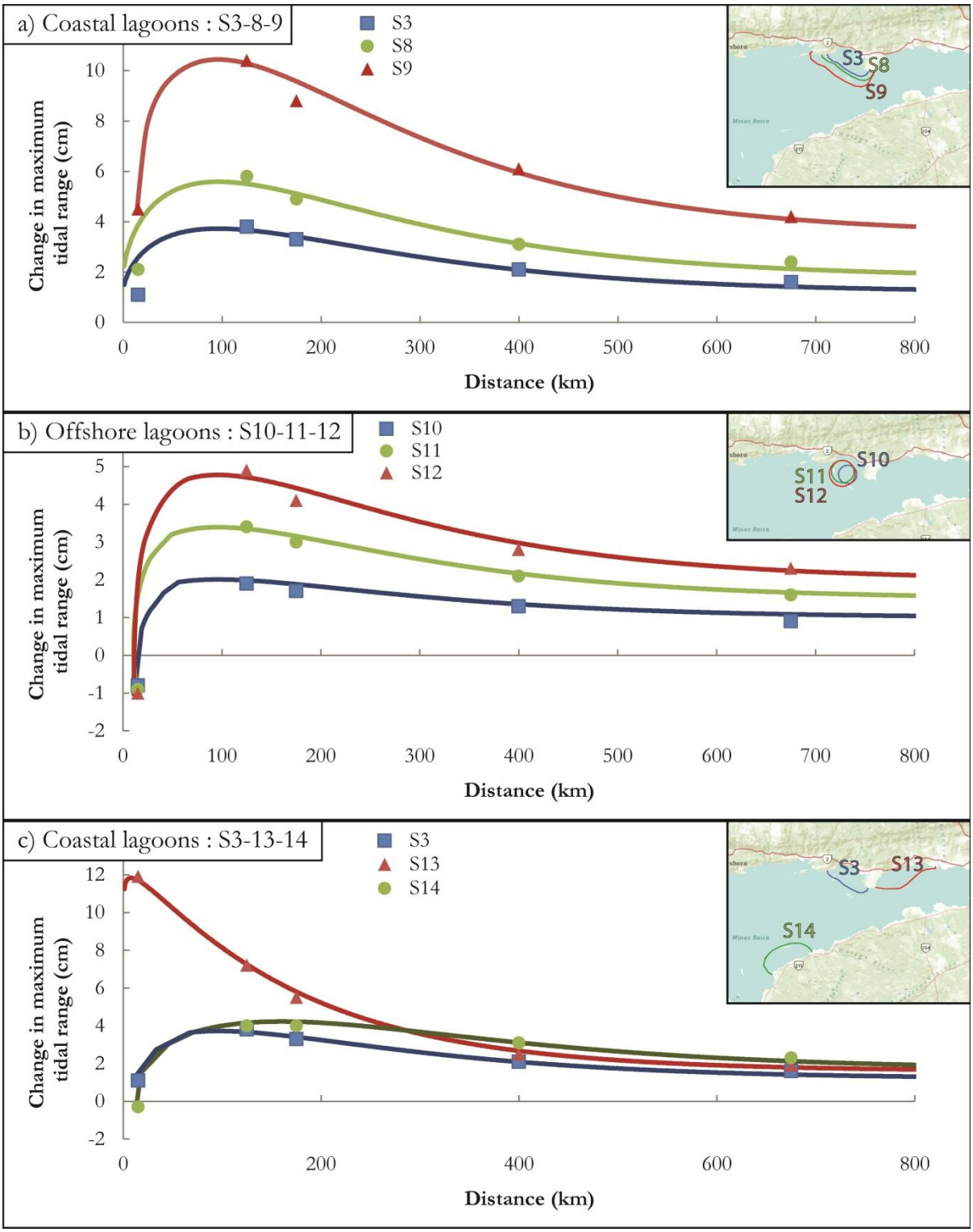

Figure 4.24: Changes in maximum tidal range with respect to distance for different hypothetical scenarios.

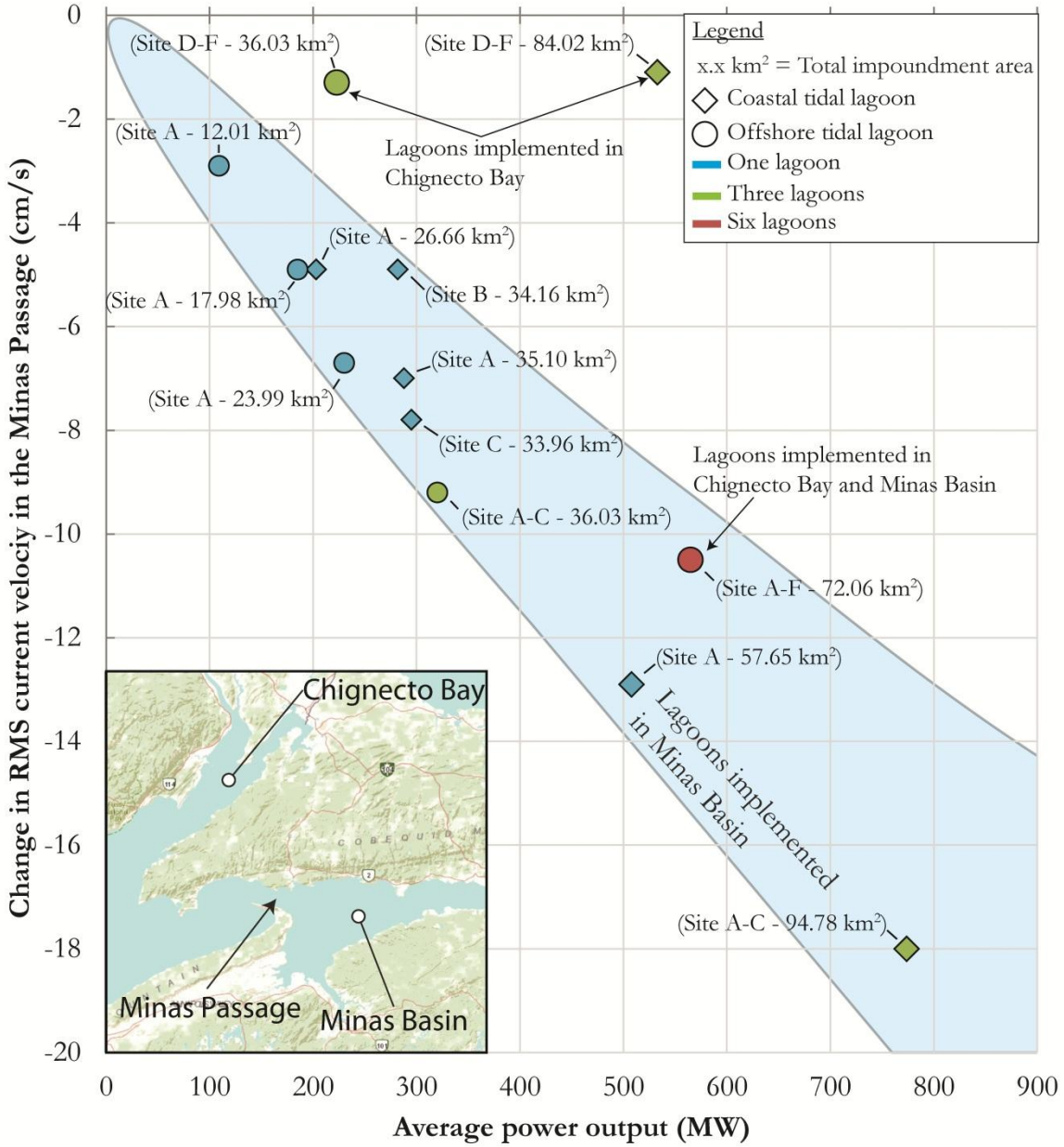

Figure 4.25: Changes in RMS current velocity in the Minas Passage with respect to average power output for different hypothetical scenarios.

Figure 4.26 shows the changes in RMS current velocity with respect to average power output for scenarios at site A. This figure shows that the linear relationship between power output and hydrodynamic impacts is virtually identical for both the offshore lagoons and coastal lagoons. The diamond and circular symbols represent coastal and offshore tidal lagoons, respectively. The relationships are given as follows:

$$\Delta V_{RMS} = -0.0263 \cdot P_{avg} + 0.5069 \quad \text{for coastal tidal lagoons} \tag{4.31}$$

$$\Delta V_{RMS} = -0.0309 \cdot P_{avg} + 0.5587 \quad \text{for offshore tidal lagoons} \tag{4.32}$$

where ΔV_{RMS} is the change in RMS current velocity (cm/s), and P_{avg} is the average power output (MW).

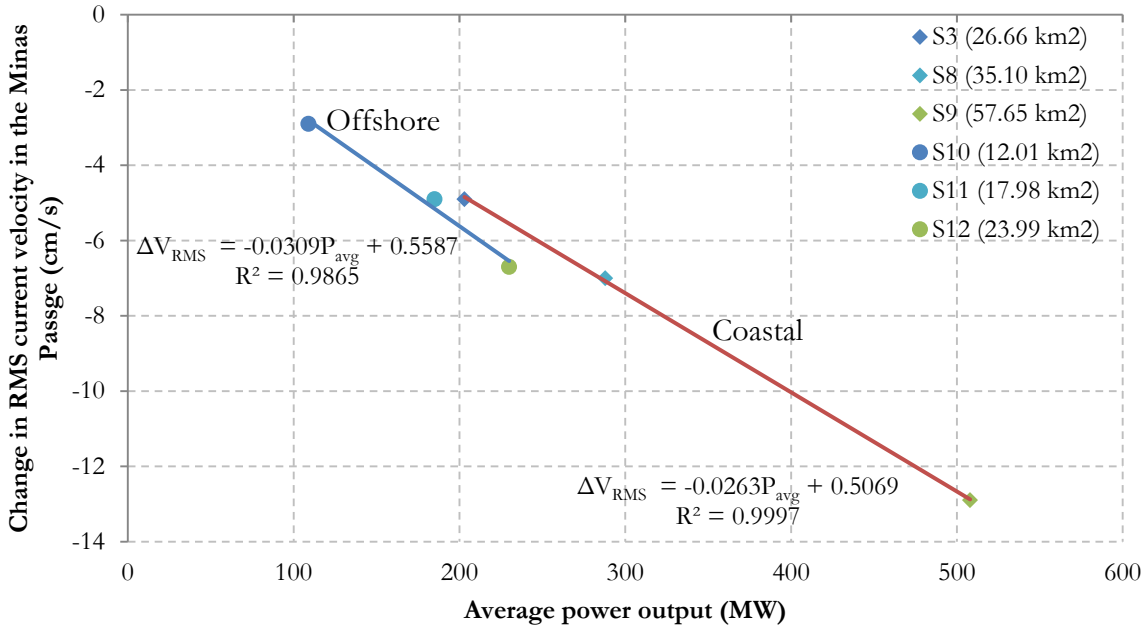

Figure 4.26: Changes in maximum tidal range with respect to average power output in the Minas Passage.

Chapter 5

Discussion

5.1 Introduction

In this chapter, the developments and findings of preceding chapters are discussed in order to provide a solid understanding of the hydrodynamic impacts induced by the presence of tidal lagoons proposed to be installed in the Bay of Fundy. The discussion focuses on analysing the technical design of tidal lagoons and the numerical model development, and provides also a discussion on the hydrodynamic results.

5.2 Technical Design of Tidal Lagoons and Model Development

5.2.1 Site selection

Delta Marine Consultants (DMC) (2007), commissioned by Tidal Electric Canada, performed a conceptual design study for a tidal lagoon in the Minas Basin. DMC proposed constructing a tidal lagoon on the tidal flats along the northern shore of Minas Basin between Five Islands and Economy Point. In this study, it was concluded that performing an analysis of the impact in the presence of other tidal lagoons designs was essential in order to identify the extent of possible changes over a wide range of constructions scenarios in the Bay of Fundy. Five other sites were selected in the Upper Bay of Fundy to implement hypothetical tidal lagoons. In this study, the sites were selected based on favourable bathymetry and available tidal range. Although the selection of a site could (and should) also be based on many factors such as geological properties, cost, material availability, environmental impacts and others this was not within the scope of this exploratory investigation. The purpose was to determine reasonable sites, well distributed in the Upper Bay of Fundy, and to study the general hydrodynamic impacts induced by the presence of tidal lagoons in the Bay of Fundy and the Gulf of Maine.

5.2.2 Tidal lagoon layout

The selection of a tidal lagoon layout is an iterative process that takes into account its potential capacity and efficiency, as well as its hydro-environmental impacts. Various lagoon layouts were investigated by DMC, including lagoons with single and multiple basins with a direct and rectified flow through the power station. DMC concluded that a single basin with a direct flow through the power station would be most cost efficient in the Minas Basin. In this study, it was assumed that a single basin with a direct flow would also be cost efficient in the Minas Basin and the Chignecto Bay. In order to ratify this assumption, further studies on tidal lagoon layouts would need to be undertaken.

Both types of tidal lagoon, coastal and offshore type, were placed at each site to analyse the difference between their hydrodynamic impacts. The impoundment layouts of the coastal tidal lagoon varied from site to site. However, the impoundment layouts of the offshore tidal lagoon were always circular for every site.

5.2.3 Sluices

Sluices are important features of tidal lagoon since they maximize the capacity of the power plant. Falconer et al. (2009) and Xia et al. (2010a, 2010b, 2010c) applied the orifice equation to simulate adequately the hydrodynamic processes caused by the sluices. Although this method is computationally efficient, it is only valid if the sluices behave like an orifice. In the study performed by DMC, they proposed positioning the sluices near the water level where the orifice relationship is no longer applicable. For computational time cost purposes, sluices were positioned at a certain depth in order to apply the orifice equation. The sluice's rectangular cross-sectional area was selected based on the study performed by DMC. A sensitivity analysis on the C_d parameter for each operating mode should be considered in future studies to understand its importance towards power generation.

5.2.4 Turbines and generators

The turbine performance chart was developed based upon the studies performed by Baker (1991) and Delta Marine Consultants (DMC) (2007). However, the performance of a turbine is often defined as a hill chart, relating specific discharge, unit speed, and efficiency in which they are based largely on physical and computational fluid dynamics models. Future studies should approach manufacturers directly to assess the most appropriate design for turbines and generators depending on the site characteristics in the Bay of Fundy.

5.2.5 Plant configuration

In the relatively limited previous studies, information on determining the plant configuration of a tidal lagoon was either limited or simply absent. In this study, a box model was developed to optimize the number of sluices and turbines maximum power generation for three different operation modes. The operation modes include the two-way generation, ebb generation, and flood generation. The model provides a good preliminary realistic description of the water level variations inside the tidal basin, available head differences at various times within the operation cycle, time varying discharge of turbines and sluices, and resulting available energy generation. Flow processes inside the basin and leakage through the impoundment are neglected in the present model as these aspects could be considered in future studies.

5.2.6 Power generation and the scale of lagoon development

The power generation was calculated and compared to the scale of lagoon development. In the Minas Basin, the power generation was found to be linearly related to the impoundment area for both types of tidal lagoons: coastal and offshore. Results also show that the offshore tidal lagoons require less impoundment area compared to the coastal tidal lagoons for equal amount of power generation. This is natural since offshore tidal lagoons are place deeper in the ocean and requires less area to obtain the same volume in a flatter coastal impoundment.

5.2.7 Operation protocol

The three operating modes such as two-way generation, and ebb generation produce similar power generation from the box model and from the hydrodynamic model. The output of electrical energy from the mode of flood generation was only about 65% of that obtained using the two-way generation and ebb generation. Although the two-way generation needs turbines to generate power at both ebb and flood tide, it produces equivalently more power generation output from the mode of ebb generation. In addition, there are two periods of power generation per tidal cycle instead of one, and thus power generation is much constantly added to the local grid. Menint (1986) has shown from the experience at La Rance tidal power plant in France that two-way generation produces less energy overall compared with ebb generation due to inherent turbine inefficiencies. Although modern turbine technology is thought to overcome it, the modes of ebb generation and two-way generation are considered to be virtually comparable in terms of power production.

5.3 Hydrodynamic Analysis

5.3.1 Tides

5.3.1.1 Near- and far-field

Results indicate that the scale of the changes in tidal hydrodynamics increases with larger lagoon development. While multiple lagoons or larger lagoons located in the Upper Bay of Fundy will generate more electrical power, they also induce larger perturbations to a near resonant system, and can therefore be expected to induce more significant changes in tidal hydrodynamics. Further investigation on the potential impact on communities and ecosystems must be taking into consideration.

5.3.1.2 Local changes

Results indicate that tidal lagoons will generally decrease tidal range in the vicinity of the tidal lagoon. These changes are most noticeable when tidal lagoons are implemented in Chignecto Bay. By far, the largest changes in tidal range occur within the lagoon itself, where tidal range is reduced by several meters, relative to existing conditions. The exact tidal range reduction will depend on the operation schemes and the characteristics of turbines and sluices. This change could cause an adverse impact on the ecological systems of local mudflats, which warrant further investigation.

5.3.2 Tidal currents

5.3.2.1 Near- and far-field changes

Tidal currents in remote locations such as the lower Bay of Fundy and Gulf of Maine will remain virtually unchanged. However, depending on the scale of lagoon development, tidal currents will noticeably be reduced at the mouth of Minas Basin and particularly in Minas Passage. This decrease in velocity could lead to reduction in suspended sediment concentrations and turbidity levels. Positive and negative impact associated with the environmental and ecological aspects require further investigations.

5.3.2.2 Local changes

A tidal lagoon will induce local changes in the direction and strength of the tidal currents, both within the lagoon and outside it. These changes are particularly important near the powerhouse and along the external perimeter of the impoundment dike. During the flood phase, seawater flows into the lagoon mainly through the turbines (some water flows through the sluices near the end of the flood stage). Within the lagoon, velocities are highest near the powerhouse, and de-

crease with increasing distance away from the powerhouse. Outside the lagoon, as expected, relatively strong currents occur near the powerhouse and along the perimeter of the impoundment dyke. During the ebb phase, seawater flows out of the lagoon mainly through the turbines, although some water passes through the sluices near low water. The peak velocities near the powerhouse tend to be larger during the ebb than during the flood, due to the shallower water depths outside the lagoon near the end of the ebb phase. Depending on seabed conditions, scour protection may be required in these areas to mitigate potential erosion due to the high energy flows emerging from the turbines and sluices. Scour protection may also be required to stabilize and protect the toe of the impoundment dike. There are also areas in tidal lagoon where speeds are reduced significantly. It is possible that fine sediments may accumulate in this area because of these lower velocities. Increased sedimentation is obviously undesirable, as this may cause the lagoon to silt up over time. If significant sediment deposition occurs, some intervention may be required to either prevent sediment from settling, or remove the sediment after it has deposited.

5.3.3 Influence of lagoon operation protocol

Results indicate that each operation mode will have a different influence on the hydrodynamics of the affected areas. For the three power generation modes (two-way, ebb, flood), tidal ranges and the tidal currents were predicted to be very similar near- and far-field. The change in tidal range and velocities due to different operation mode were predicted to be dissimilar near the powerhouse and inside the tidal lagoon impoundment. The operating mode of two-way generation may have a relatively small impact on the loss of intertidal habitats, but would also have some significant environmental impacts in terms of reduced water body exchange and changes to some marshes. Due to the nature of the operation of the ebb generation, there's excessive lowering of the maximum water level in the tidal lagoon's impoundment. This would minimize the loss of intertidal zones, and may cause adverse impacts on the aquatic environment considerably. As expected, the non-power operational protocol, opened-gates, has the least amount of hydrodynamic impacts since the hydrodynamic processes are similar to natural flow condition. However, the other non-power operational protocol, closed-gates, has the largest hydrodynamic impact towards the change in tidal range and tidal currents.

Chapter 6

Conclusions

Presently, there is considerable interest in constructing tidal lagoons in the Bay of Fundy to extract potential energy from tides. Although there have been studies on the technical aspects of tidal lagoons, the potential hydrodynamic impacts due to this new technology have not been investigated. The aim of this study was to develop a numerical model and attempt to partially understand the impacts on tidal hydrodynamics throughout the Gulf of Maine and the Bay of Fundy due to the presence and operation of man-made tidal lagoons implemented the Upper Bay of Fundy.

A detailed two-dimensional (depth-averaged) hydrodynamic model has been developed and applied to investigate the changes in water levels and tidal currents for various hypothetical lagoon development scenarios. The model was successfully calibrated and validated against water level observations for many tidal stations throughout the region, and can be used to predict tidal hydrodynamics with good accuracy. Lagoons are simulated by partitioning the model domain into sub-domains, and using source-sink pairs to simulate the exchange of seawater through sluices and turbines. This modeling approach is able to provide a reasonable simulation of the hydrodynamic processes at man-made tidal power lagoons.

The model was subsequently applied to predict tidal hydrodynamics for present conditions without lagoons, and for 19 different hypothetical scenarios with from one to six individual lagoons. The numerical results indicate that any tidal power lagoon will induce some large changes in the pattern and strength of the local tidal currents, particularly near the powerhouse and possibly along portions of the impoundment dyke. Numerical results indicate that the changes in water levels and tidal current velocities are largest near the lagoons and generally diminish with increasing distance. Notably, however, some change is predicted throughout the entire Gulf of Maine, even for the smallest development scenario. In addition, the scale of the hydrodynamic change is also found to be proportional to the scale of the lagoon development, with multiple lagoons inducing larger change. While the changes may represent a small fraction of the tidal range, their potential impact on communities and ecosystems warrants further investigation and

careful consideration. Hence, without further study, it is difficult to comment at this point in time on whether the potential benefits of tidal power lagoons might outweigh the drawbacks associated with these changes in tidal hydrodynamics.

In terms of power output for the different operating modes, the mode of flood generation produced the least electricity among the three power generation modes considered and two-way and ebb generation produced similar levels of power output. The operating modes were found to have some influence on local velocities, particularly within the lagoon. However, the operational protocol appears to have little influence on the scale of far-field impacts. Therefore, the modes of ebb generation and two-way generation were considered to be virtually comparable in terms of overall advantages and disadvantages, particularly when trying to balance uniformity of power production and hydrodynamic impact.

A future direction for this research is to investigate the implications of the velocity changes on sediment transport and on the associated morphodynamics of the seabed near and within a lagoon. The new numerical model can also be applied to simulate and assess the hydrodynamic impacts of other tidal energy developments, including tidal barrages and arrays of in-stream turbines.

Chapter 7

References

Allard, T. 2004. Ontario Fishing Newsletter:Staying Current on River Walleye, Ontario Walleye Fishing.

Baker, A. C. 1991. *Tidal Power.*, Peter Peregrinus Ltd., London, United Kingdom.

Bay of Fundy Tidal Power Review Board. 1974. Preliminary Reassessment of Feasibility of Tidal Power Development in the Bay of Fundy.

Bay of Fundy Tidal Power Review Board. 1977. Reassessment of Fundy Tidal Power. Ottawa, Report prepared for the Minister of Supply and Services (Canada), under contract No. 02KX 23384-5207.

Chow, V. T. 1959. *Open-Channel Hydraulics.*, McGraw-Hill, Inc.

Cornett, A. 2006. Inventory of Canada's Renewable Marine Energy Resources. Canadian Hydraulics Centre, NRC, Report CHC-TR-041.

Cornett, A., Durand, N., and Serrer, M. 2010. 3-D Modelling and assessment of tidal current resources in the Bay of Fundy. *International Conference on Ocean Energy*, 3.

Delta Marine Consultants (DMC). 2007. Tidal Power Plant, Bay of Fundy. Technical Feasibility Study.

Delta Marine Consultants. 2007. Tidal Power Plant, Bay of Fundy. Technical Feasibility Study.

DeWolfe, D. L. 1986. An update on the effects of tidal power development on the tidal regime of the Bay of Fundy and Gulf of Maine. *Effects of changes in sea level and tidal range on the Gulf of Maine-Bay of Fundy system*, 35-54.

Dupont, F. and Hannah, C. G. G. D. A. 2005. Modelling the Sea Level of the Upper Bay of Fundy. *Atmosphere-Ocean*, 43(1):33-47.

Durand, N., Cornett, A., and Bourban, S. 2008. 3-D modelling and assessment of tidal current energy resources in the Bay of Fundy. Canadian Hydraulic Centre, NRC, Ottawa, Report CHC-TR-052.

Falconer, R., Xia, J., Lin, B., and Ahmadian, R. 2009. The Severn barrage and other tidal energy options:Hydrodynamic and power output modelling. *Sci China Ser E-Tech Sci*, 52(11):3413-3424.

Garrett, C. 1972. Tidal resonance in the Bay of Fundy and Gulf of Maine. *Nature*, 238:441-443.

Garrett, C. 1974. Normal modes of the Bay of Fundy and Gulf of Maine. *Journal of Earth Science*, 11:549-556.

Gordon, D. C. and Longhurst, A. R. 1979. The Environmental Aspects of a Tidal Power Project in the Upper Reaches of the Bay of Fundy. *Marine Pollution Bulletin*, 10(38):38-45.

Greenberg, D. A. 1977. Mathematical studies of tidal behaviour in the Bay of Fundy. Department of Fisheries, Ottawa, Report No. 46.

Greenberg, D. A. 1979. A numerical model investigation of tidal phenomena in the Bay of Fundy and Gulf of Maine. *Marine Geodesy*, 2(2):161-187.

Greenberg, D. A. 1983. Modeling the mean barotropic circulation in the Bay of Fundy and Gulf of Maine. *Journal of Physical Oceanography*, 13:886-904.

Greenberg, D., Shore, J., and Shen, Y. 1997. Modelling tidal flows in Passamaquoddy Bay. *Proceedings of the Maritime Atlantic Ecozone Science Workshop*, 58-64.

Hagerman, G., Fader, G., Carlin, G., and Bedard, R. 2006. EPRI Nova Scotia in-stream energy conversion survey and characterization of potential project sites.

Hagerman, G., Fader, G., Carlin, G., and Bedard, R. 2006. EPRI Nova Scotia tidal in-stream energy conversion survey and characterization of potential project sites.

Henderson, F. M. 1966. *Open Channel Flow*., McMillan Company, New York, USA.

Hervouet, J. M. 2007. Hydrodynamics of free-surface flows - modelling with the finite element method.

Karsten, R. H., McMillan, J. M., Lickley, M. J., and Haynes, R. D. 2008. Assessment of tidal current energy in the Minas Passage, Bay of Fundy. *Proc. IMechE*, 222(Part A: Journal of Power and Energy):493-507.

Lawton, F. L. 1970. Economics of Tidal Power. *Proceedings of an international Conference on the Utilization of Tidal Power*, 105-129.

Lynch, D. R. and Naimie, C. R. 1993. The M2 tide and its residual on the outer banks of the Gulf of Maine. *Journal of Physical Oceanography*, 23(10):2222-2253.

Menint, L. 1986. The new design of bulb turbine units based on the experience from the Rance tidal station and on-the-river build units. *Proceedings of 3rd international symposium on wave, Tidal, OTEC and small scale hydro energy. BHRA.*

Normann, J. M. 1985. Hydraulic design of highway culverts. HDS-5 (Hydraulic Design Series 5). FHWA-IP-85-15. NTIS publication PB86196961.

Rao, D. B. 1968. Natural Oscillations of the Bay of Fundy. *Journal of the Fisheries Research Board of Canada*, 25(6):1097-1114.

Sankaranarayanan, S. and McCay, D. F. 2003. Three-Dimensional Modeling of Tidal Circulation in Bay of Fundy. *Journal of Waterway, Port, Coastal and Ocean Engineering*, 129(3):114-123.

Severn Barrage Committee (SBC). 1981. Tidal Power from the Severn Estuary. HMSO.

Severn Tidal Power Group (STPG). 1993. Severn Barrage project: further environmental and energy capture studies. ETSU report (TID 4099).

Smagorinsky, J. 1963. General circulation experiments with the primitive equations I: the basic experiment. *Mon. Weather Rev.*, 91:99-164.

Sucsy, P. V., Pearce, B. R., and G, P. V. 1992. Comparison of Two- and Three-Dimensional Model Simulation of the Effect of a Tidal Barrier on the Gulf of Maine Tides. *Journal of Physical Oceanography*, 23:1231-1248.

Sutherland, G., Foreman, M., and Garrett, C. 2007. Tidal current energy assessment for Johnstone Strait, Vancouver Island. *Journal of Power and Energy*, 338(221).

Xia, J., Falconer, R. A., and Lin, B. 2010a. Hydrodynamic impact of a tidal barrage in the Severn Estuary, UK. *Renewable Energy*, 35:1455-1468.

Xia, J., Falconer, R. A., and Lin, B. 2010b. Impact of different operating modes for a Severn Barrage on the tidal power and flood inundation in the Severn Estuary, UK. *Applied Energy*, 87:2374-2391.

Xia, J., Falconer, R. A., and Lin, B. 2010c. Impact of different tidal renewable energy projects on the hydrodynamic processes in the Severn Estuary, UK. *Ocean Modelling*, 32:86-104.

Zhang, A., Wei, E., and Parker, B. B. 2003. Optional estimation of tidal open boundary conditions using predicted tides and adjoint data assimilation technique. *Conf. Shelf Res.*, 1055-1070.

APPENDICES

Annexe A

Tides

A.1 Introduction

The aim of this section is to provide a brief explanation on the aspects of tides and tidal constituents.

A.2 Origin of tides

Tides represent the periodic rise and fall of sea levels caused by the combined effects of celestial gravitational and centrifugal forces. These effects are the gravitational attraction of the Earth, the centrifugal force generated by the rotation of the Earth, the gravitational attraction of the Moon, and the gravitational attraction of the Sun.

If the gravitation attraction of the Sun was neglected and the Earth was completely covered by a very deep ocean, the gravitational force of the Moon would produce two bulges. One bulge would be produce on the side facing the Moon and the other one on the opposite side of the Earth. Figure A.1 shows the Earth and Moon as viewed from above the North Pole. An observer under the water on the Earth at position 1 is beneath one of the water bulges and would be experiencing a high tide. A quarter of a revolution later, at position 2 where the original water level has been depressed, a low tide would be seen. The high-low tide sequence repeats as the observer moves around through points 3 and 4.

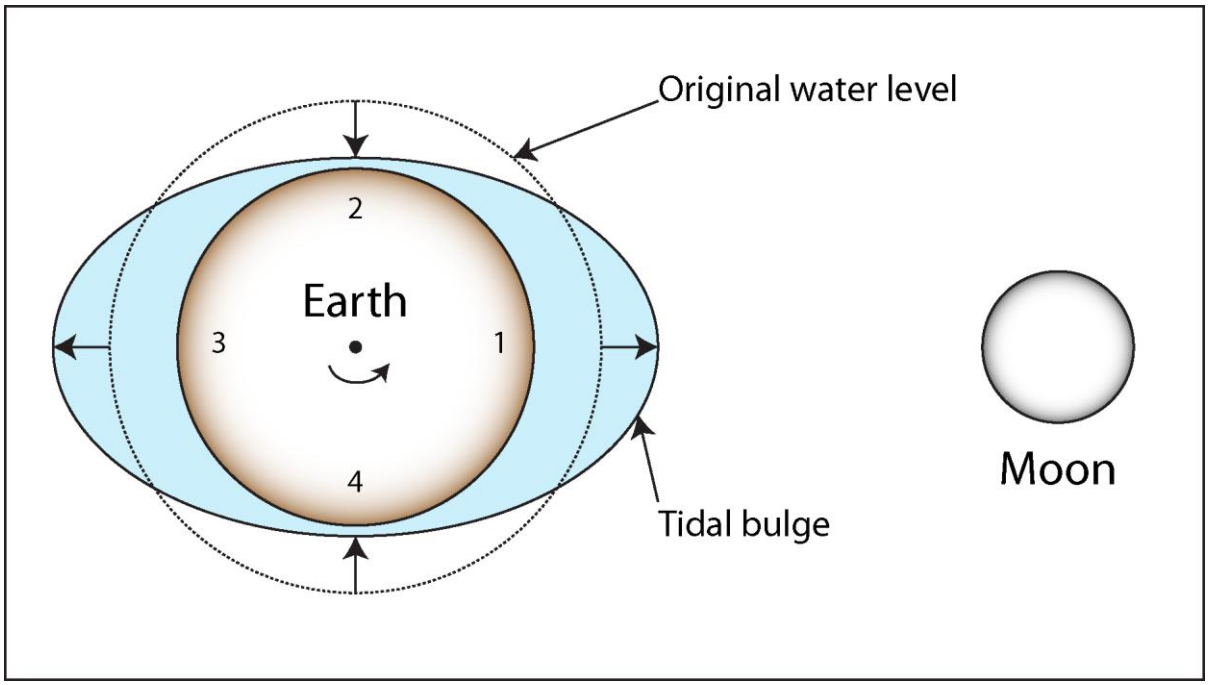

Figure A.1: Tidal bulges.

The Earth-Sun system is also subject to similar gravitational and centrifugal forces but due to the Sun's greater distance this system has less than half the strength of the lunar-related forces. Consequently, the solar-related residual forces and resulting bulges are correspondingly smaller.

When the Sun, Moon, and the Earth are lined up, the Sun and Moon are exerting their strongest force together and tidal ranges are at their maximum. This is known as spring tides. This occurs twice each month, when the Moon is full and new. At the first quarter and third quarter Moon, the Sun and Moon are at a 45° angle to each other, and their gravitational energy is diminished. The lower than normal tidal range that takes place at these times is called neap tides.

Another factor having a substantial influence on tidal ranges is the elliptical shape of the Moon's orbit. Since gravitational force is inversely proportional to the square of the distance, the Moon's tidal influence is 30 to 48% greater at perigee than at apogee.

Tides usually experience two high tides and two low tides each day (semi diurnal tide) and are most pronounced along the coastline of the oceans and in bays where the tidal range is increased due to secondary effects such as coastal geomorphology, coastal water depth, ocean floor topography and many more. All these secondary effects can be viewed as separate tide generators. Each tide generator has its own strength, frequency and phase angle with respect to the others.

The resulting tide is, therefore, a complex addition of effects of the moon, the sun and many secondary causes. Each component is called a tidal constituent.

A.3 Tidal constituents

The Earth's geography not only confines the water and moves it along with the surface of the Earth, but it also causes certain tidal constituents to resonate locally in the various oceans, seas, bays, and estuaries. Thus some constituents are magnified in certain locations, while others simply disappear, making the tide at each location unique.

The tide is assumed to be represented by the harmonic summation

$$\eta(t) = \sum_{i=1}^{I} a_i \cos(\omega_i t + \alpha_i) \tag{7.1}$$

where $\eta(t)$ is the sea water level at time t, a_i is the amplitudes, α_i is the phase angles of the tidal constituents and ω_i are their angular frequencies. For example, the semi-diurnal lunar constituent, identified as M2 has a period of 12.42 hours and therefore $\omega_{M2} = 2\pi/(3600 \times 12.42) = 1.405 \times 10^{-5}$ sec^{-1}. The period of important tidal constituents are shown in Table A.1. The amplitudes, a_i and phase angles, α_i of tidal constituents are determined from tidal analysis. Tidal analysis consists of separating measured tides into as many of its constituents as can be identified from the length of record available.

Among all the tidal components, M2, S2, and K1 are the most significant, since the amplitudes of these three tide components are usually greatest and dominate the observed tides.

Table A.1: Important tidal constituants.

Semi-diurnal		**Diurnal**		**Long term**	
Tidal constituent	Period	Tidal constituent	Period	Tidal constituent	Period
M2	12.421 hr	K1	23.934 hr	Mf	13.661 days
S2	12.000 hr	O1	25.819 hr	Mm	27.555 days
N2	12.658 hr	P1	24.066 hr	Lunar node	18.613 yr
K2	11.967 hr	S1	24.000 hr	Sa	1.000 yr

Annexe B

Model Development

B.1 Depth / Elevation

The objective of this section is to describe the sources of different topographic and bathymetric data and how data were integrated.

B.1.1 Raw Data

Topographic and bathymetric data were obtained from six sources (see Figure A.2): (1) Geobase Canadian Digital Elevation Data, (2) USGS National Elevation Dataset, (3) CHS Multibeam Bathymetry, (4) CHS Nautical Charts, (5) NOAA Soundings and Electronic Navigational Charts Bathymetry, and (6) BODC Gridded Bathymetric Chart of the Oceans.

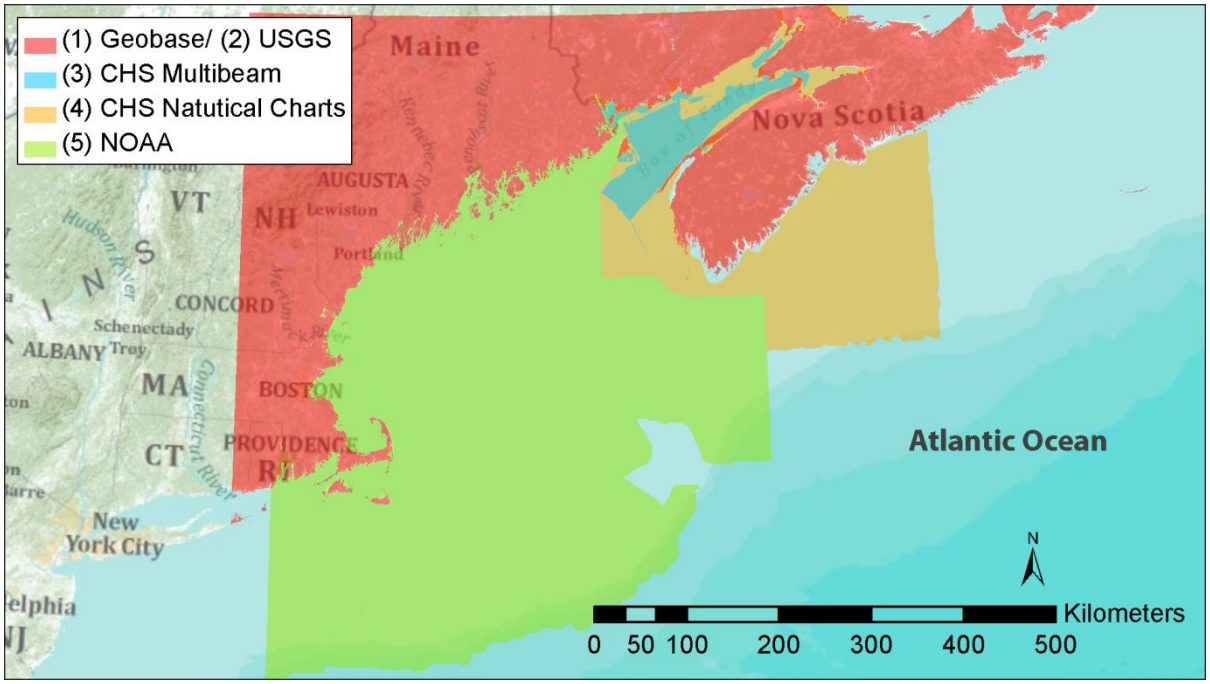

Figure A.2: Topographic and bathymetric data.

(1) Geobase Canadian Digital Elevation Data

GeoBase is a federal, provincial and territorial government initiative that is overseen by the Canadian Council on Geomatics (CCOG). Depending on the latitude of the Canadian Digital Elevation Data section, the grid spacing, based on geographic coordinates, vary in resolution from a minimum of 0.75 arc seconds to a maximum 3 arc seconds for the 1:50,000 NTS tiles, and from

a minimum of 3 arc seconds to a maximum 12 arc seconds for the 1:250,000 NTS tiles respectively. Ground Elevations are recorded in metres relative to Mean Sea Level (MSL), based on the North American Datum 1983 (NAD83) horizontal reference datum. All digital elevation maps (DEMs) were obtained from http://www.geobase.ca.

(2) USGS National Elevation Dataset

The National Elevation Dataset (NED) 1 Arc Second is a raster product assembled by the U.S. Geological Survey (USGS). NED is designed to provide National elevation data in a seamless form with a consistent datum, elevation unit, and projection. NED has a resolution of one arc-second (approximately 30 meters) for the conterminous United States. All NED were obtained from http://seamless.usgs.gov.

(3) CHS Multibeam Bathymetry

The Canadian Hydrographic Service (CHS) in collaboration with Natural Resources Canada (NRCan) perform a continued multibeam mapping of the floor and water column of the Bay of Fundy(Author). The resulting scale map is approximately 1:50,000.

(4) CHS Nautical Charts

The Canadian Hydrographic Service CHS is a division of the Science Branch of the Department of Fisheries and Oceans Canada. CHS publishes and maintains nearly a thousand nautical charts as well as hundreds of publications. All data was obtained from CHS's nautical digital charts.

(5) NOAA Soundings and Electronic Navigational Charts Bathymetry

NOAA's National Geophysical Data Center (NGDC) provides scientific stewardship, products, and services for geophysical data. Bathymetric data was obtained from http://www.ngdc.noaa.gov/mgg/bathymetry/relief.html.

(6) BODC Gridded Bathymetric Chart of the Oceans

The British Oceanographic Data Center (BODC) has bathymetric and topographic data. BPOC provides a Gridded Bathymetric Chart of the Oceans (GEBCO) gridded bathymetry data sets. The GEBCO_08 Grid – global 30 arc-second grid was obtained from https://www.bodc.ac.uk.

B.1.2 Data integration

Bathymetric data points (3) CHS Multibeam Bathymetry, and (4) CHS Nautical Charts were interpolated using the spline interpolation method to obtain a raster image. It was integrated with the other raster images such as the (1) Geobase Canadian Digital Elevation Data, (2) USGS National Elevation Dataset, (5) NOAA Soundings and Electronic Navigational Charts Bathymetry,

and (6) BODC Gridded Bathymetric Chart of the Oceans. The highest spatial resolution was taken during the integration.

B.1.3 Analysis

Spatial resolution represents the level of detail in an image. A finer spatial resolution will show more details than a coarser resolution. An example is shown in Figure A.3. The figure shows four images with the same dimensions but with difference resolution. An image with 100x100 cells will show a lot more details than an image with 20x20 cells or even 10x10 cells. Table A.2 shows all the spatial resolution of each topographic and bathymetric dataset.

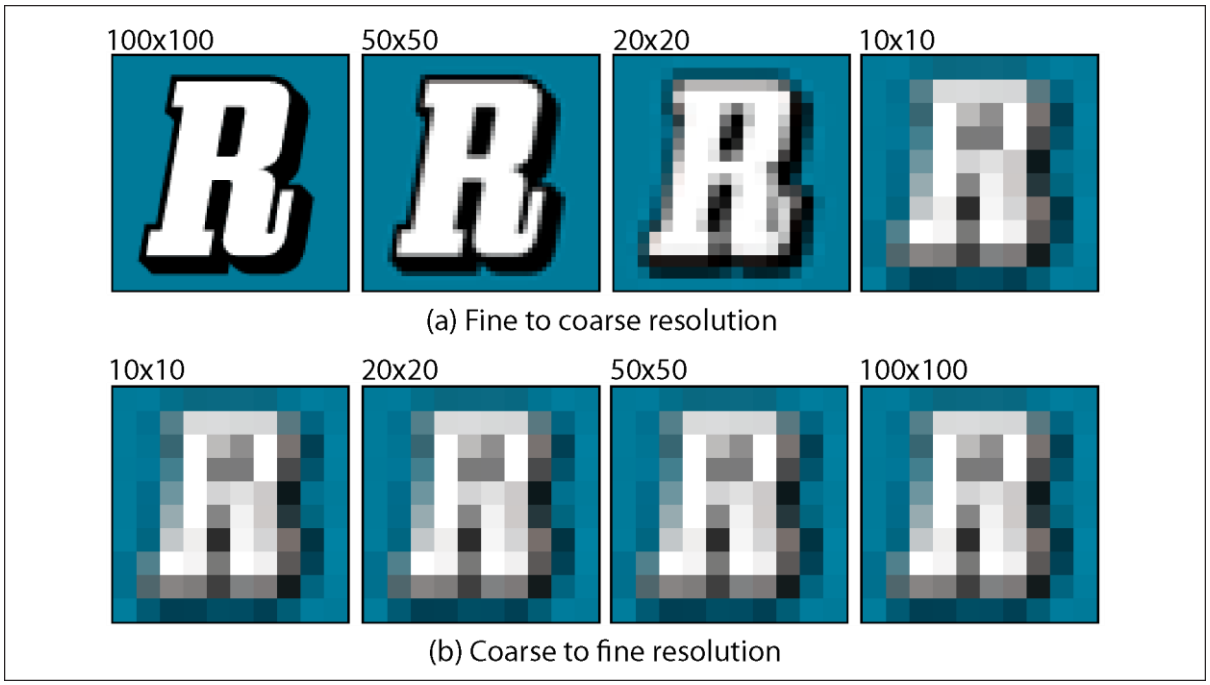

Figure A.3: Image re-sampling example.

Table A.2: Topographic and bathymetric dataset spatial resolution.

Data	Spatial resolution	
	(arc-second)	(meters)
GeoBase	0.5 - 3	~25
USGS	1	~25
CHS Multibeam	(-)	~100
CHS Nautical Charts	(-)	~500
NOAA	3	~100
BODC	30	~1000

Each spatial resolution dataset were re-sampled to the highest resolution of 25 m. Re-sampling a raster image is feasible but there's some limitation. A higher spatial resolution map can be resampled to a lower spatial resolution map as shown Figure A.3.a. A lower spatial resolution map can also be resample to a higher spatial resolution however; it won't generate a higher detailed map as shown in Figure A.3.b.

B.2 Model boundaries

Two types of boundaries were developed in the study: land and ocean boundary.

B.2.1 Land boundary

Land boundaries are shorelines along the coast and along the islands. Land boundaries were developed up to the highest astronomical tide (HAT) shoreline in areas of special interest to include inter-tidal flats. To reduce computational cost, inter-tidal flats were excluded in areas of lesser interest by developing the land boundaries up to the lowest astronomical tide (LAT).

The lowest tidal shoreline and the highest tidal shoreline are obtainable by comparing depth/elevation with LAT and HAT, respectively. The LAT and HAT were calculated from model results produced by a depth-integrated finite-element tidal circulation model develop by Dupont et al. (2005). The HAT and LAT in the BoF and GoM are shown in Figure A.4 and Figure A.5, respectively. For calculation simplicity, the shorelines were approximated to the nearest natural number.

B.2.2 Ocean boundary

Ocean boundaries are imaginary lines created to enclose the numerical model. The ocean boundaries were developed by determining the -1, 000m isoline along the continental shelf and by creating arbitrary lines to link to continental shelf isoline and the coastline.

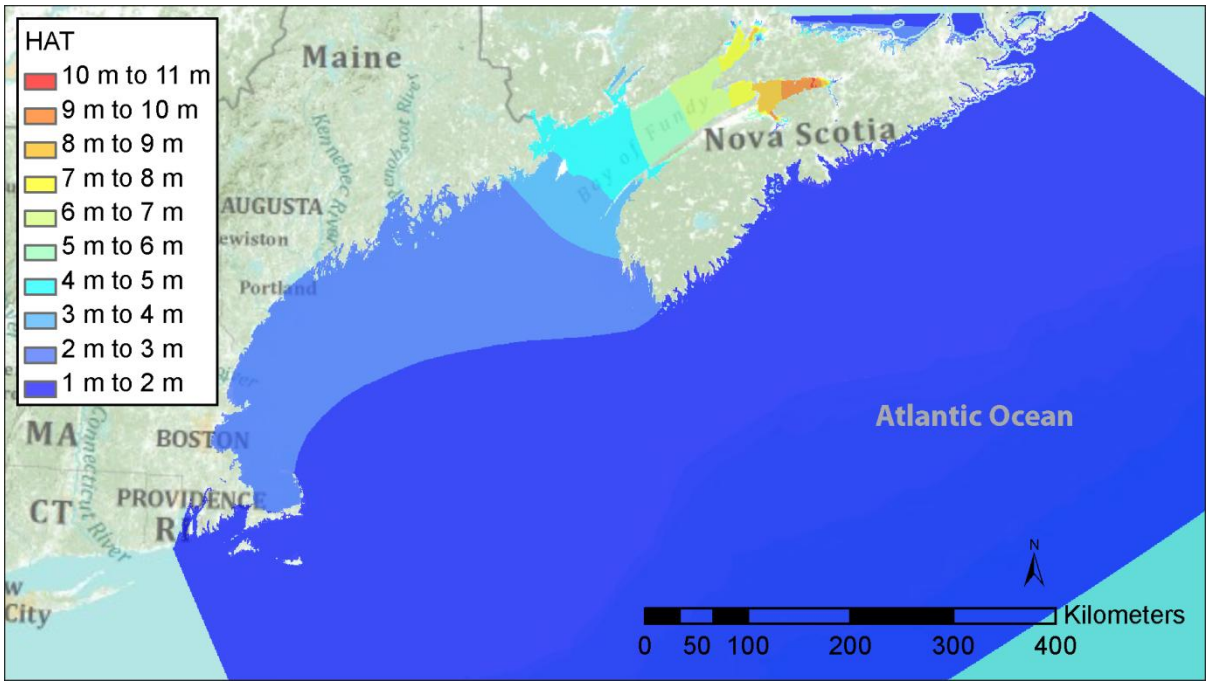

Figure A.4: Highest astronomical tide.

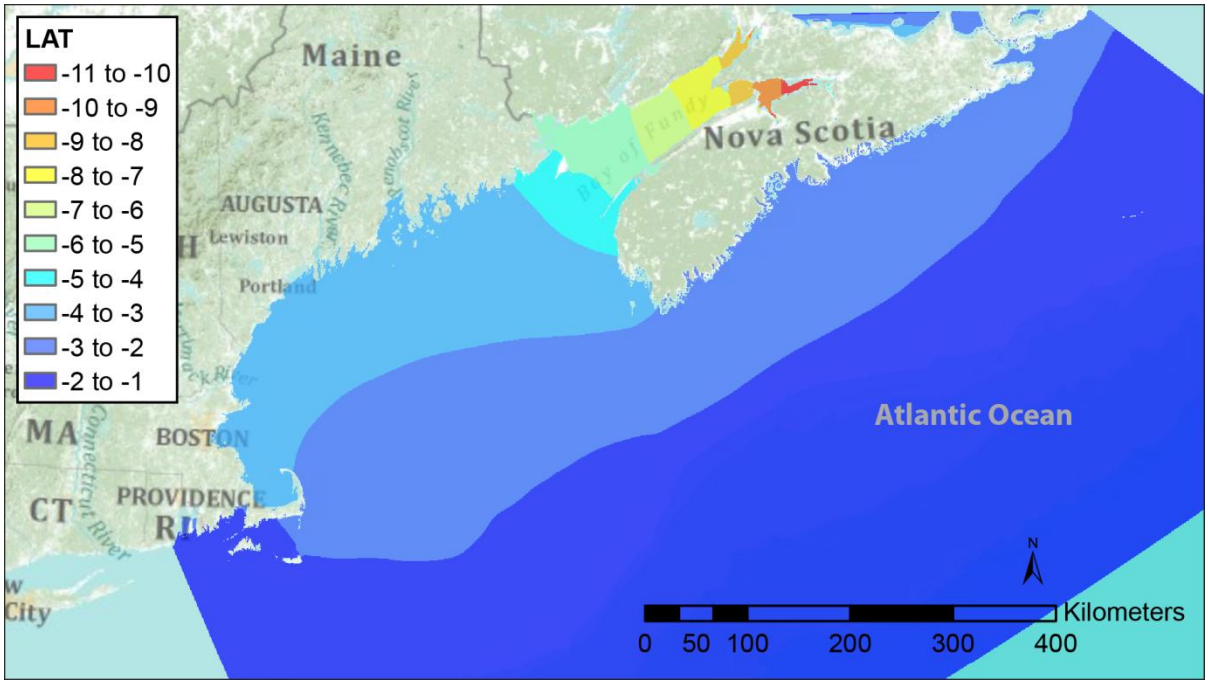

Figure A.5: Lowest astronomical tide.

B.3 Tidal lagoon grid model

Table A.3 summarizes each model grid scenario with different combination of tidal lagoon layouts. Figure A.6 to Figure A.10 shows each model grid layout used in this study.

Table A.3: Model grid layouts.

Simulation	Model grid layout	Number of coastal lagoon	Coastal lagoon layout	Number of offshore lagoon	Offshore lagoon layout
S1, S3, S4, S5, S6, S7	A_C1	1	A_C1	0	-
S8	A_C2	1	A_C2	0	-
S9	A_C3	1	A_C3	0	-
S2, S10	A_O1	0	-	1	A_O1
S11	A_O2	0	-	1	A_O2
S12	A_O3	0	-	1	A_O3
S13	B_C1	1	B_C1	0	-
S14	C_C1	1	C_C1	0	-
S15	m3_C1	3	A_C1 B_C1 C_C1	0	-
S16	m3_O1	0	-	3	A_O1 B_O1 C_O1
S17	m3_C2	3	D_C1 E_C1 F_C1	0	-
S18	m3_O2	0	-	3	D_O1 E_O1 F_O1
S19	m6_O1	0	-	6	A_O1 B_O1 C_O1 D_O1 E_O1 F_O1

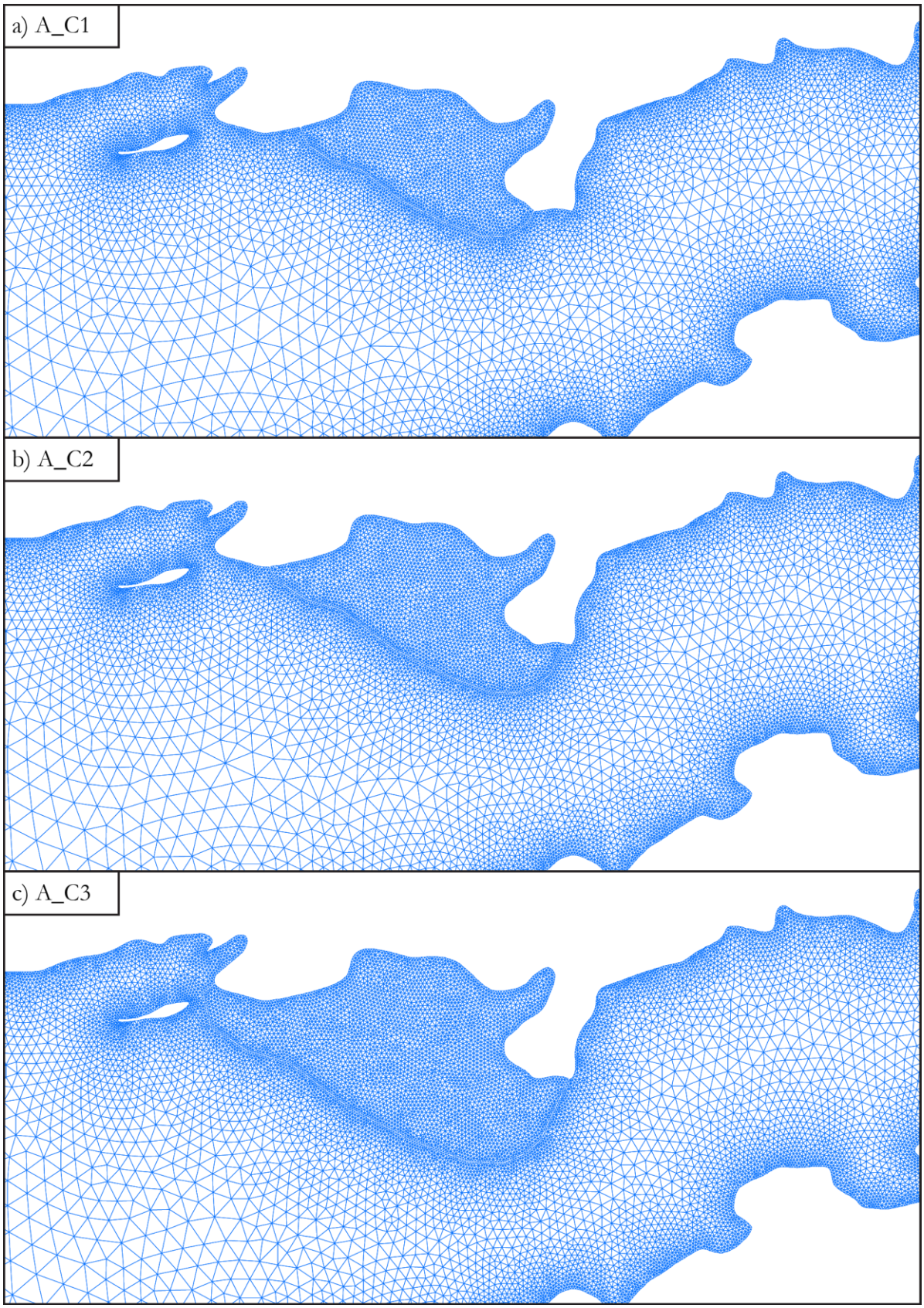

Figure A.6: Model grid of a) A_C1, b) A_C2, and c) A_C3.

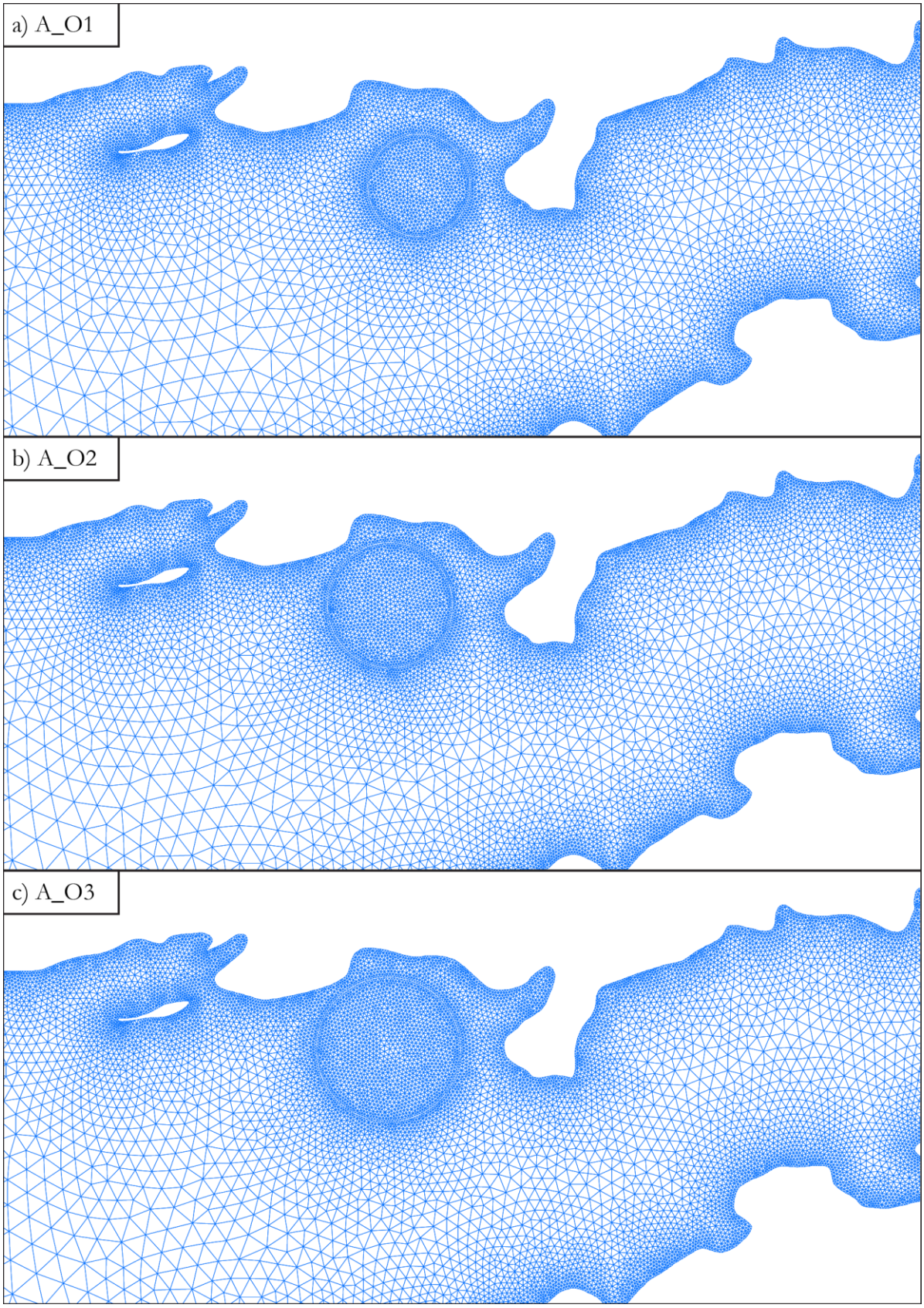

Figure A.7: Model grid of a) A_O1, b) A_O2, and c) A_O3.

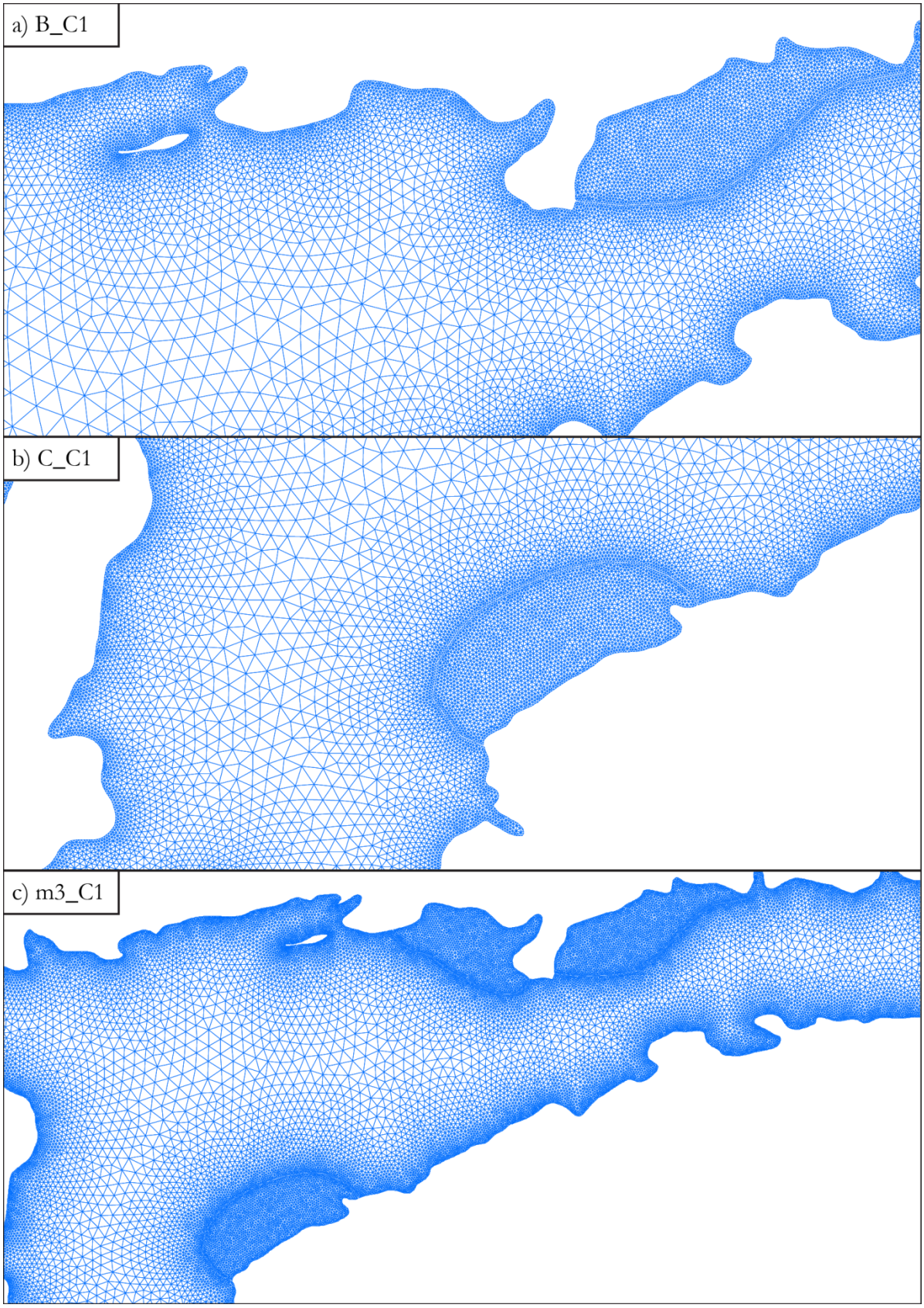

Figure A.8: Model grid of a) C_C1, b) C_C1, and c) m3_C1.

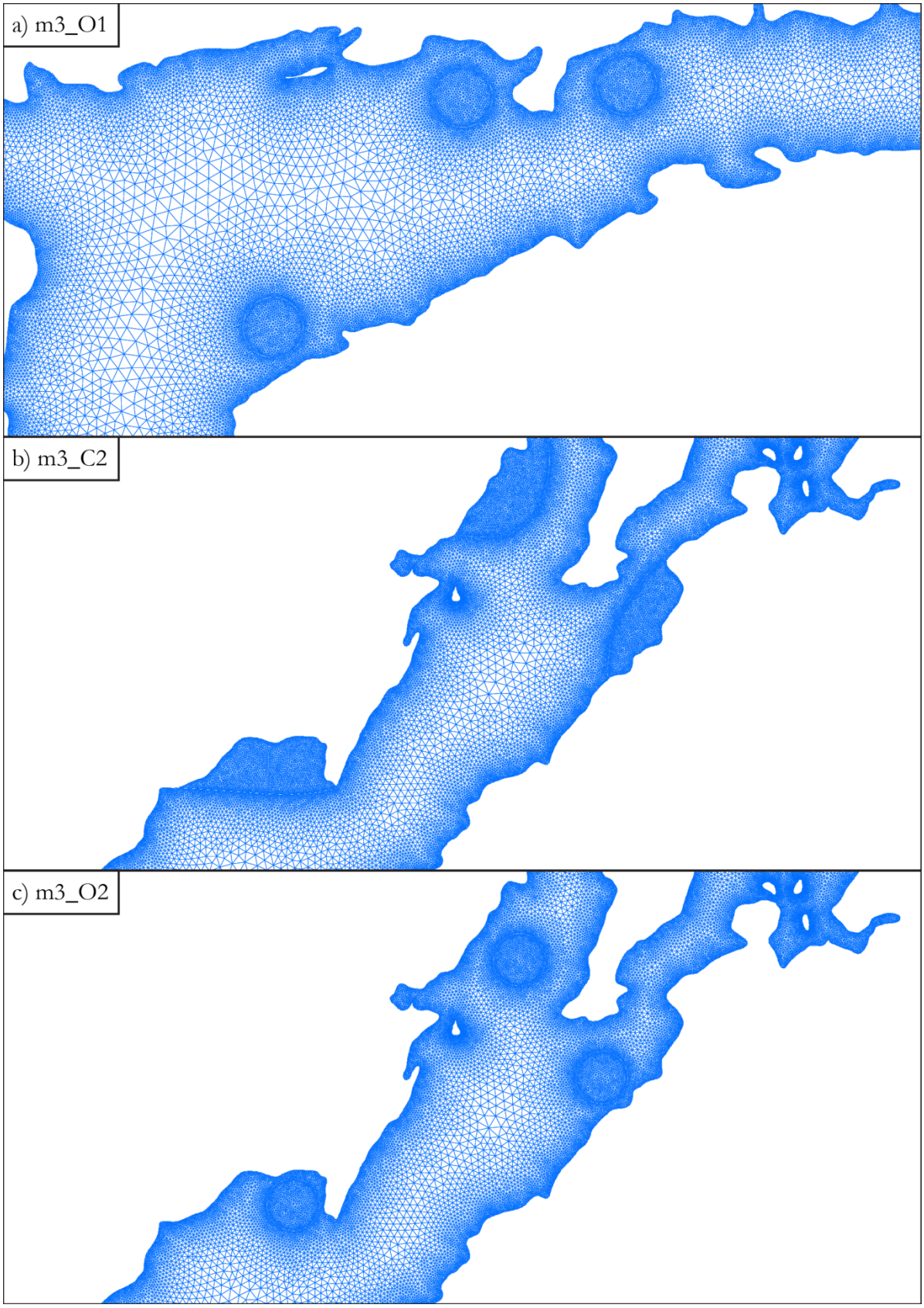

Figure A.9: Model grid of a) m3_O1, b) m3_C2, and c) m3_O2.

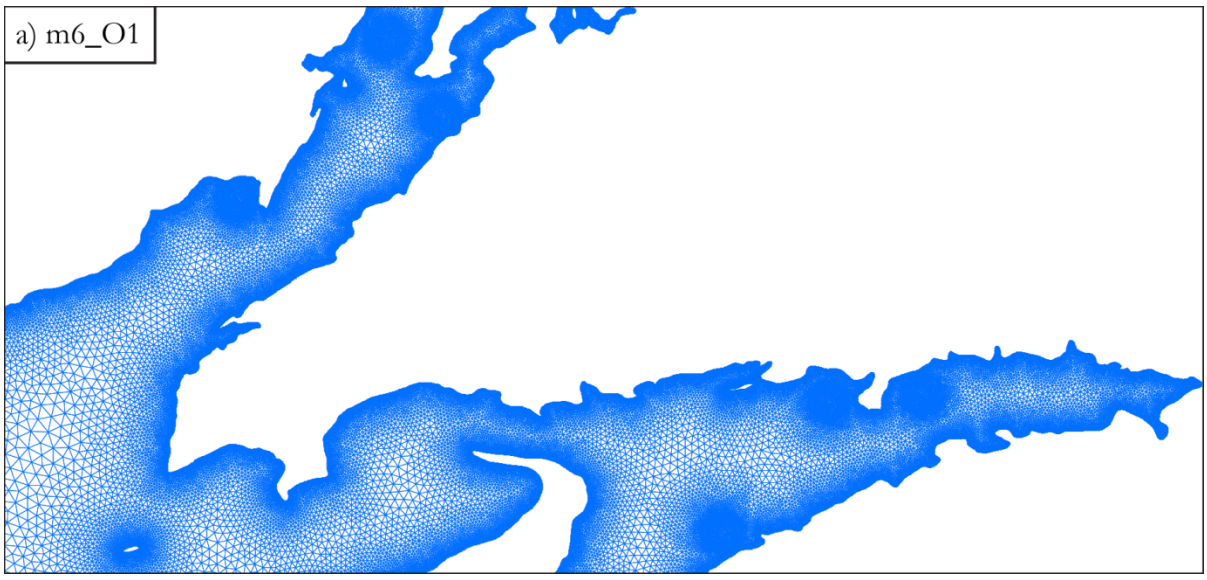

Figure A.10: Model grid of a) m6_O1.

Annexe C

Technical Design

C.1 Sluices

The water head-discharge relationships for a sluice were calculated for three invert elevation (-20 m, -16 m, -12 m) using the orifice equation and culvert equations. During this process, the sluice was assumed to have a circular cross-sectional area of 56 m^2 where tidal range fluctuated 16 m. A discharge coefficient of 0.75 was applied for the orifice equation.

Figure 3.5 shows the water head-discharge relationship for an invert elevation of -20 m. Figure A.11 and Figure A.12 shows the water head-discharge relationship for an invert elevation of -16 m and -12 m, respectively.

An application was developed to simulate adequately the hydrodynamic processes using the orifice equation and the culvert equations. The reproduction of the code required for the simulations presented in this study would take up far too much space and would be of limited interest to most readers. Those who are interested in the code may contact the author by e-mail (julien_cousineau@hotmail.com).

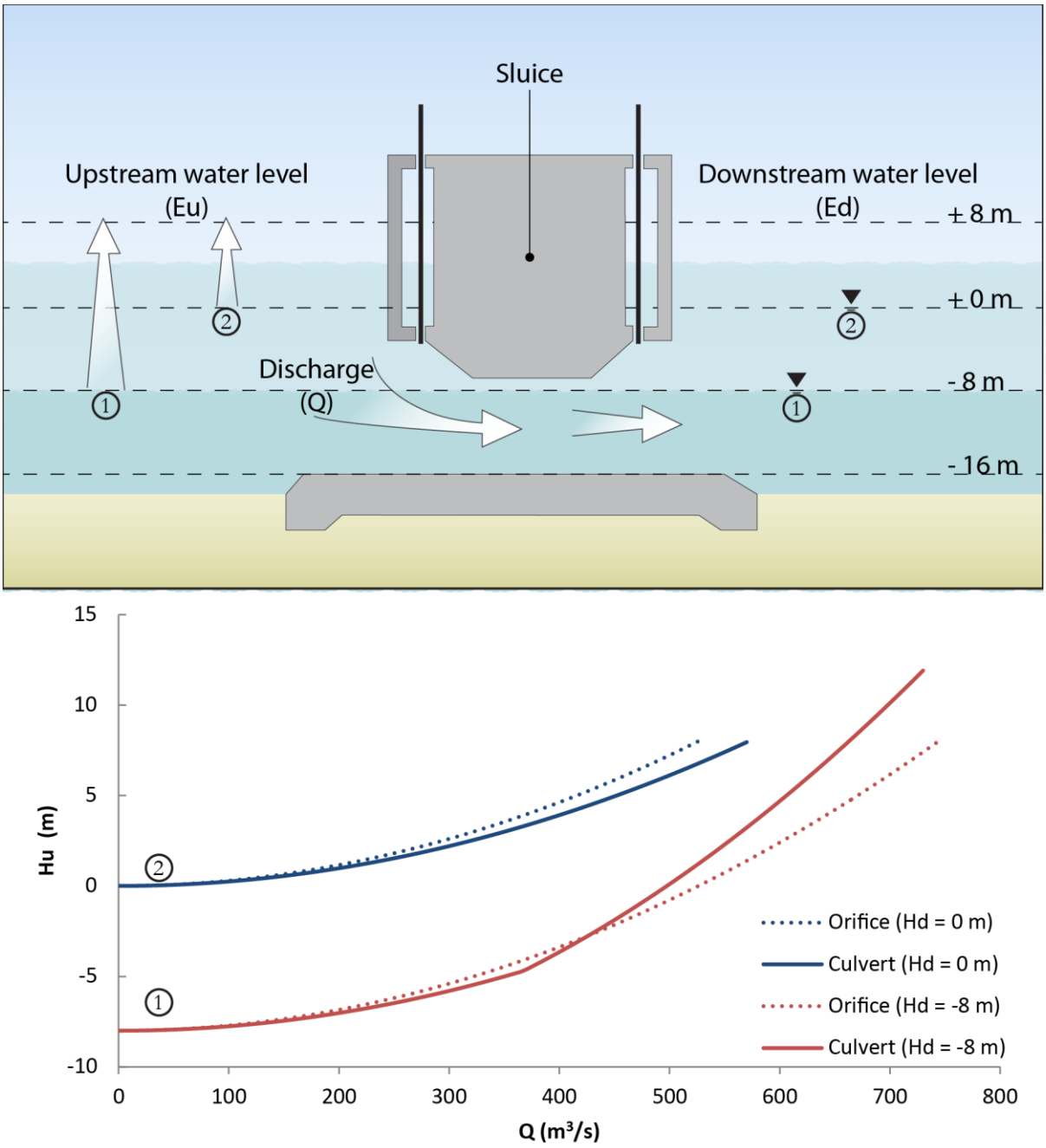

Figure A.11: Hydraulic processes of a sluice for an invert elevation of -16m.

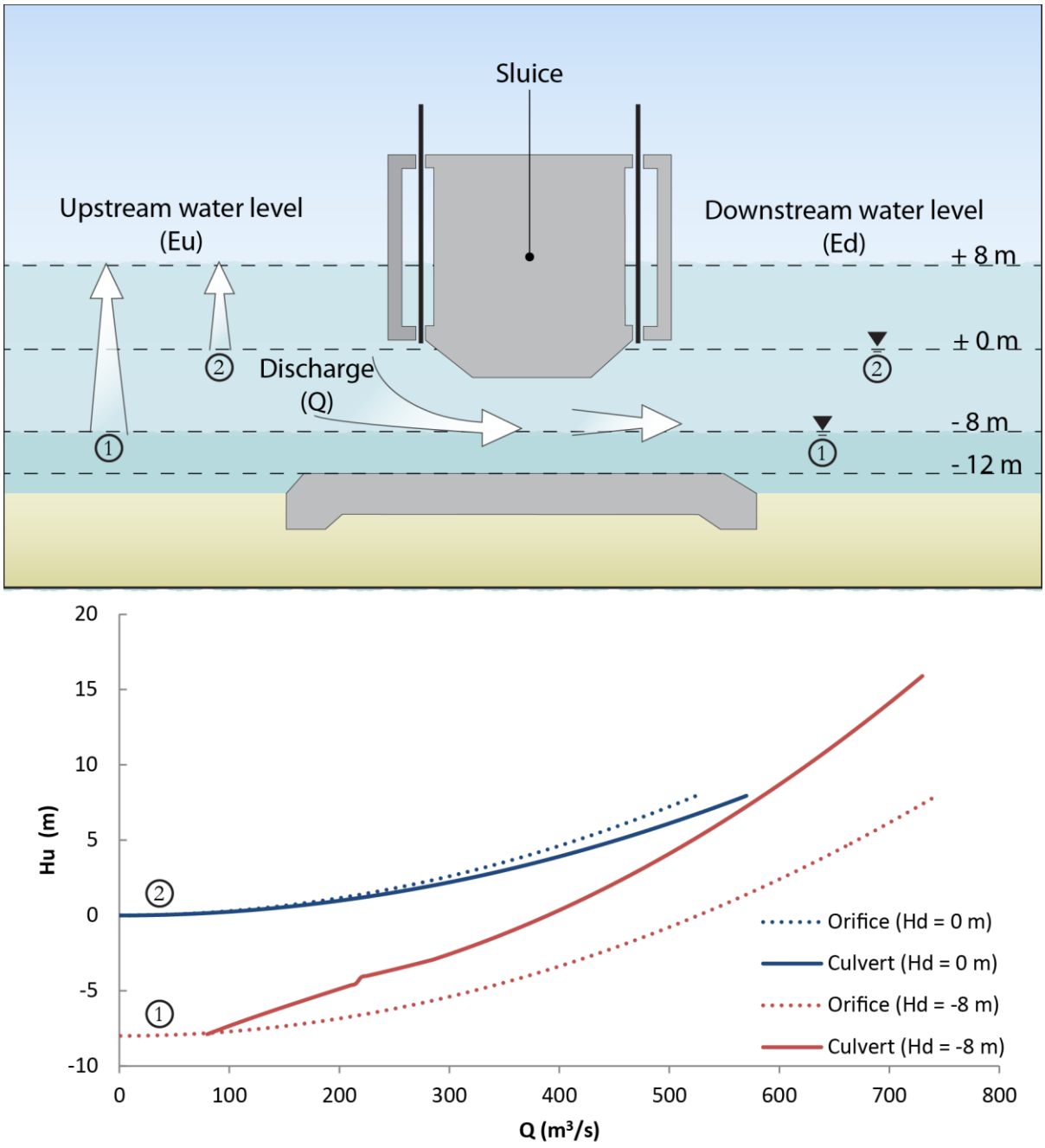

Figure A.12: Hydraulic processes of a sluice for an invert elevation of -8m.

C.3 Plant configuration

C.3.1 Depth / area curves

Figure A.13 and Figure A.14 illustrates the depth / area curves for coastal and offshore tidal lagoons, respectively.

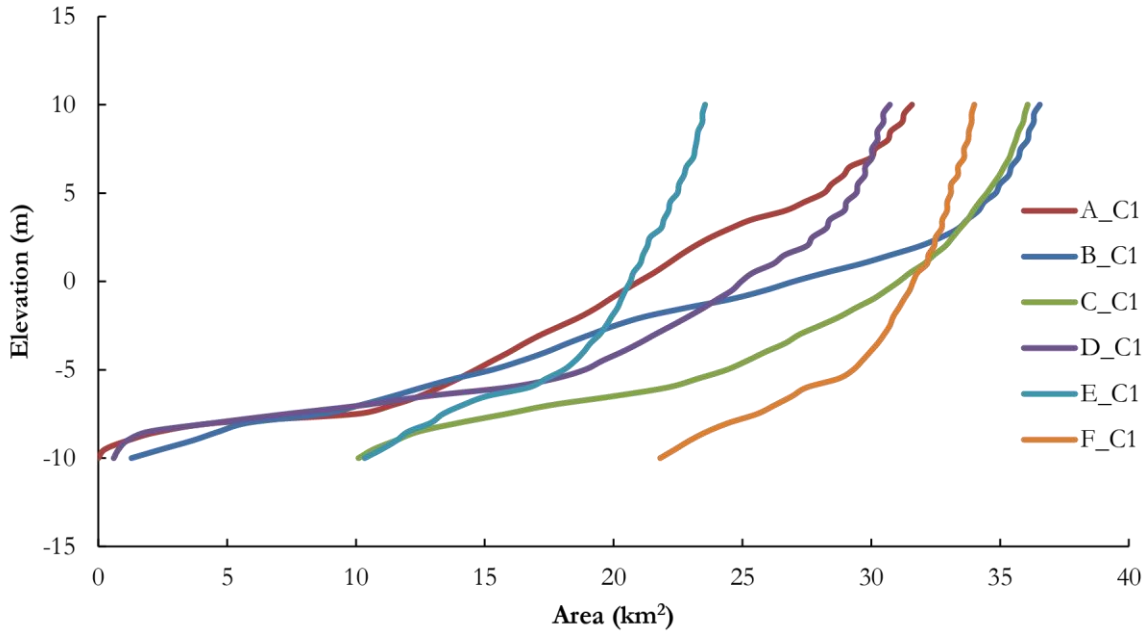

Figure A.13: Depth / area curves for coastal tidal lagoons.

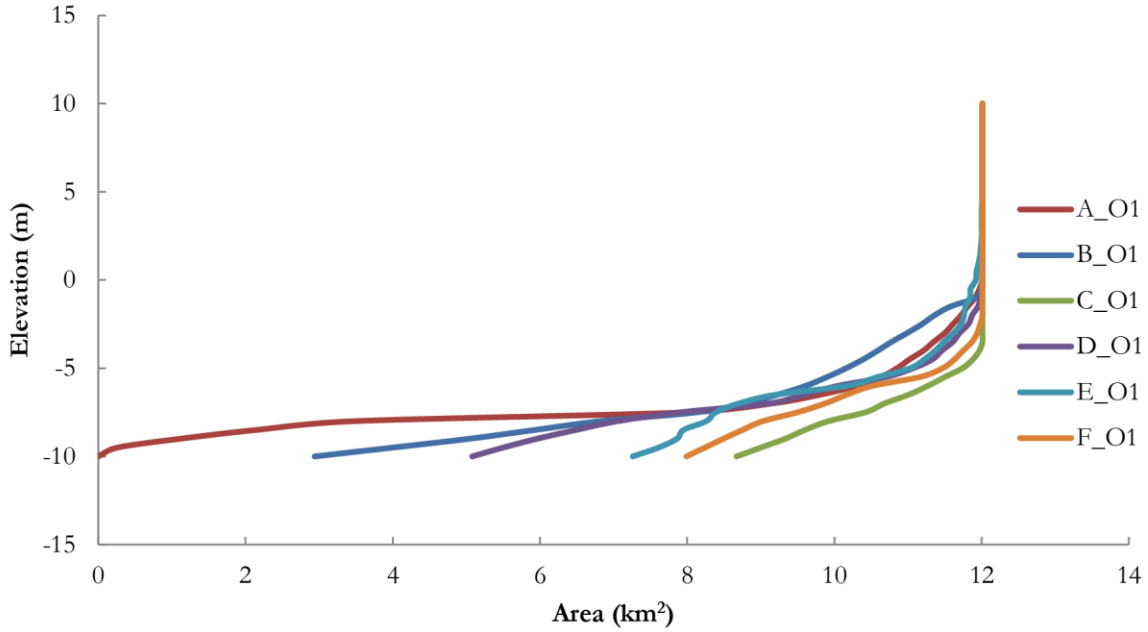

Figure A.14: Depth / area curves for offshore tidal lagoons.

Annexe D

Project Simulation Log

D.1 Calibration

Date/Time characteristics

Name of simulation period	A
Cold start	
Start time	2007-08-07 00:00:00
Duration	3 00:00:00
Simulation time step	10 seconds
Output time step	60 minutes
Hot start	
Start time	2007-08-10 00:00:00
Duration	7 09:30:00
Simulation time step	10 seconds
Output time step	10 minutes

Simulation characteristics

Simulation name	MCD_1_A_1	MCD_1_A_2	MCD_1_A_3	MCD_1_A_4
Number of constituents	1	1	1	1
Steering file	MDC_1_A_1.cas	MDC_1_A_2.cas	MDC_1_A_3.cas	MDC_1_A_4.cas
Boundary conditions file	_grid_1.conlim	_grid_2.conlim	_grid_3.conlim	_grid_4.conlim
Formatted data file 1	ICF_1_A_1.dat	ICF_1_A_2.dat	ICF_1_A_3.dat	ICF_1_A_4.dat
Fortran file	MCD_1.f	MCD_2.f	MCD_3.f	MCD_4.f
Geometry file	_grid_1.slf	_grid_2.slf	_grid_3.slf	_grid_4.slf
Liquid boundaries file	1_A_1.lqd	1_A_2.lqd	1_A_3.lqd	1_A_4.lqd
Results file	MCD__1_A_1.slf	MCD__1_A_2.slf	MCD__1_A_3.slf	MCD__1_A_4.slf

Simulation name	MCD_1_A_5	MCD_1_A_6	MCD_1_A_7	MCD_10_A
Number of constituents	1	1	1	10
Steering file	MDC_1_A_5.cas	MDC_1_A_6.cas	MDC_1_A_7.cas	MDC_10_A.cas
Boundary conditions file	_grid_5.conlim	_grid_6.conlim	_grid_7.conlim	_grid.conlim
Formatted data file 1	ICF_1_A_5.dat	ICF_1_A_6.dat	ICF_1_A_7.dat	ICF_10_A.dat
Fortran file	MCD_5.f	MCD_6.f	MCD_7.f	MCD.f
Geometry file	_grid_5.slf	_grid_6.slf	_grid_7.slf	_grid.slf
Liquid boundaries file	1_A_5.lqd	1_A_6.lqd	1_A_7.lqd	10_A.lqd
Results file	MCD__1_A_5.slf	MCD__1_A_6.slf	MCD__1_A_7.slf	MCD__10_A.slf

D.2 Validation

Simulation name	MVD_10_A	MVD_10_B	MVD_10_C	MVD_10_D
Cold start				
Start time	2007-08-07 00:00:00	2007-08-14 00:00:00	2009-01-04 00:00:00	2009-07-14 00:00:00
Duration	3 00:00:00	3 00:00:00	3 00:00:00	3 00:00:00
Simulation time step	10 seconds	10 seconds	10 seconds	10 seconds
Output time step	60 minutes	60 minutes	60 minutes	60 minutes
Hot start				
Start time	2007-08-10 00:00:00	2007-08-17 00:00:00	2009-01-07 00:00:00	2009-07-17 00:00:00
Duration	14 18:30:00	29 13:00:00	29 13:00:00	29 13:00:00
Simulation time step	10 seconds	10 seconds	10 seconds	10 seconds
Output time step	10 minutes	30 minutes	30 minutes	30 minutes

Number of constituents	10	10	10	10
Steering file	MVD_10_A.cas	MVD_10_B.cas	MVD_10_C.cas	MVD_10_D.cas
Boundary conditions file	_grid.conlim	_grid.conlim	_grid.conlim	_grid.conlim
Formatted data file 1	ICF_1_A.dat	ICF_1_B.dat	ICF_1_C.dat	ICF_1_D.dat
Fortran file	MCD.f	MCD.f	MCD.f	MCD.f
Geometry file	_grid.slf	_grid.slf	_grid.slf	_grid.slf
Liquid boundaries file	1_A.lqd	1_B.lqd	1_C.lqd	1_D.lqd
Results file	MCD__1_A.slf	MCD__1_B.slf	MCD__1_C.slf	MCD__1_D.slf

D.3 Hypothetical Scenarios

Date/Time characteristics

Name of simulation period	A
Cold start	
Start time	2007-08-07 00:00:00
Duration	3 00:00:00
Simulation time step	10 seconds
Output time step	60 minutes
Hot start	
Start time	2007-08-10 00:00:00
Duration	14 18:30:00
Simulation time step	10 seconds
Output time step	10 minutes

Simulation name	MDD_A_C1_10_A	MDD_A_O1_10_A	MDD_A_C1A_10_A	MDD_A_C1B_10_A
Number of constituents	10	10	10	10
Steering file	MDD_A_C1_10_A.cas	MDD_A_O1_10_A.cas	MDD_A_C1A_10_A.cas	MDD_A_C1B_10_A.cas
Boundary conditions file	A_C1_grid.conlim	A_O1_grid.conlim	A_C1_grid.conlim	A_C1_grid.conlim
Formatted data file 1	ICF_10_A.dat	ICF_10_A.dat	ICF_10_A.dat	ICF_10_A.dat
Fortran file	MDD_A.f	MDD_A.f	MDD_A.f	MDD_B.f
Geometry file	A_C1_grid.slf	A_O1_grid.slf	A_C1_grid.slf	A_C1_grid.slf
Liquid boundaries file	10_A.lqd	10_A.lqd	10_A.lqd	10_A.lqd
Results file	MDD_A_C1_10_A.slf	MDD_A_O1_10_A.slf	MDD_A_C1A_10_A.slf	MDD_A_C1B_10_A.slf

Simulation name	MDD_A_C1C_10_A	MDD_A_C1D_10_A	MDD_A_C1E_10_A	MDD_A_C2_10_A
Number of constituents	10	10	10	10
Steering file	MDD_A_C1C_10_A.cas	MDD_A_C1D_10_A.cas	MDD_A_C1E_10_A.cas	MDD_A_C2_10_A.cas
Boundary conditions file	A_C1_grid.conlim	A_C1_grid.conlim	A_C1_grid.conlim	A_C2_grid.conlim
Formatted data file 1	ICF_10_A.dat	ICF_10_A.dat	ICF_10_A.dat	ICF_10_A.dat
Fortran file	MDD_C.f	MDD_D.f	MDD_E.f	MDD_A.f
Geometry file	A_C1_grid.slf	A_C1_grid.slf	A_C1_grid.slf	A_C2_grid.slf
Liquid boundaries file	10_A.lqd	10_A.lqd	10_A.lqd	10_A.lqd
Results file	MDD_A_C1C_10_A.slf	MDD_A_C1D_10_A.slf	MDD_A_C1E_10_A.slf	MDD_A_C2_10_A.slf

Simulation name	MDD_A_C3_10_A	MDD_A_O1_10_A	MDD_A_O2_10_A	MDD_A_O3_10_A
Number of constituents	10	10	10	10
Steering file	MDD_A_C3_10_A.cas	MDD_A_O1_10_A.cas	MDD_A_O2_10_A.cas	MDD_A_O3_10_A.cas
Boundary conditions file	A_C3_grid.conlim	A_O1_grid.conlim	A_O2_grid.conlim	A_O3_grid.conlim
Formatted data file 1	ICF_10_A.dat	ICF_10_A.dat	ICF_10_A.dat	ICF_10_A.dat
Fortran file	MDD_A.f	MDD_A.f	MDD_A.f	MDD_A.f
Geometry file	A_C3_grid.slf	A_O1_grid.slf	A_O2_grid.slf	A_O3_grid.slf
Liquid boundaries file	10_A.lqd	10_A.lqd	10_A.lqd	10_A.lqd
Results file	MDD_A_C3_10_A.slf	MDD_A_O1_10_A.slf	MDD_A_O2_10_A.slf	MDD_A_O3_10_A.slf

Simulation name	MDD_B_C1_10_A	MDD_C_C1_10_A	MDD_m3_C1_10_A	MDD_m3_O1_10_A
Number of constituents	10	10	10	10
Steering file	MDD_B_C1_10_A.cas	MDD_C_C1_10_A.cas	MDD_m3_C1_10_A.cas	MDD_m3_O1_10_A.cas
Boundary conditions file	B_C1_grid.conlim	C_C1_grid.conlim	m3_C1_grid.conlim	m3_O1_grid.conlim

Formatted data file 1	ICF_10_A.dat	ICF_10_A.dat	ICF_10_A.dat	ICF_10_A.dat
Fortran file	MDD_A.f	MDD_A.f	MDD_A.f	MDD_A.f
Geometry file	B_C1_grid.slf	C_C1_grid.slf	m3_C1_grid.slf	m3_O1_grid.slf
Liquid boundaries file	10_A.lqd	10_A.lqd	10_A.lqd	10_A.lqd
Results file	MDD_B_C1_10_A.slf	MDD_C_C1_10_A.slf	MDD_m3_C1_10_A.slf	MDD_m3_O1_10_A.slf

Simulation name	MDD_m3_C2_10_A	MDD_m3_O2_10_A	MDD_m6_O1_10_A
Number of constituents	10	10	10
Steering file	MDD_m3_C2_10_A.cas	MDD_m3_O2_10_A.cas	MDD_m6_O1_10_A.cas
Boundary conditions file	m3_C2_grid.conlim	m3_O2_grid.conlim	m6_O1_grid.conlim
Formatted data file 1	ICF_10_A.dat	ICF_10_A.dat	ICF_10_A.dat
Fortran file	MDD_A.f	MDD_A.f	MDD_A.f
Geometry file	m3_C2_grid.slf	m3_O2_grid.slf	m6_O1_grid.slf
Liquid boundaries file	10_A.lqd	10_A.lqd	10_A.lqd
Results file	MDD_m3_C2_10_A.slf	MDD_m3_O2_10_A.slf	MDD_m6_O1_10_A.slf

Annexe E

Results and analysis for S3 to S19

E.1 Operation mode (S3 to S7)

A - Water level: Maximum tidal range

Figure A.15 shows the change in maximum tidal range for different operation modes. All the simulations, S3 to S7, were simulated with the coastal tidal lagoon A_C1. All the operation modes are explained in Section 4.3.1.2.

As illustrated in the figure, the power generation modes (S3 to S5) will have similar changes in maximum tidal range. The tidal range will increase between 2 and 8 cm at the entrance of Minas Basin and in Chignecto Bay, and between 2 and 4 cm in the lower Bay of Fundy. There is some tidal range increase in the Gulf of Maine between 1 and 2 cm.

Scenario S6, where turbine gates are always closed and sluices are always opened, tidal range will decrease in Minas Basin by 2 to 8 cm and increase by 1 to 2 cm for the rest of the Bay of Fundy and the Gulf of Maine. If turbine and sluice gates are closed, S7, tidal range will increase by 4 to 8 cm in the Upper Bay of Fundy, 2 to 4 cm in the lower Bay of Fundy and 1 to 2 cm in the Gulf of Maine.

By far the largest changes in water levels occur within the lagoon itself, where the tidal range is reduced by several meters, relative to existing conditions. The exact tidal range reduction depends on the operation scheme and the characteristics of the turbines and sluices. The estimated reduction in tidal range is around 6.33 m for S3, 7.54 m for S4, 4.65 m for S5 and 2.98 m for S6. The change in tidal range for S7 is not applicable since the water is still during the entire simulation.

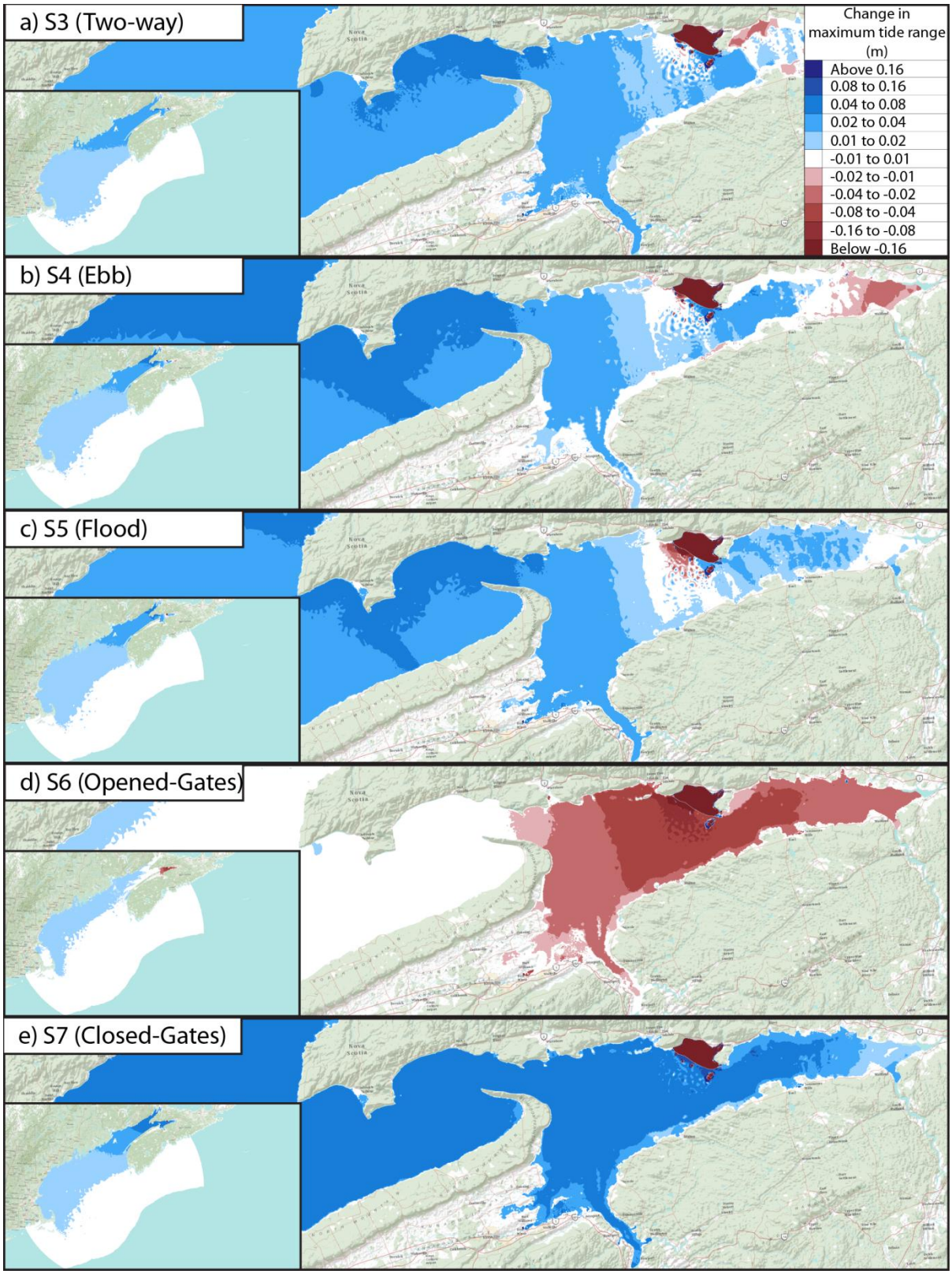

Figure A.15: Changes in maximum tidal range for S3 to S7.

B - Current velocity: Maximum and RMS current velocities

Figure A.16.a to Figure A.16.e shows the change in maximum current velocity in Minas Basin for S3 to S7. There are minor differences in maximum current velocity between S3 to S7. The maximum current velocity will be 2 to 4 cm/s slower to existing conditions. As illustrated, tidal currents outside Minas Basin are very weakly affected, if at all.

The most noticeable velocity changes occur near the lagoons, both inside and outside the impoundment dikes. Within the lagoon, compared to existing conditions, peak velocities are generally higher near the powerhouse and lower in other regions within the impoundment.

The most significant velocity increases are shown to occur outside the powerhouse, adjacent to the sluices and turbines. Higher velocities occur seaward of the powerhouse because of the decrease in water depth during the ebb tide as shown in Figure A.17. Outside the lagoon, compared to existing conditions, peak velocities tend to amplify near the powerhouse and in certain areas near the perimeter of the impoundment, while peak velocities are attenuated in other areas.

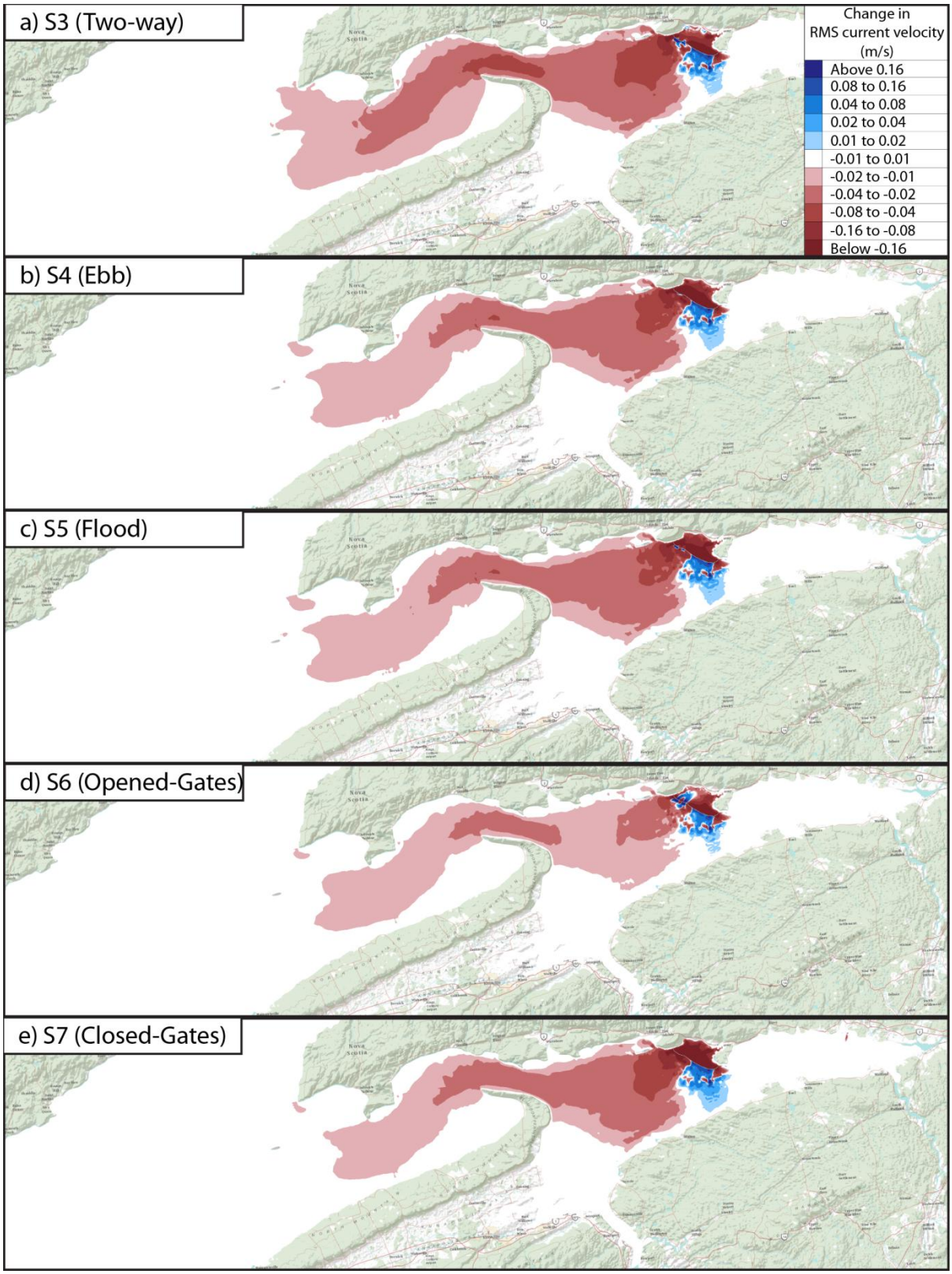

Figure A.16: Changes in RMS current velocity for S3 to S7.

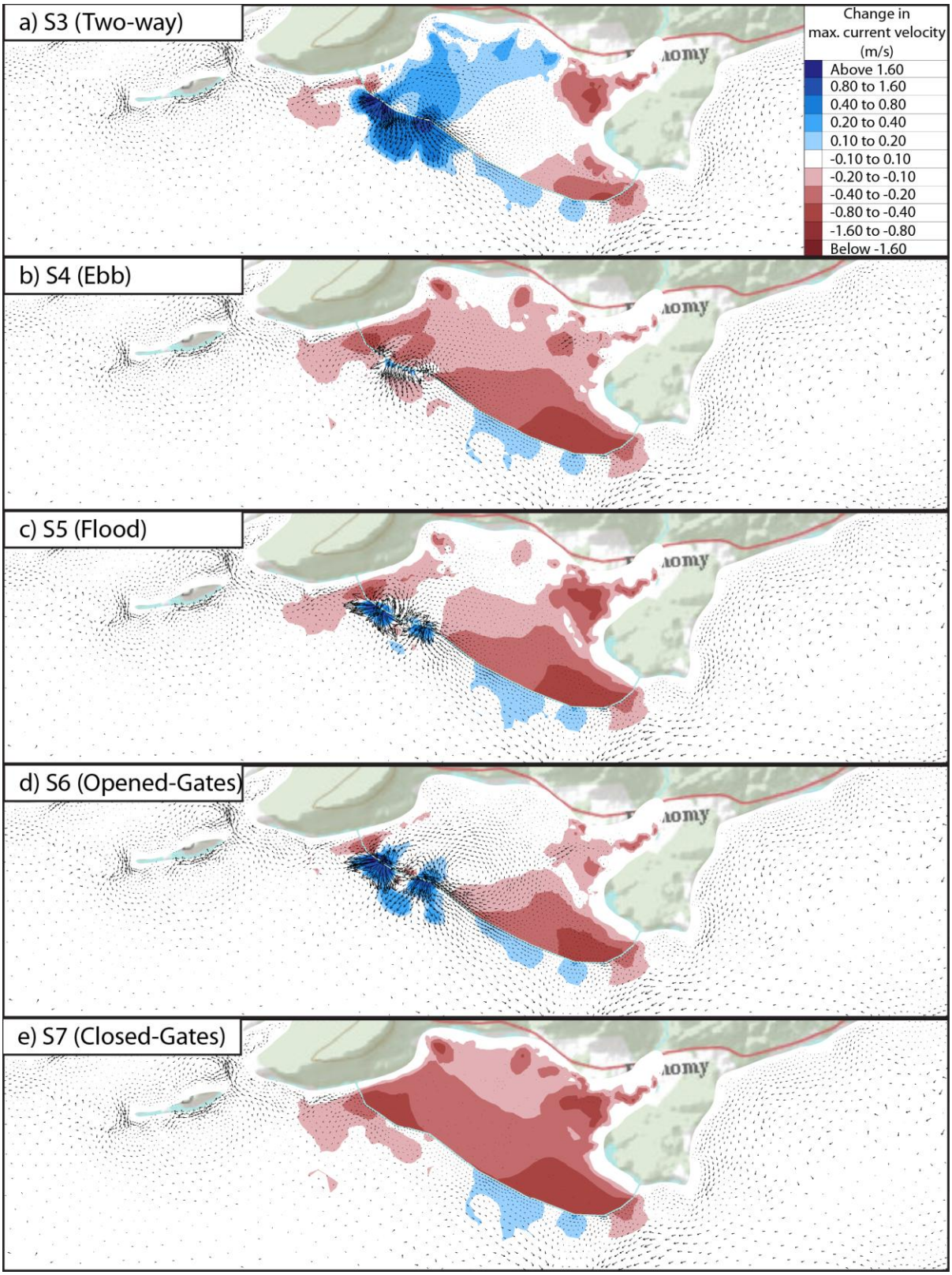

Figure A.17: Changes in maximum current velocity for S3 to S7.

C - Power output

The time-varying power outputs for scenarios S3, S4 and S5 are compared graphically in Figure A.18. In this figure the power output computed from the finite-element modeling is compared with the power output produced by the analytic model of plant operations (the "box" model) described in Chapter 3. There are minor differences in power output between both models. As illustrated in this time series, the maximum power output and the phase are not identical. The phase difference between these models varies from 20 to 30 min at the start of the power generation and from 10 to 20 min at the end of the power generation.

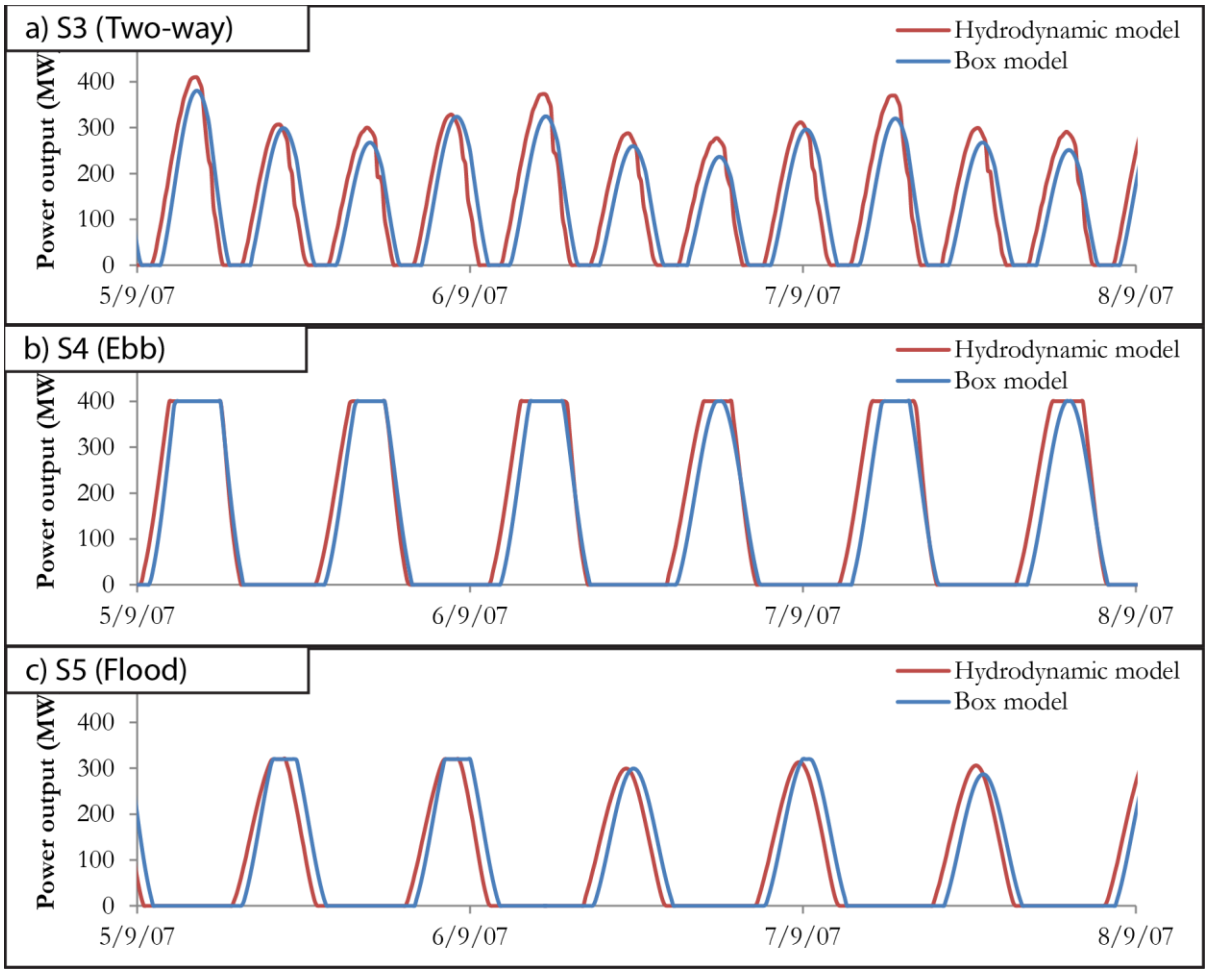

Figure A.18: Changes in maximum tidal range for S3, S8 and S9.

There are numerous reasons why these results are not identical. The water level from the box model was simulated from 10 constituents from tidal station Five Islands which is located around 50 km away from the site. This distance could potentially alter the power generation period and alternate results. In addition, the box model is based on the assumptions that a volume

of water let into the basin will raise the level of the basin by an amount equal to the volume let in divided by the area of the basin at the time, i.e. spread uniformly over the basin. Furthermore, large dynamic effects due to power extraction from the tidal lagoon is altering water level inside Minas Basin, thus alternating results.

Table A.4 shows the average power output for both models. For S3, where the power operating mode is two-way generation, the box model over-estimates the power output and the power generation. As for S4 and S5, ebb and flood generation, the box model is actually underestimates the power output and the power generation.

Table A.4: RMS power output and RMS power generation for S3 to S5.

	Hydrodynamic model	**Box model**
Simulation	Average power output (MW)	Average power output (MW)
S3	242.91	260.62
S4	246.38	227.11
S5	171.98	166.89

E.2 Tidal lagoon size (S8 to S12)

E.2.1 Coastal lagoon

A - Water level: Maximum tidal range

Figure A.19.a to Figure A.19.c shows the change in maximum tidal range due to three different coastal tidal lagoons. All of these lagoons are place approximately in the same location but have different sizes.

The smallest lagoon, S3, has an area of around 26.66 km^2 and will increase tidal range between 2 cm and 8 cm at the entrance of Minas Basin and in Chignecto Bay, and between 2 cm and 4 cm in the lower Bay of Fundy. There is some increase in tidal range in the Gulf of Maine between 1 cm and 2 cm. The coastal lagoon, S8, with an area of 35.10 m^2 will increase tidal range by 4 to 8 cm in the Bay of Fundy and 2 to 4 cm in the Gulf of Maine. The biggest coastal lagoon, S9, with an area of 57.65 m^2 will increase tidal range by 8 to 16 cm in the Bay of Fundy and 4 to 8 cm in the Gulf of Maine.

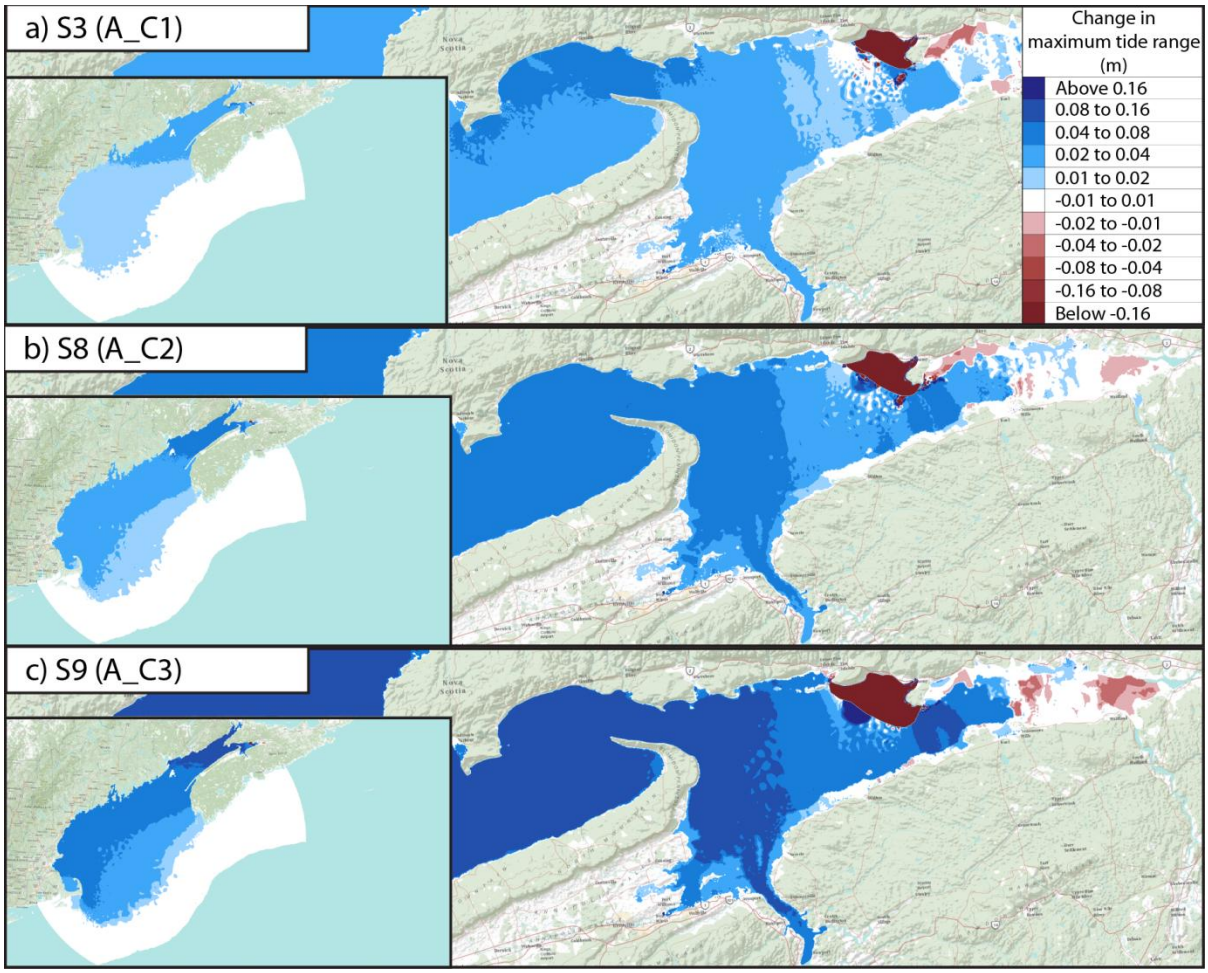

Figure A.19: Changes in maximum tidal range for S3, S8 and S9.

D - Current velocity: RMS current velocity and residual currents

The RMS current velocity only changes in the vicinity of the tidal lagoon and in the Minas Passage. Figure A.20.a to Figure A.20.c shows the change in RMS current velocity in Minas Basin for S3, S8 and S9. There is a decrease in current velocity by 1 to 16 cm/s in the Minas Passage depending on the tidal lagoon layout and remains below 1 cm/s throughout most of the Bay of Fundy and in the entire Gulf of Maine.

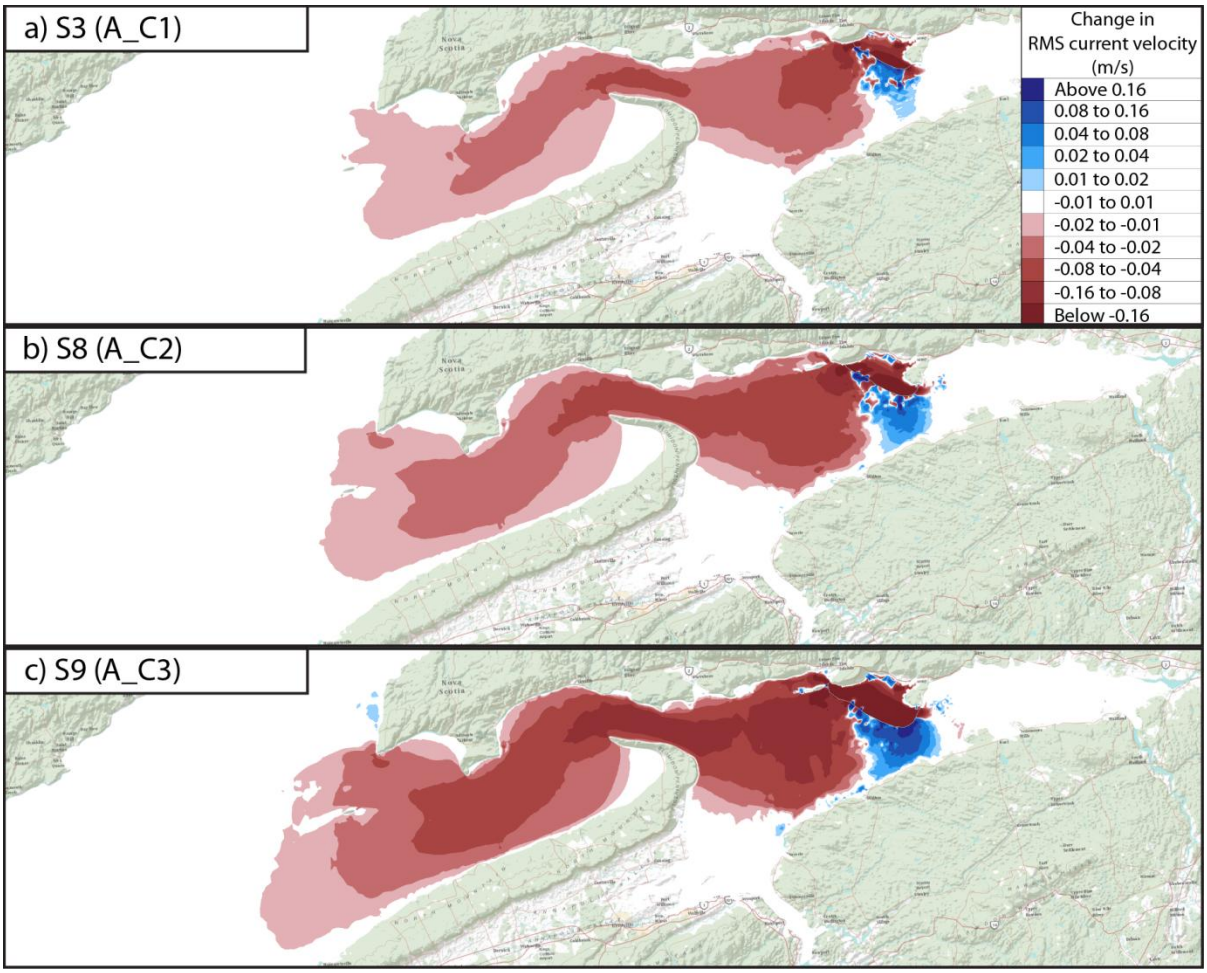

Figure A.20: Changes in RMS current velocity for S3, S8 and S9.

Figure A.21.a to Figure A.21.c shows the change in RMS current velocity and shows residual currents near the tidal lagoons for S3, S8 and S9. As mention before, the most significant velocity increases are shown to occur near the powerhouse, adjacent to the sluices and turbines. It's worth to note that although the number of turbines and sluices increases with respect to the increase in lagoon size, the length of the powerhouse is always 2,000 m for all the simulations. Hence, the flow concentration near the powerhouse will be higher for bigger lagoons compared to smaller lagoons. Therefore, the magnitude of current velocity along the power house should be taken with precaution.

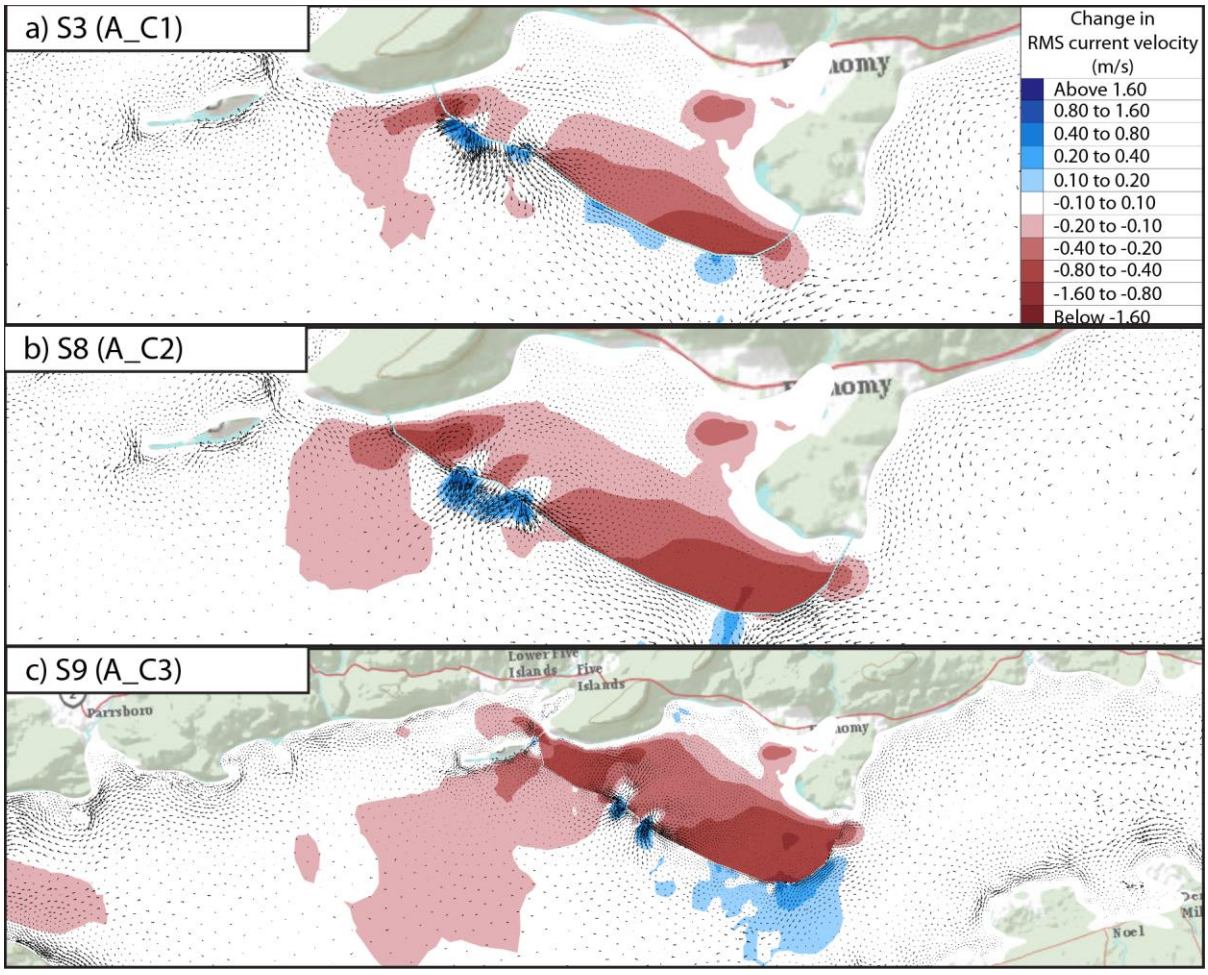

Figure A.21: Changes in RMS current velocity and residual currents for S3, S8 and S9.

E.2.2 Offshore lagoon

A - Water level: Maximum tidal range

Using the same approach as the coastal lagoon scenarios, Figure A.22.a to Figure A.22.c shows the change in maximum tidal range due to three offshore tidal lagoon with different sizes. The largest lagoon, S12, has an area of around 23.99 km^2 and will increase tidal range by 4 to 8 cm at the entrance of Minas Basin and in Chignecto Bay, and between 2 cm and 4 cm in the lower Bay of Fundy and Gulf of Maine. The offshore tidal lagoon will have mixture of increases and decreases in tidal range in the Minas Basin. Although local change patterns are different, far-field pattern changes are very similar to the coastal lagoon.

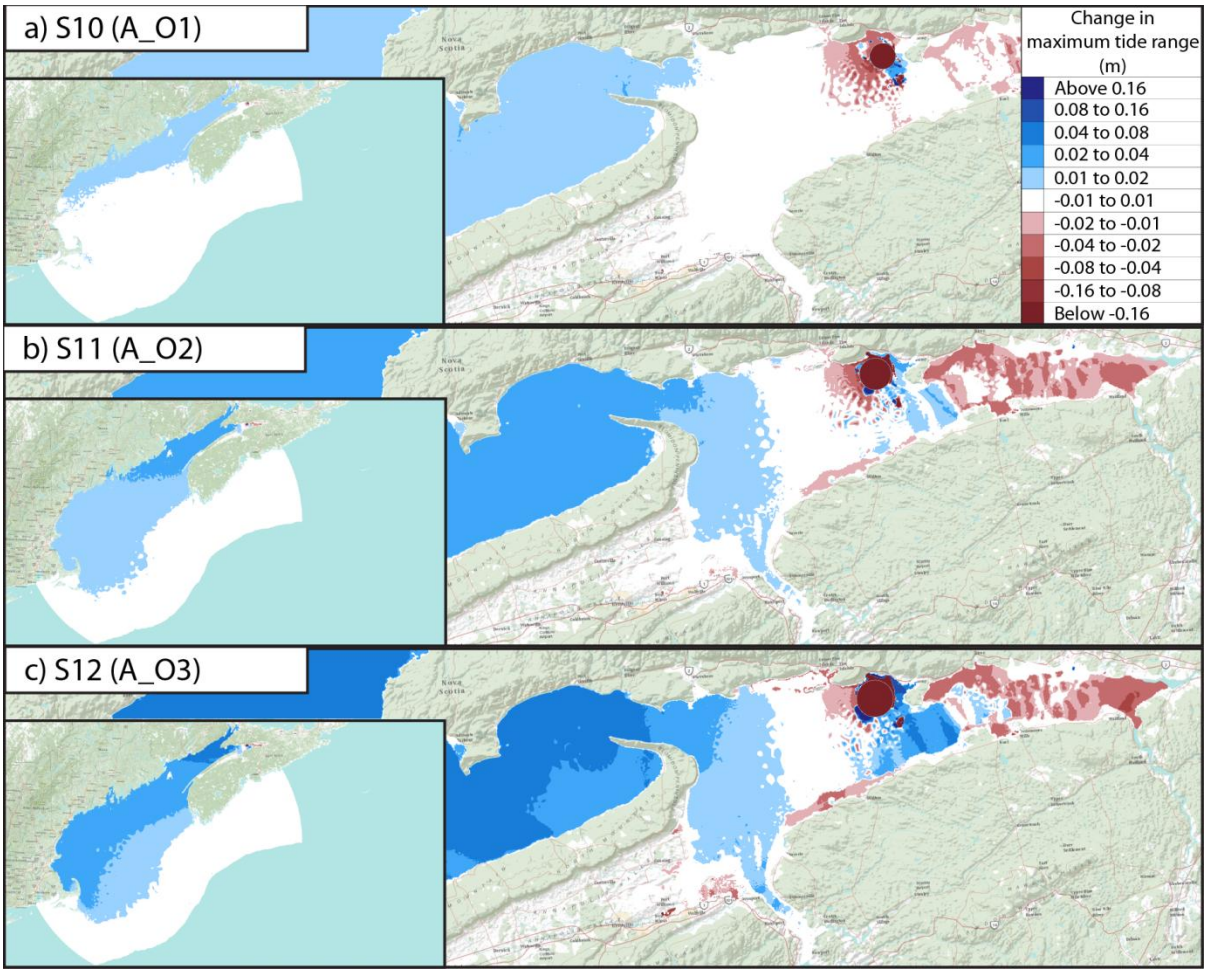

Figure A.22: Changes in maximum tidal range for S10 to S12.

B - Current velocity: RMS current velocity and residual currents

The patterns in current velocities are very similar to the coastal simulations. Figure A.23.a to Figure A.23.c shows the change in RMS current velocity in Minas Basin for S10 to S12. There is a decrease in current velocity by 1 to 8 cm/s in the Minas Passage depending on the tidal lagoon layout and remains below 1 cm/s throughout most of the Bay of Fundy and in the entire Gulf of Maine.

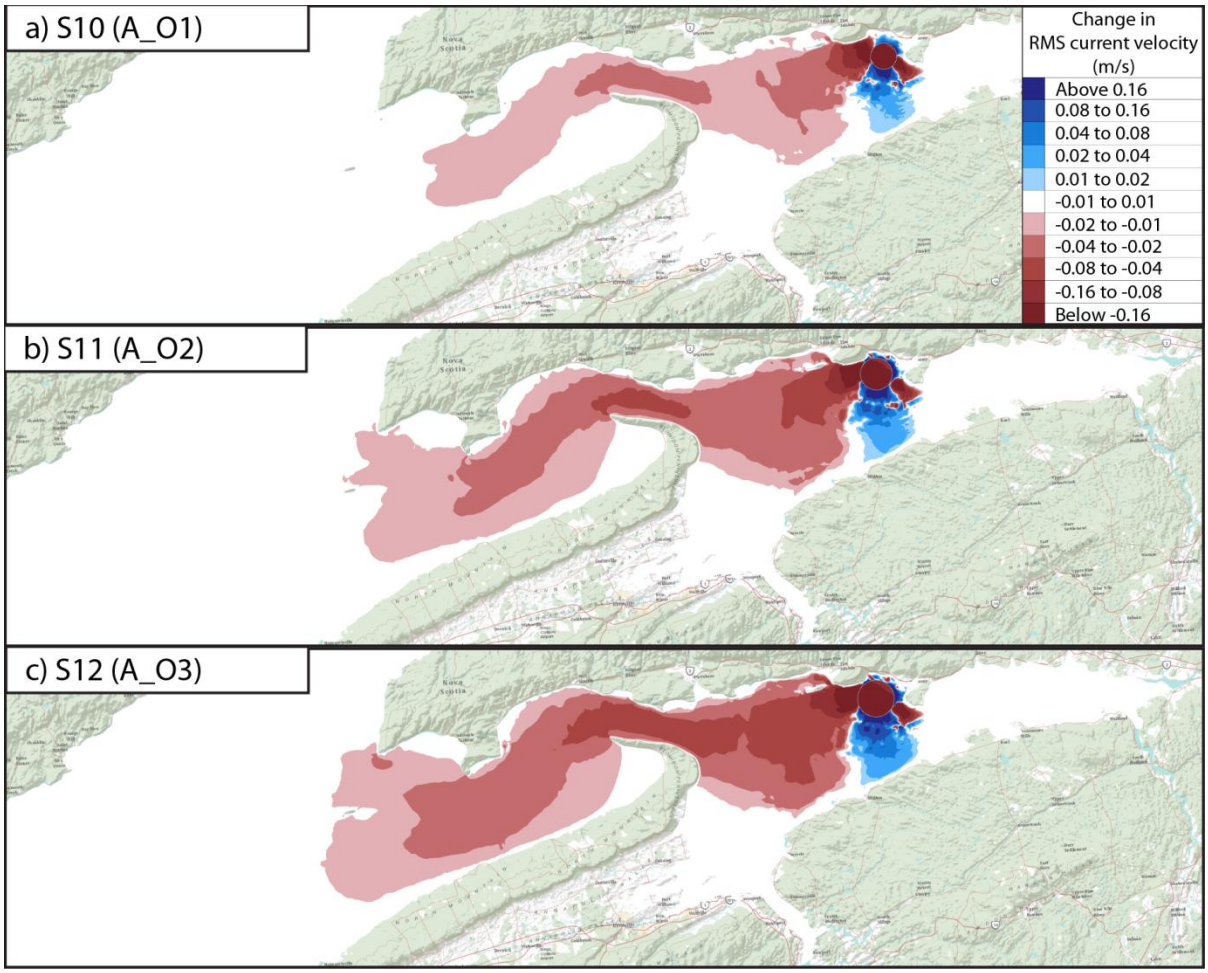

Figure A.23: Changes in RMS current velocity for S10 to S12.

Figure A.24.a to Figure A.24.c shows the change in RMS current velocity and shows residual currents near the tidal lagoons for S10 to S12. As explain in Section E.2.1, although the size of the lagoon increases, the powerhouse length remains 2,000 m. The magnitude of current velocity along the powerhouse should be taken with precaution.

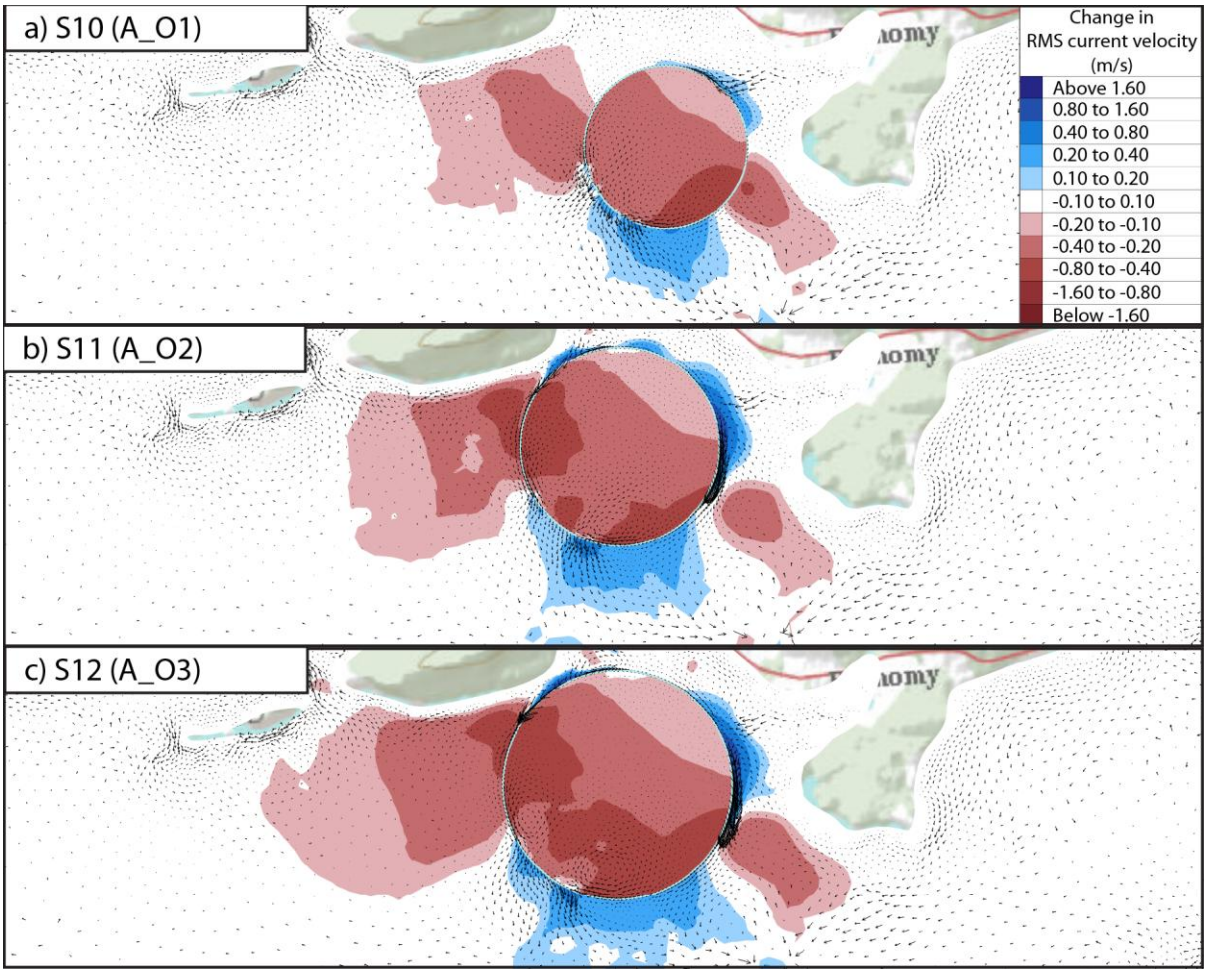

Figure A.24: Changes in RMS current velocity and residual currents for S10 to S12.

E.3 Tidal lagoon location (S13 to S14)

A - Water level: Maximum tidal range

Figure A.25.a to Figure A.25.c shows the change in maximum tidal range due to three coastal tidal lagoons at different location in the Minas Basin.

As shown in the figure, the hydrodynamic behaves very differently for each scenario. Scenario S13, where the tidal lagoon is place on the north-eastern coast of Minas Basin, will increase tidal range by 8 to 16 cm in Minas Basin, and it will increase by 4 to 8 cm in Chignecto Bay and lower Bay of Fundy. In addition, tidal range will increase in the Gulf of Maine by 1 to 4 cm.

Scenario S14, where the tidal lagoon is place on the southern coast of Minas Basin, will increase tidal range by 2 to 4 cm in Chignecto Bay, lower Bay of Fundy and Gulf of Maine. Tidal range will generally decrease in Minas Basin by 1 to 2 cm.

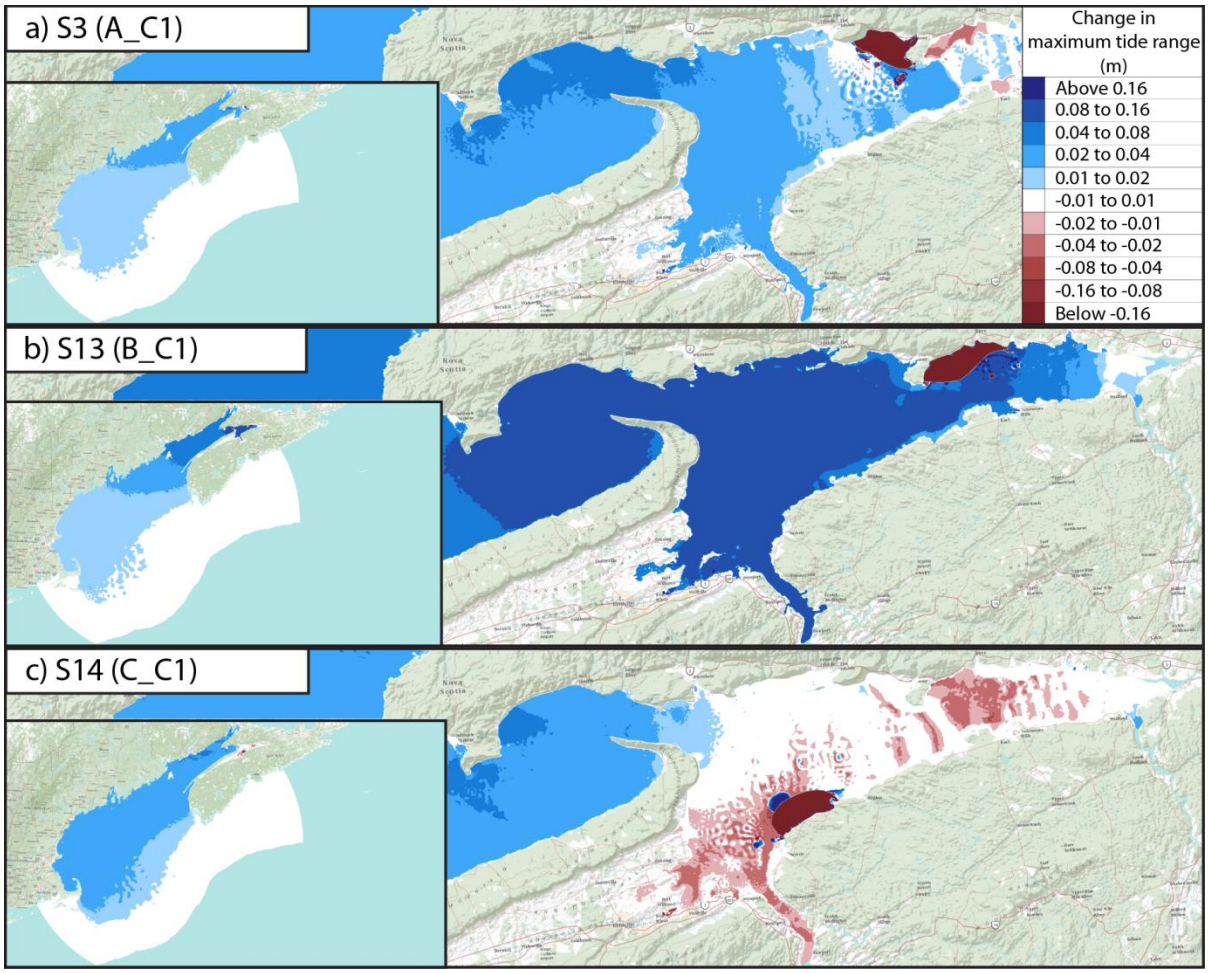

Figure A.25: Changes in maximum tidal range for S3, S13 and S14.

B - Current velocity: RMS velocity

Figure A.26.a to Figure A.26.c shows the change in RMS current velocity in Minas Basin for S3, S13 and S14.

The changes in velocity patterns from the Minas Passage towards to tidal lagoon are similar for all the scenarios. Velocities have a tendency to decrease by 8 to 16 cm/s in the vicinity of the tidal lagoon and by 2 to 8 cm/s in the Minas Passage. The most significant velocity increases are shown to occur near the powerhouse and along the impoundment depending on the tidal lagoon layout and powerhouse configuration.

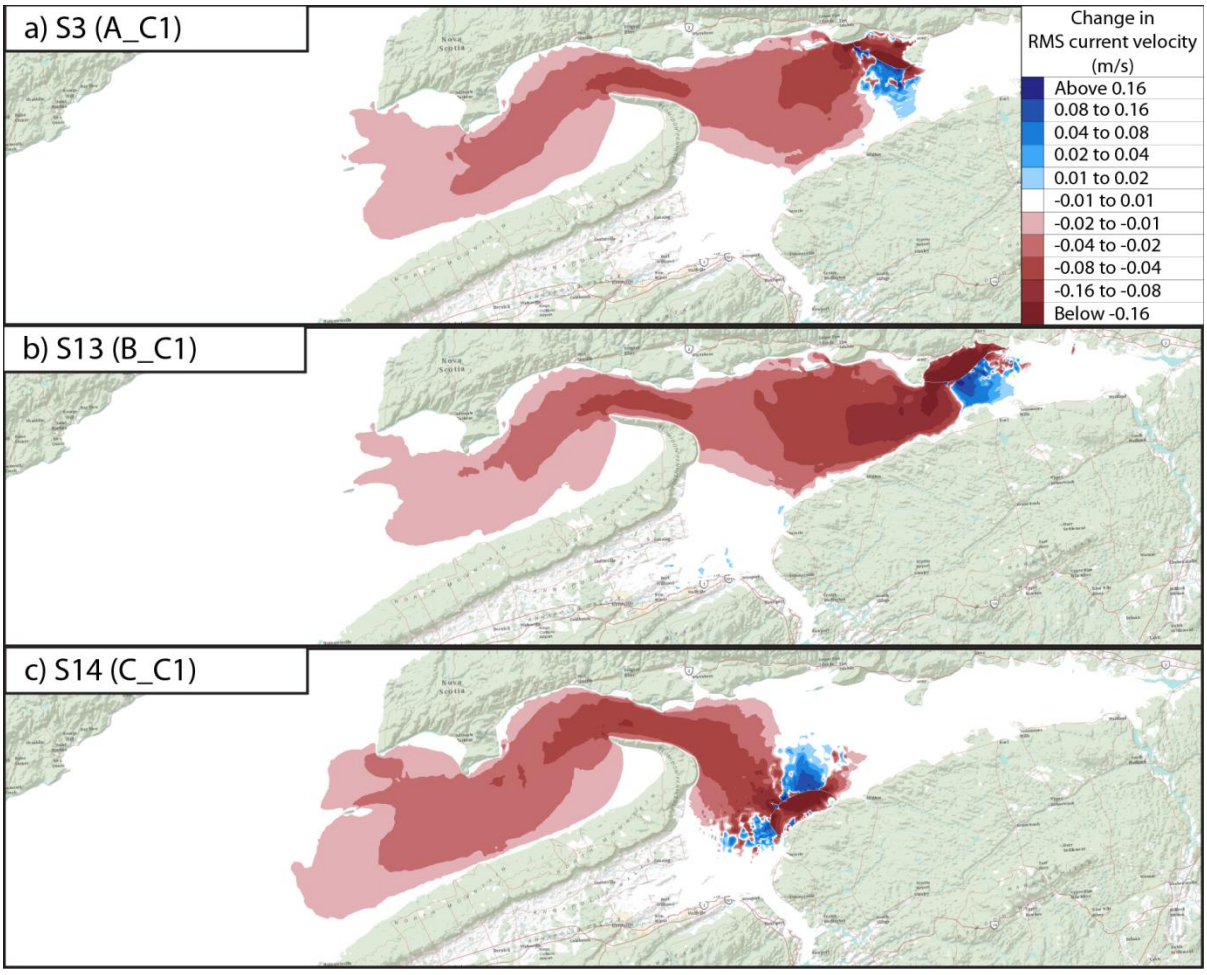

Figure A.26: Changes in RMS current velocity and residual current circulation for S3, S13 and S14.

E.4 Minas Basin (S15 and S16)

A - Water level: Maximum tidal range

Figure A.27.a and Figure A.27.b shows the change in maximum tidal range due to three coastal tidal lagoons and three offshore tidal lagoons, respectively. All the lagoons are place in Minas Basin and their exact location and size are explained is Section 4.3.2.1.

By comparing the two figures, the scenario with the coastal tidal lagoons have larger impacts than the offshore tidal lagoons. This is mainly due to the fact that the coastal lagoons are taken 2.63 more area than the offshore lagoons (coastal: 94.78 km^2, offshore: 36.03 km^2). For the coastal lagoons, the maximum tidal range will increase by 8 to 16 cm in the Bay of Fundy and 4 to 8 cm in the Gulf of Maine. As for the offshore lagoons, the maximum tidal range will increase by 4 to 8 cm at the entrance of Minas Basin and in Chignecto Bay, by 4 to 8 cm in the Bay of Fund, and by 2 to 4 cm in the Gulf of Maine.

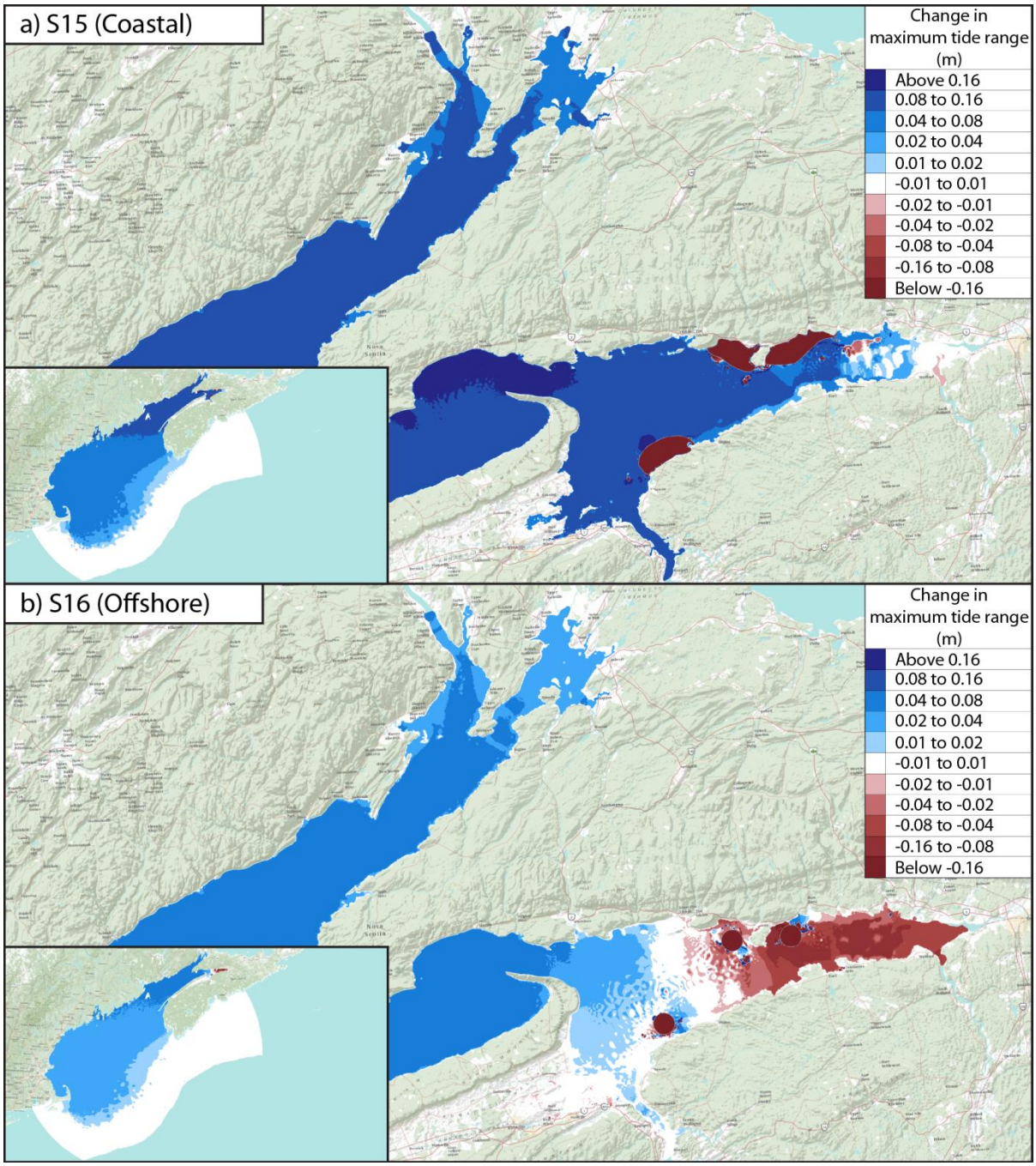

Figure A.27: Changes in maximum tidal range for S15 and S16.

B - Current velocity: RMS velocity and residual current circulation

Figure A.28.a to Figure A.28.b shows the change in maximum current velocity in Minas Basin for S15 and S16, respectively. As illustrated, the pattern changes in current velocity at the entrance of Minas Basin are very similar. Only the magnitude and the extent of velocity changes will differ. The maximum tidal current in Minas Passage will be approximately 8 to 16 cm/s

slower with the coastal lagoons and from 4 to 8 cm/s slower with the offshore lagoons. It's also worth to notice that there is an increase in velocity in Chignecto Bay by 1 to 2 cm/s.

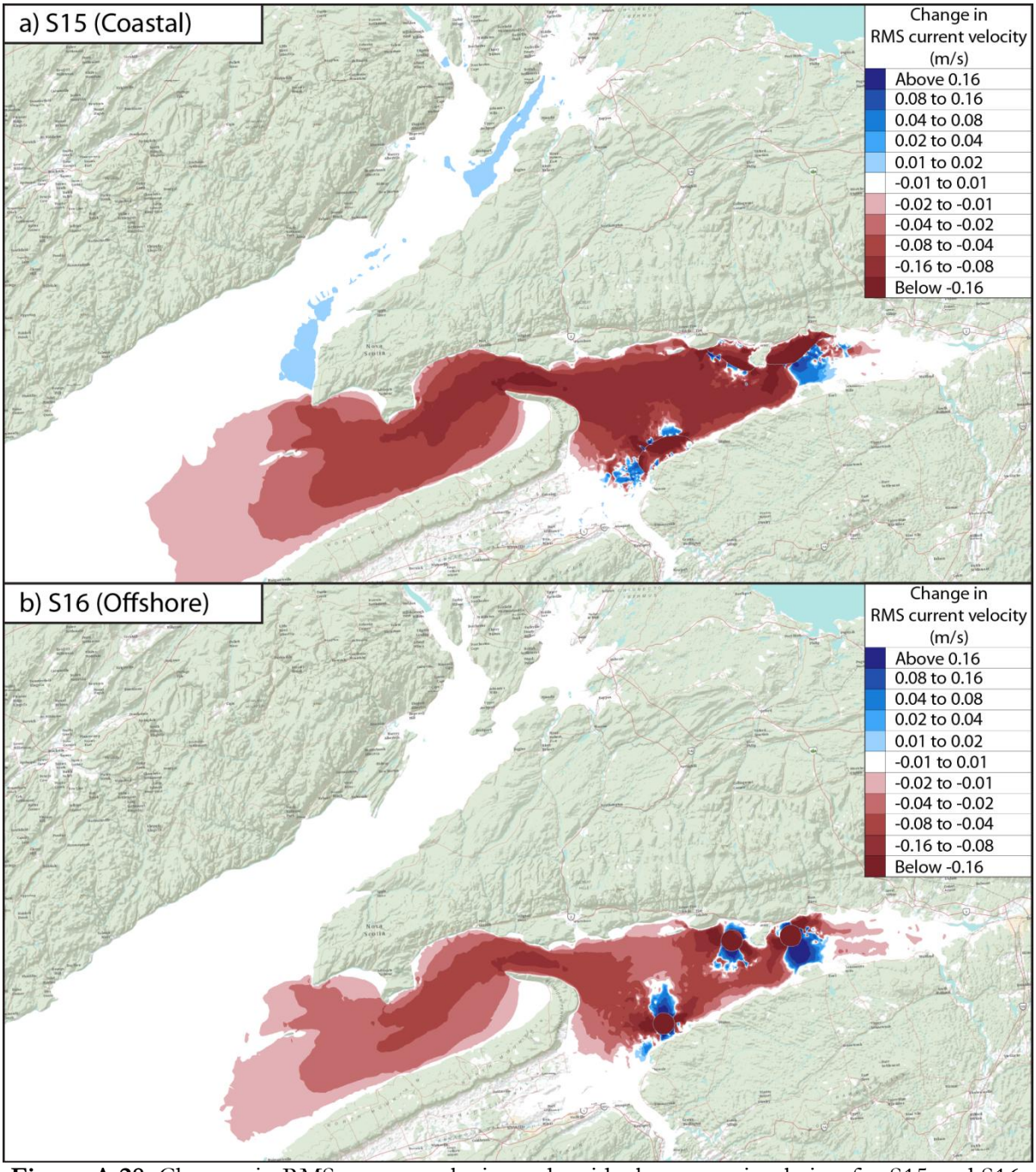

Figure A.28: Changes in RMS current velocity and residual current circulation for S15 and S16.

E.5 Chignecto Bay (S17 and S18)

A - Water level: Maximum tidal range

Figure A.29.a and Figure A.29.b shows the change in maximum tidal range due tidal lagoons in Chignecto Bay. Different from S1 to S16, these lagoons are place in Chignecto Bay. More details on the hypothetical scenarios in Section 4.3.2.2.

For the coastal lagoons, S17, the maximum tidal range will decrease by 4 to 8 cm in Minas Basin and lower Bay of Fundy, and by 8 to 16+cm in Chignecto Bay. The maximum tidal range will actually increase by 4 to 8 cm in the Gulf of Maine. As for the offshore lagoons, S18, the maximum tidal range impacts are smaller compared to the coastal tidal lagoons but the pattern changes are similar. It will decrease by 4 to 16 cm in Chignecto Bay, and by 1 to 8 cm in the rest of the Bay of Fundy. Maximum tidal range will increase by 1 to 8 cm in the Gulf of Maine.

B - Current velocity: RMS velocity

Predicted changes in the RMS velocity of the depth-averaged tidal currents coastal and offshore lagoons operating in Chignecto Bay are mapped in Figure A.30.a and Figure A.30.b. The change in velocity patterns differs from the S1 to S16. The change in velocity starts in Chignecto Bay and spreads to the lower Bay of Fundy. Velocity tends to decrease by 8 to 16 cm/s in Chignecto Bay and 1 to 4 cm/s in the lower Bay of Fundy. The RMS current velocity will decrease by 1 to 2 cm/s in Minas Passage and very weakly affected in the Minas Basin and Gulf of Maine.

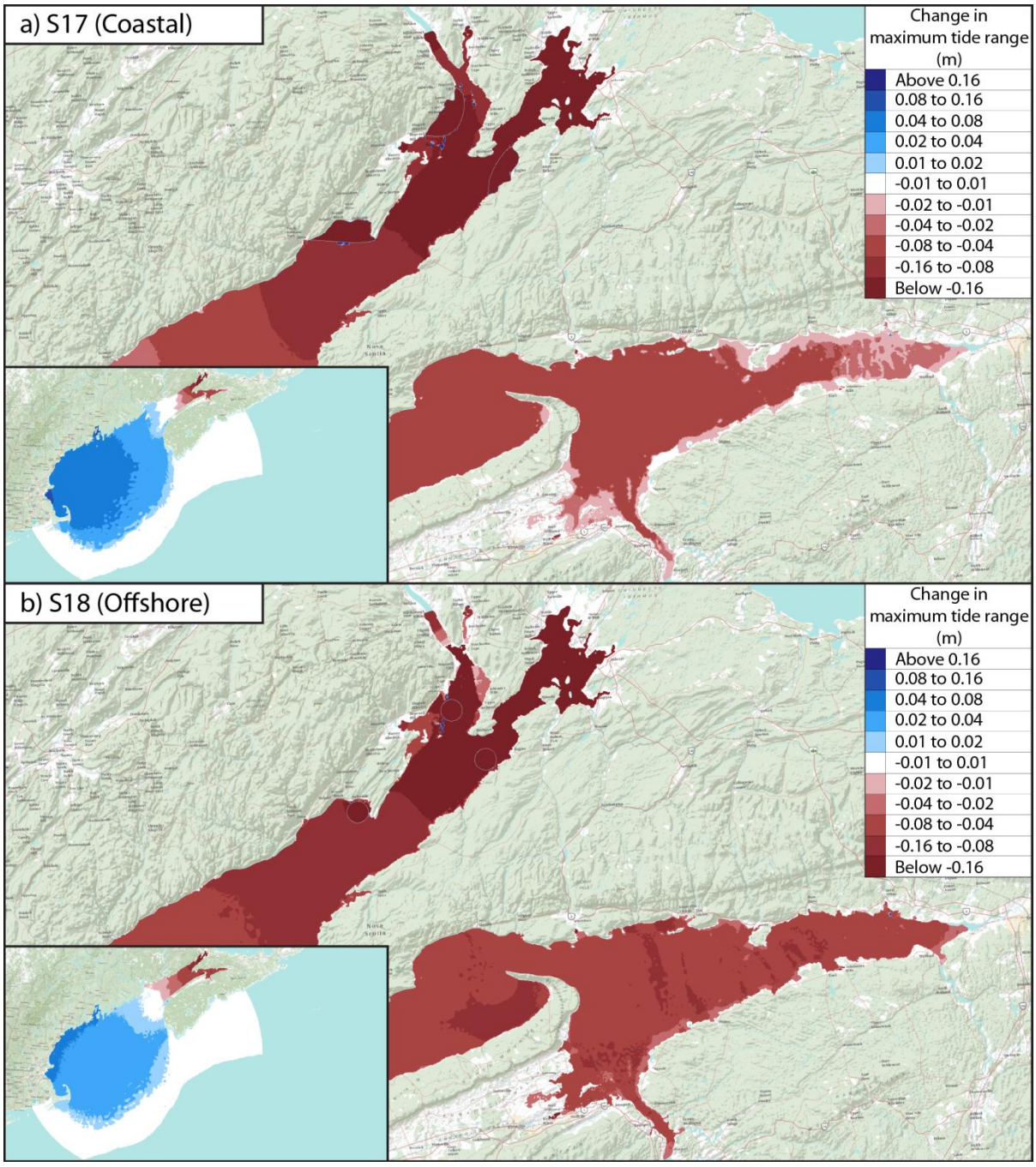

Figure A.29: Changes in maximum tidal range for S17 and S18.

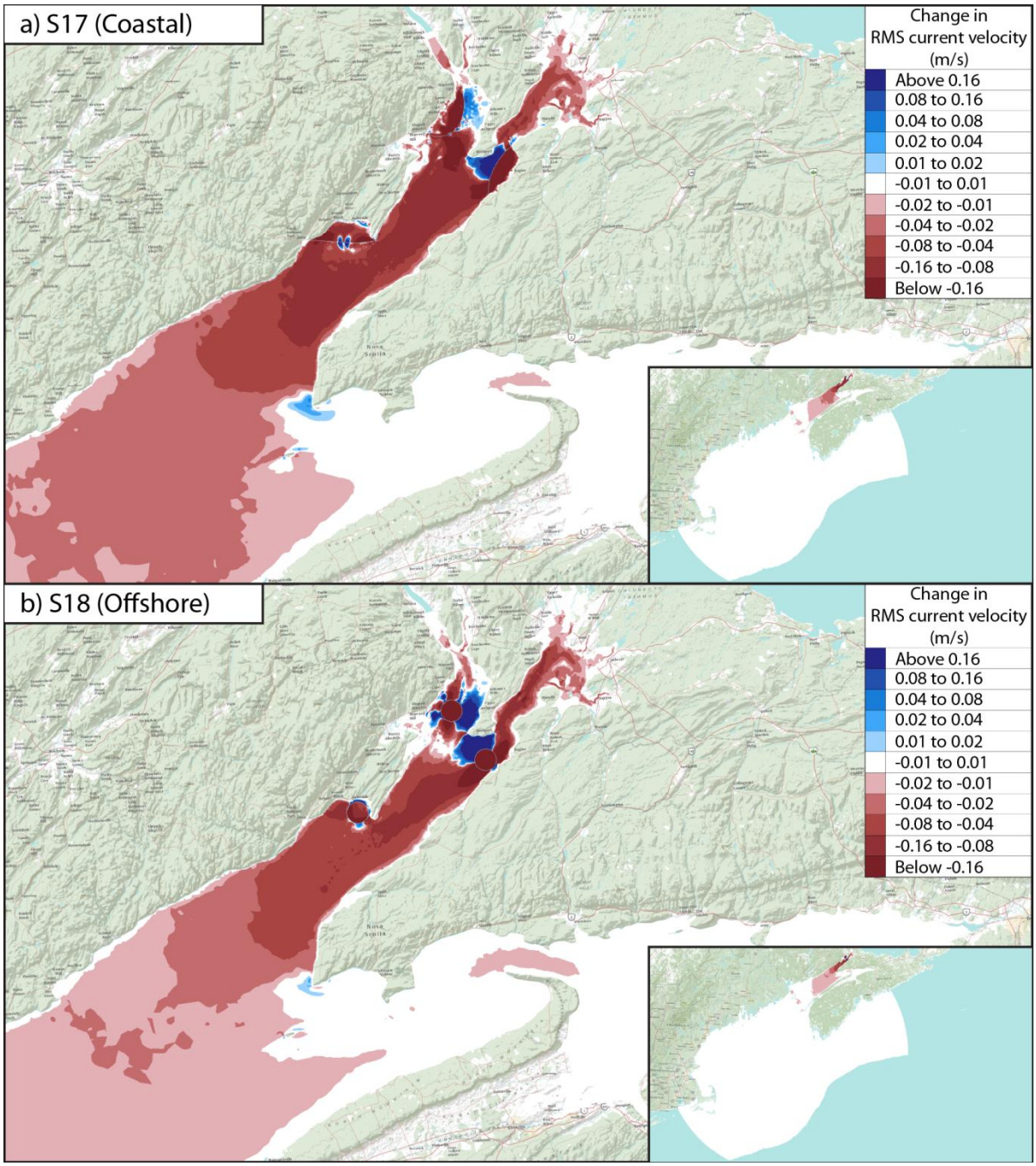

Figure A.30: Changes in RMS current velocity and residual current circulation for S17 and S18.

E.6 Chinecto Bay and Minas Basin (S19)

A - Water levels: Maximum tidal range

This scenario has six offshore tidal lagoons in the Bay of Fundy. More details on the hypothetical scenarios are explained in Section 4.3.2.3. Figure A.31 shows the change in maximum tidal range due offshore tidal lagoons in Minas Basin and Chignecto Bay. As illustrated, the patterns

in tidal range change are a mixture between S16 and S18. The maximum tidal range will decrease 8 to 16+ cm in the Upper Bay of Fundy and increase 4 to 8 cm in the Gulf of Maine.

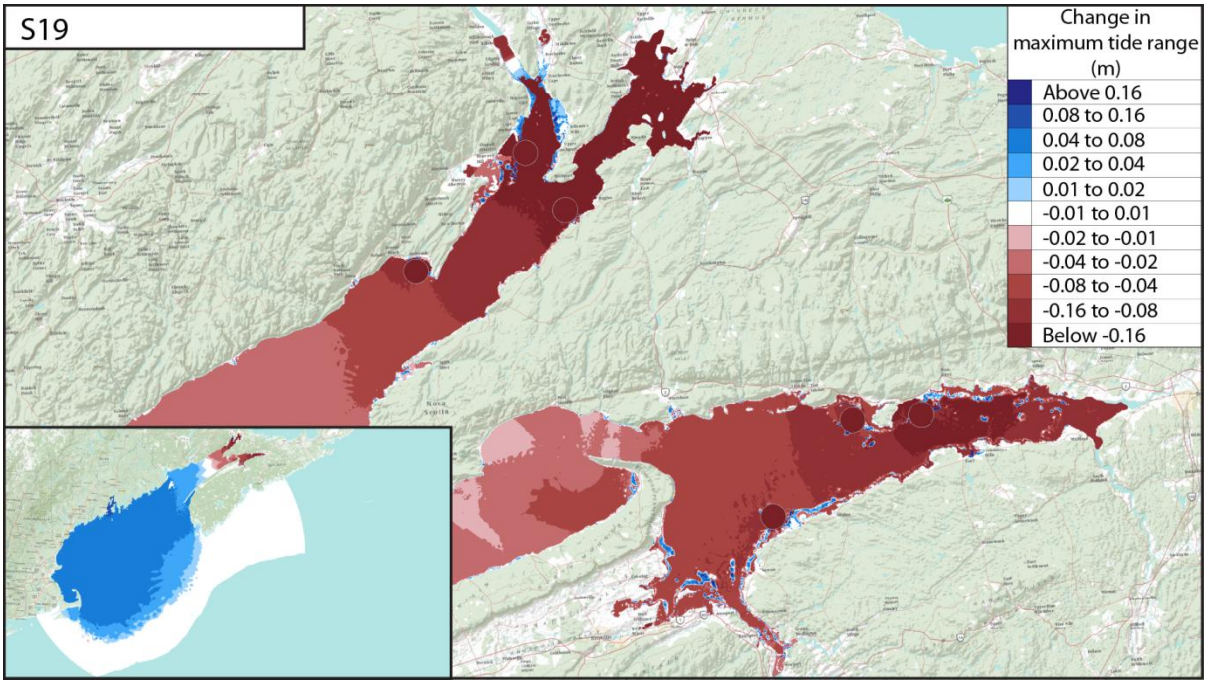

Figure A.31: Changes in maximum tidal range for S19.

B - Current velocity: RMS velocity and residual current

Figure A.32 shows the change in RMS current velocity. As illustrated, the patterns in velocity changes are a mixture between S16 and S18. Minas Passage will be approximately 8 to 16 cm/s slower with the six offshore lagoons. The overall Upper Bay of Fundy will decrease RMS velocity by 4 to 8 cm/s. The most significant velocity increases are shown to occur near the powerhouse and along the impoundment depending on the tidal lagoon layout and powerhouse configuration.

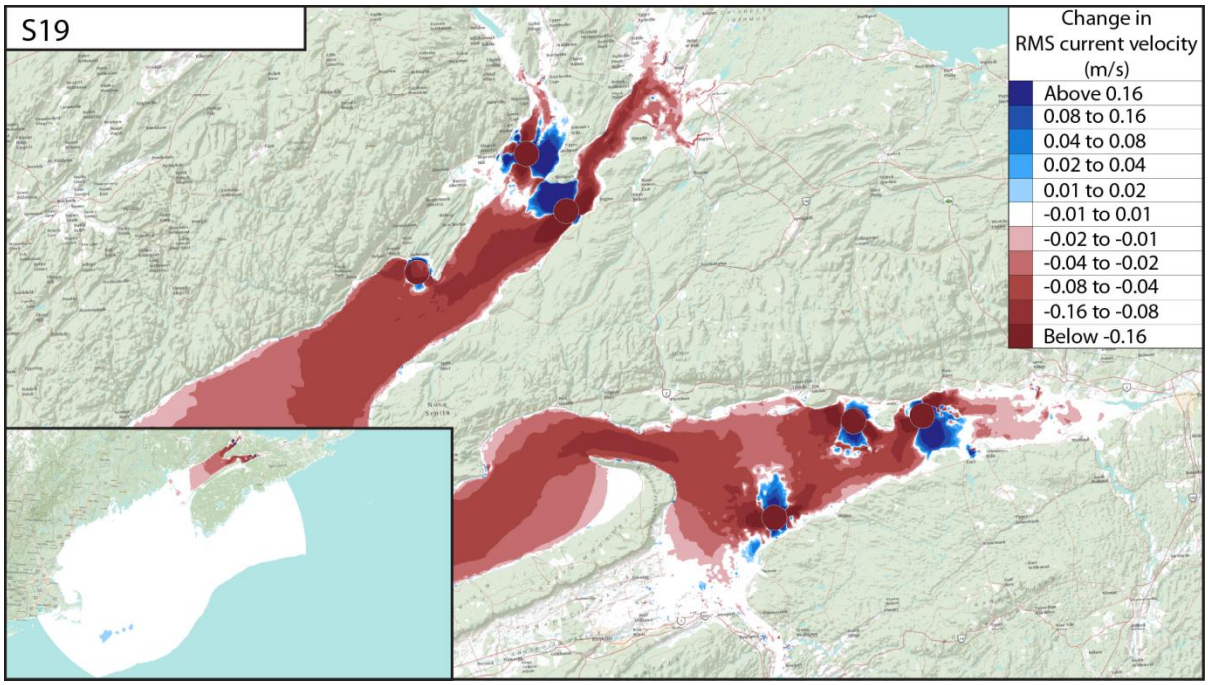

Figure A.32: Changes in RMS current velocity for S19.